RESIDUAL STRESS MODELING IN MACHINING PROCESSES

A Dissertation
Presented to
The Academic Faculty

by

Jiann-Cherng Su

In Partial Fulfillment
of the Requirements for the Degree
of Doctor of Philosophy in the
George W. Woodruff School of Mechanical Engineering

Georgia Institute of Technology
December 2006

RESIDUAL STRESS MODELING IN MACHINING PROCESSES

Approved by:

Dr. Steven Y. Liang, Advisor
George W. Woodruff School of Mechanical Engineering
Georgia Institute of Technology

Dr. Hamid Garmestani
School of Materials Science & Engineering
Georgia Institute of Technology

Dr. Shreyes N. Melkote
George W. Woodruff School of Mechanical Engineering
Georgia Institute of Technology

Dr. Yong Huang
School of Mechanical Engineering
Clemson University

Dr. Richard W. Neu
George W. Woodruff School of Mechanical Engineering
Georgia Institute of Technology

Date Approved: September 29, 2006

ACKNOWLEDGEMENTS

I would like to thank the people and sponsors who made this research possible. First, I would like to thank my advisor Professor Steven Liang for his support and guidance throughout my time at Georgia Tech. I would also like to thank members of my committee, Professors Shreyes Melkote, Richard Neu, Hamid Garmestani, and Yong Huang. Additionally, thanks to Kong Ma at Rolls-Royce and Keith Young at Boeing for providing guidelines and experimental data for the research. I would also like to thank Shesh Srivatsa at GE for his help in the sensitivity analysis and feedback for the research. I would also like to thank the other Metals Affordability Initiative (MAI) team members including Jeff Simmons at the US Air Force for comments and feedback provided throughout the project.

I am also grateful for the financial support provided by the NIST Advanced Technologies Project (ATP) grant "Enabling Technologies for Lean Manufacturing of Hardened Steel Applications" with Chuck Bartholomew as the project monitor that covered the scientific fundamentals of thermal, mechanical, and residual stresses modeling. Financial support provided by the Air Force MAI program, with Jeff Simmons as the project monitor, which covered the model applications to broaching and milling processes, is also greatly valued. Without their funding, completion of this project would not have been possible.

I also want to thank the Precision Machining Research Consortium (PMRC) support staff who have been nothing but helpful during my time at Georgia Tech. I want to thank both past and present officemates for their friendships. I want to thank Meghan Shilling for her support and help in proofreading the dissertation.

Last but not least, I want thank my mom, dad, and brother for their continuous support and encouragement throughout my research. I am truly grateful for all that they have done.

TABLE OF CONTENTS

LIST OF TABLES

Page

LIST OF FIGURES

Page

LIST OF SYMBOLS

t	Uncut chip thickness or depth of cut
t_c	Chip thickness
w	Width of cut
F_C, F_T	Chip formation force in cut direction and thrust direction
F_R	Cutting force due to oblique angle
k_{AB}	Flow stress of material in shear zone
f	Shear angle
a	Tool rake angle
l	Friction angle in chip formation model
A, B, C, m, n	Johnson-Cook flow stress parameters
e_{AB}, $\dot{e}_{AB}$	Strain and strain rate in the shear zone
e_{int}, $\dot{e}_{int}$	Strain and strain rate between tool and chip
C_{Oxley}	Constant in Oxley's cutting force model
P_{cut}, P_{thrust}	Plowing force in cut direction and thrust direction
q_{shear}, $q_{rubbing}$	Heat intensities from shear zone and rubbing
q_{cool}	Heat loss intensity due to coolant
k_t, r_t, C_t	Thermal conductivity, density, and specific heat
V_{cut}	Cutting speed
$\bar{h}$	Overall heat transfer coefficient
S_{ij}	Deviatoric stresses
a_{ij}	Back stresses
R	Uniaxial yield stress of material
$\dot{e}_{ij}^{p}$	Plastic strain rate
n_{ij}	Direction of plastic strain rate
Y	Blending function used in rolling contact algorithm
k	Rolling contact algorithm constant
G	Elastic shear modulus

P_1, P_2, P_3	Cutting forces in tangential, axial, and radial directions
f_{entry}, f_{exit}	Entry and exit immersion angles for milling
F_X, F_Y, F_Z	Forces in feed, normal to feed, and axial directions in milling
D_{cutter}	Milling cutter diameter
r	Corner radius or nose radius
r_e	Edge hone radius
f	Feed rate in turning
d	Depth of cut in turning
$f_{j,k}$	Immersion angle of milling cutter
d_r	Radial depth of cut in milling
d_a	Axial depth of cut in milling
h_{chip}	Chip load in milling

SUMMARY

Residual stresses play an important role in the performance of machined components. Component characteristics that are influenced by residual stress include fatigue life, corrosion resistance, and part distortion. The functional behavior of machined components can be enhanced or impaired by residual stresses. Because of this, understanding the residual stress imparted by machining is an important aspect of understanding machining and overall part quality.

Machining-induced residual stress prediction has been a topic of research since the 1950's. Research efforts have been composed of experimental findings, analytical modeling, finite element modeling, and various combinations of those efforts. Although there has been significant research in the area, there are still opportunities for advancing predictive residual stress methods. The objectives of the current research are as follows: (1) develop a method of predicting residual stress based on an analytical description of the machining process and (2) validate the model with experimental data.

This research looks to fill gaps in current residual stress modeling techniques. In particular, the research will focus on predicting residual stresses in machining based on first principles. Machining process output parameters such as cutting forces and cutting temperatures will be predicted as part of the overall modeling effort. These output parameters will serve as the basis for determining the loads which generate residual stresses due to machining. The modeling techniques will be applied to a range of machining operations including orthogonal cutting, broaching, milling, and turning.

CHAPTER 1

INTRODUCTION

1.1 Overview and Motivation

Residual stresses play an important role in the performance of machined components. Component characteristics that are influenced by residual stress include fatigue life, corrosion resistance, and part distortion. The functional behavior of machined components can be enhanced or impaired by residual stresses. Because of this, understanding the residual stress imparted by machining is an important aspect of understanding machining and overall part quality.

The sources of residual stress are widely varied and include plastic deformation of a material or volume changes of a material due to thermal gradients. In the case of plastic deformation, the residual stress is due to the permanent displacement the crystal structure [1]. The residual stresses caused by thermal gradients are typically a result of a change in volume of the material.

In machining, all of the previously described sources of residual stress are present. Plastic deformation occurs during chip formation and contact between the tool and the machined part. Thermal gradients are produced by plastic deformation as well as frictional heating. If temperature and pressure are high enough, phase transformations on the newly generated surface may occur. Additionally, the effect of stress and temperature on the material behavior during loading may influence residual stresses. As a result, modeling the residual stress formation on a machined surface is a challenging task.

1.2 Research Goals and Objectives

Residual stress prediction is as important as ever. Although there has been significant research in the area, there are still opportunities for advancing predictive residual stress methods. The objectives of the current research are as follows: (1) develop a method of predicting residual stress based on an analytical description of the machining process and (2) validate the methodology with experimental data.

1.3 Research Plan

The research aims to achieve the objectives offered previously through analytical modeling of the cutting process. To that aim, the process will be characterized from a physics based approach with a focus on cutting force, workpiece temperature, and contact stress modeling. A flowchart of the methodology is shown in Figure 1.1.

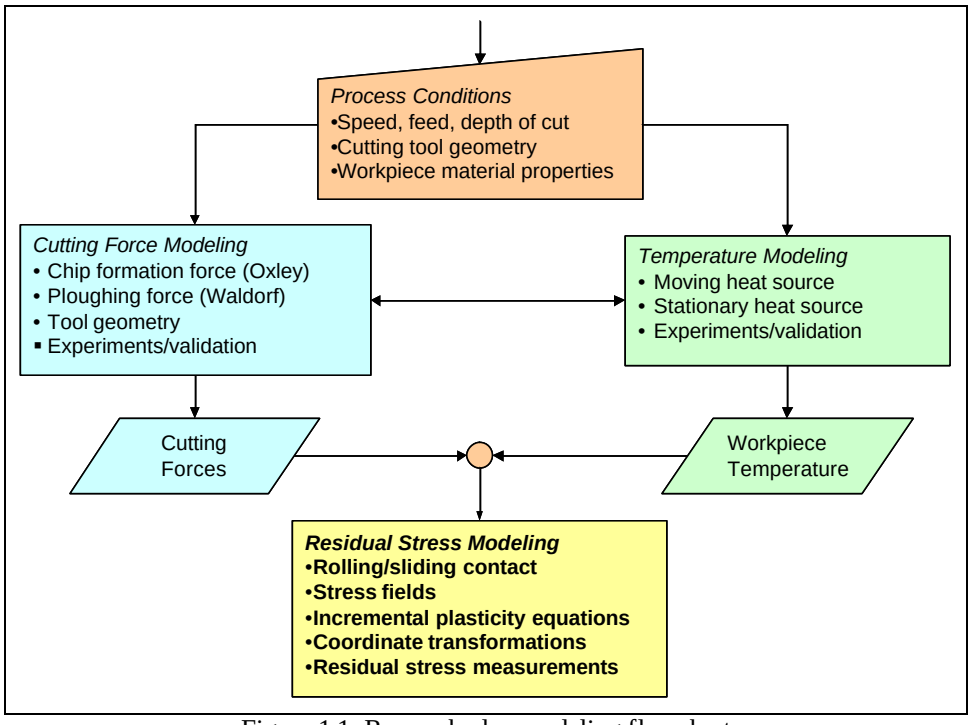

Figure 1.1 Research plan modeling flowchart

As the figure shows, the model takes cutting process conditions such as speed, feed, and depth of cut along with tool geometry and material properties and inputs them into models for predicting cutting forces and cutting temperatures. The cutting forces are predicted from the process parameters. The results are fed into the thermal models to predict the temperature rise in the workpiece due to machining. The outputs from these modeling areas are then used to predict the thermo-mechanical loading experienced by the workpiece and subsequently, the residual stress produced from machining.

The cutting force model will be validated for various cutting conditions including orthogonal cutting, milling, and turning. In predicting cutting forces, tool geometry, cutting parameters, and workpiece material behavior will be considered. The cutting forces are treated as a combination of chip formation and plowing forces. These forces contribute to the mechanical stress experienced by the newly formed machined surface.

In addition to forces, workpiece temperatures will also be explored. The temperature rise in the workpiece due to cutting has a direct impact on the residual stress generation. Thermal expansion due to heating can produce thermal stresses in the machined surface. Additionally, the material behavior, particularly yield stress, is also affected by temperature. Another consideration for thermal effects is the potential for phase change due to the high temperatures and pressures in the vicinity of the tool-workpiece contact zone.

These aspects of the cutting process are used as inputs into a thermo-elastic-plastic model to predict residual stresses from machining. The model predictions will then be validated with experimental data do determine the effectiveness of the modeling technique.

The goal of this work is to establish a predictive model for machining induced residual stress. The model presents advantages over previous efforts in that it aims to be predictive based on kinematics of the process and material properties. Because an extensive calibration of parameters will be unnecessary, the research will enable prediction of machining induced residual stress with much less experimental work.

1.4 Overview of Thesis

The thesis is arranged by the type of machining process that is analyzed. In the following chapter, a review of the present and past literature on machining induced residual stress will be provided. The literature review will provide insight into the research questions that this dissertation seeks to answer.

The following chapters will address the specific modeling techniques for orthogonal cutting, milling, and turning. Each chapter will cover the modeling predictions and experimental validation as well as opportunities for improvement in each area. Force modeling, temperature modeling, and residual stress modeling will be discussed. Conclusions and recommendations will follow and finalize the thesis.

CHAPTER 2

LITERATURE REVIEW

Residual stress prediction has been a topic of research since the 1950's. Research efforts have been composed of experimental findings, analytical modeling, finite element modeling, and various combinations of those efforts. This chapter will focus on previous research in modeling residual stresses produced by machining and lead up to the current state of the field. The chapter is divided into three main categories of residual stress research. Section 2.1.1 describes the experimental research efforts in machining induced-residual stress. Section 2.1.2 covers the analytical modeling efforts for residual stress. Section 2.1.3 assesses the modeling efforts in finite element modeling (FEM). After the review, a summary of potential avenues for residual stress research is presented.

2.1 Literature Review on Machining Induced Residual Stress

2.1.1 Experimental Efforts in Residual Stress

Most of the early efforts at determining the effect of machining on residual stress were experimental in nature. One of the pioneering efforts at assessing the residual stress due to machining was undertaken by Henriksen [2]. The publication presented fundamental experimentation and analysis that is still widely referenced today. Henriksen experimented on low-carbon steel orthogonally machined. The work

concluded that mechanical and thermal effects played a role in the residual stress development, but mechanical influence dominated.

Liu and Barash tried to determine the effect of machining parameters on the residual stress in a machined surface [3]. They found that for orthogonal cutting, four variables uniquely determined the pattern of residual stress on a machined surface. The variables included the length of the shear plane, tool flank wear, shape of the cutting edge, and the depth of cut. The shape of the cutting edge determined the residual stress pattern near the machined surface. Additionally, the research found that tool flank wear increased cutting temperature. They also found that smaller depths of cut did not necessarily produce low subsurface stresses. They concluded that a lower degree of constraint in the deformation process produces a lower level of residual stress. Xie and Bayoumi [4] also investigated the effect of tool wear on residual stress in machining. They found similar results and concluded that tool wear impacted residual stress.

Sadat and Bailey [5] performed orthogonal cutting experiments on AISI 4340 to determine the effects of cutting speed, feed rate, and depth of cut on residual stress profiles. They used a deflection etching technique to measure the residual stresses. They found that the absolute value of the residual stresses increased with an increase in depth beneath the machined surface. Additionally, peak residual stresses at low speeds were tensile but became increasingly compressive at high feed rates.

Sadat [6] also experimented with machining on Inconel-718. That research was an effort to determine the effect of cutting speed and tool-chip contact length on the surface integrity produced by machining. They concluded that both thermal and mechanical effects produced the residual stress distribution and the plastically deformed

layer. They showed that the depth to which residual stresses extend beneath the machined surface increases with a decrease in cutting speed. This was due to lower temperatures for lower cutting speeds. Additional residual stress experimental work has been conducted by Schlauer [7]. The work showed that tensile surface residual stresses were due to nano-sized grains while shear bands in the subsurface corresponded to compressive stresses.

More recently, Jang used turning experiments on AISI 304 stainless steel to determine the effect of machining parameters [8]. Residual stresses were measured using X-ray diffraction. The work showed that the tool sharpness has a strong influence on the surface residual stress. Additionally, they showed that the principal stresses at the surface were close to the hoop and axial directions of the workpiece.

The advent of hard turning has also produced significant findings in terms of machining and residual stress. Matsumoto [9] performed experiments on residual stress generated in hard turning. Fatigue life tests were conducted which showed that the hard turned components were comparable to fatigue life of ground components due to the high levels of compressive subsurface residual stress. It was also determined from experimental data that depth of cut and feed rate did not significantly affect the residual stresses in the subsurface of the material. However, the tool edge geometry played a dominant role in the subsurface residual stress profile, which is consistent with previous work. Mamalis [10] performed similar experiments in hard turning.

Jacobson conducted hard turning experiments on hardened M50 steel HRc 61 [11]. Tests were conducted using different tools while also varying the depth of cut during turning. They found that M50 consistently showed compressive residual stress at

the surface. The amount of residual stress varied from -600 to -1300 MPa. The effective rake angle and nose radius of the tool affect the amount of residual stress generated. Higher negative rake angle and smaller nose radius create a more compressive residual stress profile. The experimental data showed that depth of cut does not affect the amount of residual stress generated in hard turning. An interesting result is that they found that depth of cut does not affect the amount of residual stress. The research also showed that the effective rake angle and tool nose radius both affected the residual stresses.

Liu [12] studied the effects of tool nose radius and tool wear on the residual stress produced in hard turning bearing steel. His results showed that increasing flank wear contributed significantly to the residual stress profile. However, the conclusions were derived primarily from experimental results.

Earlier work showed that the tool edge geometry influences the residual stress generated from machining. Thiele and Melkote performed hard turning experiments on AISI 52100 in order to determine the effect of hardness and tool edge geometry on the residual stresses produced from hard turning [13-15]. The material ranged in hardness from 41 HRC to 57 HRC and the tool hones ranged from 22.9 μm to 121.9 μm. The results showed that large edge hone tools produce measurable sub-surface plastic flow. The workpiece sub-surface flow is associated with deep, compressive through-thickness residual stress.

The experimental research has provided a qualitative understanding of the effects of cutting parameters on machining-induced residual stress. The general findings have indicated that in the absence of chemical changes, the residual stress profile is dependent on a combination of loadings. For cases where mechanical loads dominate, compressive

residual stress profiles are more likely. Where thermal loads dominate, the residual stress profiles show a more tensile character.

2.1.2 Analytical and Statistical Modeling of Residual Stress

The literature reviewed in the previous section focused on experimental efforts in determining machining induced residual stress. This section covers research that has aimed to quantify and explain the mechanisms that produce residual stress from machining. The models range from traversing loads to polynomial curve fitting. Each aims to correlate the effect of machining parameters to residual stress.

Tsuchida et al [16] experimented on the effect of cutting conditions on the residual stress distribution. They performed tests in which speeds, feeds, and depths of cut were varied. They concluded that a decrease in the cutting speed decreases the tensile residual stress near the surface, and increases the depth of the residually stressed layer. Also, an increase of feed shifted the surface residual stress towards tension while increasing the residually stressed layer. They also found that an increase in the depth of cut did not affect the residual stress distributions. Most significantly, they discovered that the peak residual stresses can exist beneath the surface of machined components. An empirical formula for the surface residual stress was produced from their experiments.

In other work, Liu and Barash [17] aimed to characterize the state of the bulk of the material due to the chip removal process. Three quantities were established as relevant to quantifying the mechanical state of the workpiece. They included apparent strain energy density, strain hardening index, and residual stress distribution. The research showed that the length of the shear plane uniquely determined the plastic deformation of the subsurface layer for a given depth of cut. The three parameters

mentioned previously all increased with the length of the shear plane. They also found that a size effect influenced the state of the machined sub-layer. These findings were significant in that they established an overall material state rather than just residual stress. In a subsequent paper [18], they added flank wear to the list of input parameters. They found that the flank wear length altered the residual stress pattern by reducing the shear plane length. They concluded that the origins of residual stress are predominantly mechanical although thermal influence is apparent.

Matsumoto, Barash, and Liu [19] studied the effect of hardness on surface integrity of AISI 4340 steel. They analyzed the effects based on the type of chip formation. Machined components with hardness below HRC 49 produced continuous chips. Increasing hardness led to segmented chip formation. They utilized the concept of rolling contact loading to explain the cyclic loading experienced by the workpiece during machining. This effort was significant in that it was an early application of theory in an attempt to explain machining-induced residual stresses. They deduced that the change in the residual stress pattern corresponding to a change in material hardness was analogous to the change in residual stresses for change in reduction ratio in drawing. For low reduction ratio drawing, plastic deformation is confined near the surface, and a compressive residual stress is produced. However, for high reduction ratio drawing, the plastic deformation reaches deeper into the material producing tensile residual stresses. For hardened steel, the surface layer affected by the deformation is shallow, and burnishing is the dominant stress generating mechanism resulting in compressive residual stress. When soft steel is cut, the deformation reaches a deeper layer and the surface layer is compressed resulting in tensile residual stress.

In an effort to model the residual stress formation due to machining, Wu and Matsumoto [20] employed the idea of a passing load over a point in the workpiece. The rationale is that all points in the workpiece experience the same stress history. This stress history subsequently influences the residual stress. For loading conditions that are predominantly compressive, the resulting residual stress will be tensile when strains are returned to zero. For loads that are primarily tensile, the resulting residual stress is compressive when strains return to zero. They used an integration of the Boussinesq equation to predict the stresses experienced in the subsurface due to the passing load.

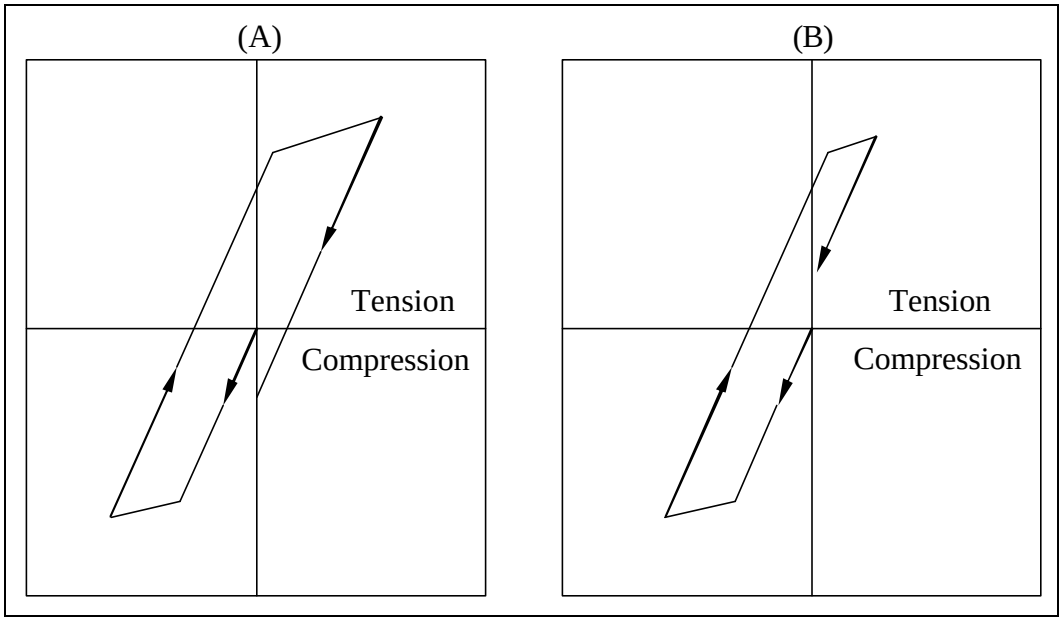

Figure 2.1 Residual stress formation for (A) predominantly tensile loading and (B) predominantly compressive loading. [20]

In other machining processes, Fuh [21] developed an empirical model to predict the residual stresses produced by milling of 2014-T6 aluminum. The mathematical model incorporated cutting conditions such as cutting speed, feed, and cutting depth as well as tool geometry characteristics such as nose radius and flank wear. The research utilized a response surface methodology (RSM) coupled with a Takushi method to limit the number of required experiments. The postulated mathematical model implemented

second-order polynomial to produce a relationship between the residual stress and cutting parameters. The curve fitting technique provided little insight into the physical relationship between the cutting parameters and the residual stress.

One of the more recent analytical models was presented by Jacobus [22]. The research utilized an incremental plasticity model, similar to that used by Merwin and Johnson [23]. Rather than assume a stress field in the workpiece, the model assumed a form for the deformation of the material beneath the tool. Residual stress was modeled in a coordinate frame with respect to the tool. The deformation parameters were treated as a function of the edge radius and the depth of cut. The parameters were calibrated from experimental tests and an optimization procedure. The work also provided a rationale for the effect of thermal loads and mechanical loads on the residual stress generated in machining. The dependence of tool orientation with respect to the principal axes of residual stress was also documented. Although the research provided a sound fundamental basis for residual stress modeling, it was still largely dependent on curve fitting techniques.

Mittal and Liu continued efforts in modeling residual stress in hard turning [24]. The model assumed that the residual stress profiles fit a polynomial profile that was a function of depth into the workpiece. The coefficients of the polynomial were individual functions of the machining parameters. This model required calibration of a large number of coefficients. Additionally, it did not provide any insight into the residual stress formation. El-Axir [25] modeled residual stress in a similar fashion as did Sridhar [26].

2.1.3 Residual Stress Modeling with FEM

In contrast to the previous sections, the following reviews will highlight residual stress modeling based on FEM. Use of FEM and commercial packages is becoming more common in residual stress research due in part to the improvements in computing power and modeling capabilities.

One of the earliest efforts at modeling residual stress using FEM was undertaken by Okushima and Kakino [27]. They were one of the first to apply significant analysis to residual stress prediction from the machining process. The plowing effect of the tool edge and the thermal effect of temperature distribution produced in metal cutting were modeled. The modeling results were compared with experimental data measured by X-ray diffraction. Residual stresses were measured in the cutting direction and across the cutting direction. They concluded that mild cutting conditions were necessary to minimize tensile residual stresses.

Mishra [28] developed an analytical model based on FEM to determine residual stresses due to a moving heat source. The model predicted the residual stresses of thermal and mechanical origin in a grinding process. The author discussed the effect of the magnitude of mechanical force, the rate of heat input, and the speed of movement of the workpiece on the residual stresses.

Lin [29] used a finite element method to determine the strain field in the workpiece. Using the strain field, the concept of particle flow was employed to determine the stress history of the strain history of the material. The modeling procedure introduced by Merwin and Johnson [23] was used to predict the residual stresses produced by machining. Lin incorporated both thermal and mechanical loads in the

model. Trends from the model were compared with experimental data. Model boundary conditions such as shear angle were assumed to be known a priori. Another work by Lin and Lee [30] used the same modeling methodology but included the effect of flank wear.

In similar research aimed at determining the interaction between thermal and mechanical loading, Wiesner [31] used a finite element method to determine the residual stresses from orthogonal machining of AISI 304. The stationary workpiece temperatures were calculated using a finite difference method. The results from the model showed that the thermal and mechanical impact of the orthogonal cutting process caused tensile residual stresses. The model was validated by X-ray diffraction measurements of machined samples. Low shear angles and working angles were found to be factors that increased tensile residual stress.

Shih [32] developed a plane-strain finite element simulation of orthogonal metal cutting. The research incorporated detailed material modeling including effects of elasticity, viscoplasticity, temperature, large strain, and high strain-rate. The model was validated and compared with experimental results. Although the model and the experimental results were comparable, the model, like others did not clarify the mechanisms that cause the residual stress.

Hua [33, 34] used a commercial FEA package DEFORM 2D, which is a Lagrangian implicit code designed for metal forming processes to simulate orthogonal cutting of AISI 52100. The work focused on analyzing the effect of feed rate, workpiece hardness, and cutting edge on the subsurface residual stress formation in hard turning. The results were compared with experimental data and showed reasonable agreement between model predictions and experimental data.

Other FEM models of interest include the work of Liu and Guo [35, 36]. They used the commercial FEM code Abaqus/Explicit to investigate the effect of sequential cuts and tool-chip friction on residual stresses in a machined layer of AISI 304 stainless steel. The affected layer from the first cut was found to change the residual stress distribution produced by the second cut. Additionally, residual stress is sensitive to the friction condition at the tool-chip interface.

FEM methods have been able to produce sufficiently informative results in predicting residual stress due to cutting. However, the FEM models have made little effort to clarify the mechanisms which give rise to the machining induced residual stresses. Additionally, FEM still requires significant computational power, and can be time prohibitive. Changes in the cutting conditions require re-computing the model. Because of this, use of FEM as a means of for production guidance has been restricted.

The current state of analytical modeling of the tool condition on the residual stress falls short in terms of application to industrial environments. Models like that developed by Jacobus [22] require extensive model calibration based on cutting tests. Other models that have been used to predict residual stress have also required a great deal of experimental data [21, 24-26] which was used to fit the residual stress data in a curve-fitting model. FEM does an adequate job in predicting the residual stresses, but they are not easily adaptable for varying process parameters because they are typically time consuming. The analytical models cover various aspects of sources of residual stress and mechanisms that affect the profiles. However, a thorough model for predicting residual stress with consideration of tool edge condition is currently unavailable.

2.2 Future Efforts in Residual Stress Modeling

Residual stress modeling in machining has been the subject of research since the 1950's. A majority of the work the work has focused on orthogonal machining processes. The modeling efforts have included experiments, semi-analytical modeling, statistical modeling, and finite element methods. Throughout the previous research, several parameters have been identified as being significant in contributing to residual stress formation. Among the parameters that have been shown to have the most influence are tool geometry (cutting edge radius, nose radius, rake angle, flank wear), cutting conditions (cutting speed, feed, depth of cut), and material behavior (hardness, flow stress).

Most of the previous research has provided generalizations about the impact of mechanical or thermal loads in the generated residual stress profile. Some analytical efforts have been made to clarify the interaction between thermal and mechanical loads [22, 29, 37]. A majority of the recent work has been focused on finite element methods [32-34, 38, 39]. Even though these methods are being used more often, they still require great computational expense which can be a limiting factor in their use.

Based on the review of literature relating to machining-induced residual stress, opportunities for augmenting the knowledge base in the research area still exist. The following research directions can help to enhance the understanding and modeling of machining induced residual stress.

Analytical modeling of the effects of process parameters is needed. It has been shown in previous research that the effects of tool edge geometry and cutting parameters impact machining-induced residual stress. To date, the available research has yet to

produce an analytical model capable of capturing the effects of process parameters on residual stresses produced by machining. The importance of residual stress in machining drives the need for such capabilities.

A first-principles based approach to machining must be coupled with residual stress prediction. Many of the previous efforts in modeling residual stresses from machining have focused on a blend of empirical and analytical modeling, with more emphasis on the empirical aspect. With more emphasis on the physics-based modeling, deeper understanding of the process is possible.

Improving the flexibility of residual stress modeling for a variety of machining operations is also an important aspect of the research. Many of the models are based on an orthogonal approach and limited to orthogonal conditions. Extending the modeling capabilities to more complex operations such as milling and turning will enhance the value of analytical residual stress modeling.

Another aspect of machining-induced residual stress that has rarely been considered in prior research has been the effect of cutting fluid. Although usually ignored, cutting fluid is a necessity for certain machining operations. As a result, the impact of cutting fluid needs to be examined or considered in modeling applications.

Efforts should also be made into the use of alternative techniques for measuring residual stresses. Common methods of measuring residual stress include hole-drilling, sectioning, and x-ray diffraction. All of these methods are inherently destructive and laborious for sub-surface residual stress measurements. Consequently they have proven to be unsuitable for use in production environments. An alternative such as ultrasonic

measurement may enable the measurement of residual stress in a real-time manner suitable for use in inspection processes.

This research looks to fill gaps in current residual stress modeling techniques. In particular, the research will focus on predicting residual stresses in machining based on first principles. Machining process output parameters such as cutting forces and cutting temperatures will be predicted as part of the overall modeling effort. These output parameters will serve as the basis for determining the loads which generate residual stresses due to machining. The modeling techniques will be applied to a range of machining operations including orthogonal cutting, broaching, milling, and turning. The techniques used will differ from previous efforts like that used by Jacobus [22] in that extensive parameter calibration will be unnecessary because the loading inputs are determined from process output parameters such as cutting forces.

This thesis will be divided based on the type machining operation being discussed. Specifically, the subsequent chapters will discuss the following:

- Overall residual stress modeling technique
  - Cutting force modeling
  - Thermal modeling
  - Residual stress modeling
- Application of modeling to orthogonal cutting operation
- Application of modeling to milling operations
  - Special considerations for milling
- Application of modeling to turning operations
  - Special considerations for turning

- Discussion of process parameters and their impact on machining-induced residual stress

CHAPTER 3

MODELING RESIDUAL STRESS IN ORTHOGONAL CUTTING

This chapter describes in detail the residual stress model for orthogonal cutting. First, the cutting force models for orthogonal cutting are discussed. Next, modeling of cutting temperatures is presented. Then the coupling of the force and thermal modeling is illustrated to complete the predictive residual stress model.

3.1 Force Modeling in Orthogonal Cutting

Force modeling in orthogonal cutting has been the subject of research for many years. One of the earliest analyses of cutting forces by M.E. Merchant was based on the assumption that the shear angle adjusts itself to minimize cutting force [40]. Other models have incorporated slip-line field theory to predict cutting forces in orthogonal cutting [41-43]. The residual stress modeling effort in this research seeks to incorporate the previously developed models for predicting cutting forces. The goal of the current research is not to develop a perfectly accurate cutting force model but rather to utilize well established predictive cutting force models as a means of estimating boundary contact stresses.

The cutting forces in the present model are assumed to consist of chip formation and plowing forces. These two force components contribute to the overall cutting forces. The cutting force models are derived for orthogonal or oblique cutting conditions.

Application of the models to turning operations requires geometric transformations for oblique conditions. Each aspect of the cutting force model is described in the following.

3.1.1 Sharp Tool Cutting Forces

The sharp tool cutting force model chosen for this work is based on Oxley's predictive machining theory [41]. It is a slip-line cutting force model derived from experimental observations in metal cutting. Plane strain, steady-state conditions are assumed. Additionally, the tool is assumed to be perfectly sharp. A brief overview of the model is provided below.

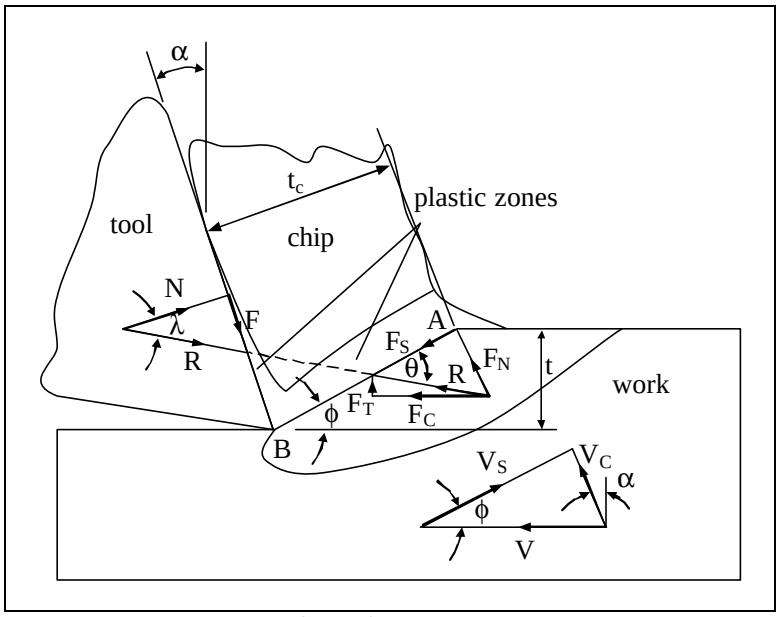

Figure 3.1 Model of chip formation used in analysis [41]

This theory analyzes the stress distributions along *AB* and the tool-chip interface shown in Figure 3.1. f is selected so that the resultant forces transmitted by *AB* and the tool-chip interface are in equilibrium. After f is defined, the chip thickness t_c and other force components can be determined from the following equations.

$$
\begin{aligned}
t_C &= t\cos(f-a)/\sin f \\
F_C &= R\cos(l-a) \\
F_T &= R\sin(l-a) \\
F &= R\sin l \\
N &= R\cos l \\
R &= \frac{F_S}{\cos q} = \frac{k_{AB} tw}{\sin f \cos q}
\end{aligned}
\tag{3.1}
$$

Due to the nature of the cutting process, high strains, strain rates, and temperatures are generated in the cutting zone. A constitutive model that captures these effects is required. In this effort, the Johnson-Cook flow stress model is used to model the material flow stress as a function of strain, strain rate, and temperature [44]. The general form of the equation is shown in Equation (3.2). s is the effective stress, e_p is the effective plastic strain, $\dot{e}_p$ is the effective plastic strain rate, T is the temperature of the material, T_m is the melting point of the material, and T_0 is a reference temperature. The terms A, B, C, m, n, and $\dot{e}_0$ are material constants.

$$
s = \left(A + Be_p^n\right)\left(1 + C\ln\frac{\dot{e}_p}{\dot{e}_0}\right)\left(1 - \left(\frac{T - T_0}{T_m - T_0}\right)^m\right) \tag{3.2}
$$

Determining the value of the shear angle f is an iterative procedure. First, the temperature rise in region AB is computed in order to predict the flow stress k_{AB} in AB. The strain along AB is given by

$$
e_{AB} = \frac{1}{2\sqrt{3}}\frac{\cos a}{\sin f \cos(f-a)} \tag{3.3}
$$

and the strain rate along AB is given by

$$
\dot{e}_{AB} = \frac{C_{Oxley}}{\sqrt{3}}\frac{V_S}{l}. \tag{3.4}
$$

The flow stress along AB is then given by

$$k_{AB} = \frac{1}{\sqrt{3}}\left(A + B\varepsilon_{AB}^{\ n}\right)\left(1 + C\ln\frac{\dot{\varepsilon}_{AB}}{\dot{\varepsilon}_0}\right)\left(1 - \left(\frac{T_{AB} - T_0}{T_m - T_0}\right)^m\right). \tag{3.5}$$

After the flow stress is determined, the cutting forces are computed by Equation (3.1). The friction angle λ is given by

$$l = q + a - f\ , \tag{3.6}$$

where the inclination angle q of the resultant force is given by

$$\tan q = 1 + 2\left(\frac{p}{4} - f\right) - Cn\ . \tag{3.7}$$

In the above equation, the term Cn used in the present application differs from the original definition in Oxley's model. The modified version allows the Johnson-Cook flow stress model to be incorporated into the cutting force model. The modified Cn term used is based on modifications to the original Oxley model presented by Wang [45]. It is defined by

$$Cn = C_{Oxley} n \frac{B\varepsilon_{AB}^{\ n}}{A + B\varepsilon_{AB}^{\ n}}, \tag{3.8}$$

where A, B, and n are constants defined in the Johnson-Cook flow stress equation.

After the angles are determined, the tool-chip contact length is computed by

$$h = \frac{t_1 \sin q}{\cos l \sin f}\left\{1 + \frac{Cn}{3\tan q}\right\}. \tag{3.9}$$

Assuming the stress distribution along the tool chip contact length is constant, the shear stress along the tool chip interface is given by

$$t_{int} = \frac{F}{hw}\ . \tag{3.10}$$

The temperature rise in the chip is then computed based on the method described by Oxley [41]. The resulting expression for the average flow stress in the chip is given by Equation (3.11).

$$k_{chip} = \frac{1}{\sqrt{3}}\left(A + B\varepsilon_{int}^{n}\right)\left(1 + C\ln\frac{\dot{\varepsilon}_{int}}{\dot{\varepsilon}_0}\right)\left(1 - \left(\frac{T_{int} - T_0}{T_m - T_0}\right)^m\right) \tag{3.11}$$

In Equation (3.11) the average value of strain in the chip is approximated by [46] as

$$\varepsilon_{int} = 2\varepsilon_{AB} + \frac{1}{\sqrt{3}}\frac{h}{d t_2} \tag{3.12}$$

and the strain rate in the chip by

$$\dot{\varepsilon}_{int} = \frac{1}{\sqrt{3}}\frac{V_C}{d t_2}. \tag{3.13}$$

For each shear angle f increment, all of the computations are made to determine t_{int} and k_{chip}. The highest value of f at which $t_{int} = k_{chip}$ is chosen as the shear angle for the process. A simplified flowchart of the modeling procedure is shown in Figure 3.2.

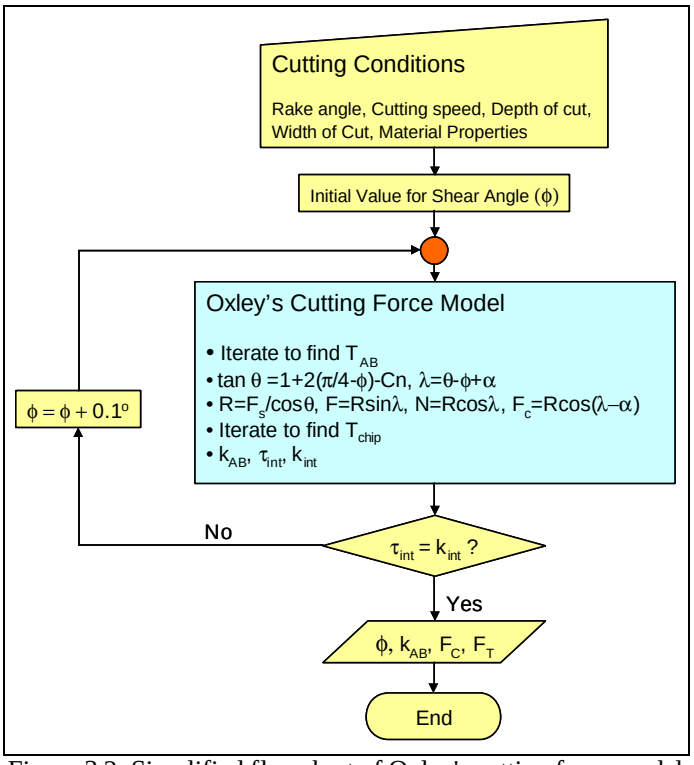

Figure 3.2 Simplified flowchart of Oxley's cutting force model

The outputs of the model include the shear angle f, flow stress k_{AB}, cutting force F_C, and thrust force F_T. The predictive model described above is for dry conditions. The friction angle l is computed based on force balance and material behavior. However, for lubricated conditions where the friction coefficient m of the lubricant is known, the friction angle is computed based on the coefficient of friction by

$$m = \tan l \ . \tag{3.14}$$

This method of incorporating the effect of friction in predicting cutting forces has been utilized by Li [47] for modeling cutting forces in near dry machining.

3.1.2 Force Modeling Considering Tool Edge Radius

In the previous discussion, the cutting tool is assumed to be perfectly sharp. However, tools are never perfectly sharp. In order instill strength and toughness in the

cutting edge, a hone or chamfer is typically part of the tool geometry. The force contribution due to the roundness of the cutting edge was termed plowing force by Albrecht [48]. Since that work, a great deal of research into the force contribution due to the roundness of a cutting edge has been performed [49-54].

The model developed by Waldorf [43, 54] is used in the present study to predict the plowing forces due to tool edge roundness. Waldorf used a slip-line model developed for predicting plowing forces in orthogonal cutting. The model incorporated a small, stable built-up edge of material adhered to the cutting tool. A brief description of the model is provided below.

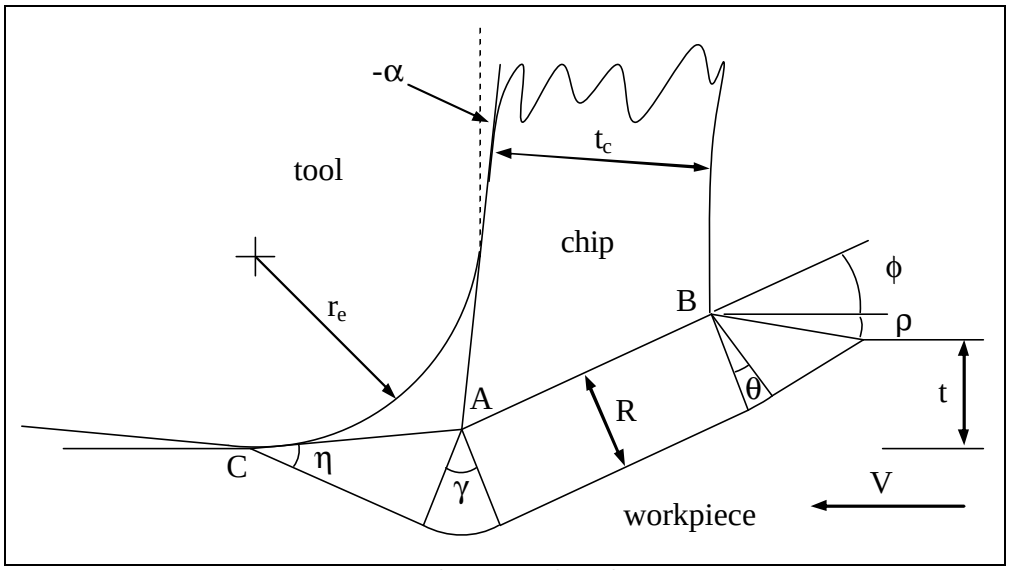

Figure 3.3 Waldorf's slipline field for plowing [54]

In Figure 3.3 r_e is the edge radius, a is the rake angle, f is the shear angle, and t is the uncut chip thickness. The fan field angles q, g, and h are found from geometric and friction relationships. Details for computing the values are available in [43]. R is the radius of the circular fan field centered at A. If the flow stress k of the material is known along with the shear angle f, the plowing forces can determined from Equation (3.15).

P_{cut} is the plowing force in the cutting direction, P_{thrust} is the plowing force normal to the newly generated surface, and w is the width of cut.

$$\begin{aligned} P_{cut} &= k \cdot w \begin{bmatrix} \cos(2h)\cos(f-g+h)+ \\ (1+2q+2g+\sin(2h))\sin(f-g+h) \end{bmatrix} \cdot CA \\ P_{thrust} &= k \cdot w \begin{bmatrix} (1+2q+2g+\sin(2h))\cos(f-g+h)- \\ \cos(2h)\sin(f-g+h) \end{bmatrix} \cdot CA \end{aligned}, \tag{3.15}$$

where

$$CA = \frac{R}{\sin h}. \tag{3.16}$$

In the Waldorf model, the prow angle r was found to be dependent on cutting edge radius. For large hone radii, a prow angle of 0° was found to generate force predictions that closely approximate measurements. For smaller hone radii, a larger prow angle performed better at predicting the plowing forces. In the present application, a prow angle of 10°, which is within the range of prow angles considered in [43], is used.

3.1.3 Average Rake Angle Model

In Section 3.1.1, one of the governing assumptions in the chip formation force model is that the cutting tool is sharp. However, since the force prediction used in the present application considers the edge roundness, the assumption of a perfectly sharp tool needs to be revised. Due to the roundness of the tool, the effective rake angle will vary depending on the depth of cut as well as the size of the cutting edge. For a shallow depth of cut relative to the radius of the cutting edge, the effective rake angle will become more negative. An average rake angle model developed by Manjunathaiah [55] is used to

compute an effective rake angle for force modeling. Significant results from the model are presented below.

In general, the average rake angle will depend on the uncut chip thickness t, edge radius r_e, the separation or stagnation point angle q, and the nominal rake angle of the tool a. The separation angle plays an important role in defining the average rake angle. Material above the separation point (P in Figure 3.4) goes to the chip while material below forms the workpiece. The separation angle has been studied widely by previous researchers [49, 56, 57]. Basuray [49] derived the value for the separation angle by an approximate energy analysis. The value was found to be approximately 37.6°. In the current application, a separation angle of 37.6° is used to compute the average rake angle. Figure 3.4 illustrates the elements primary elements in the average rake angle model.

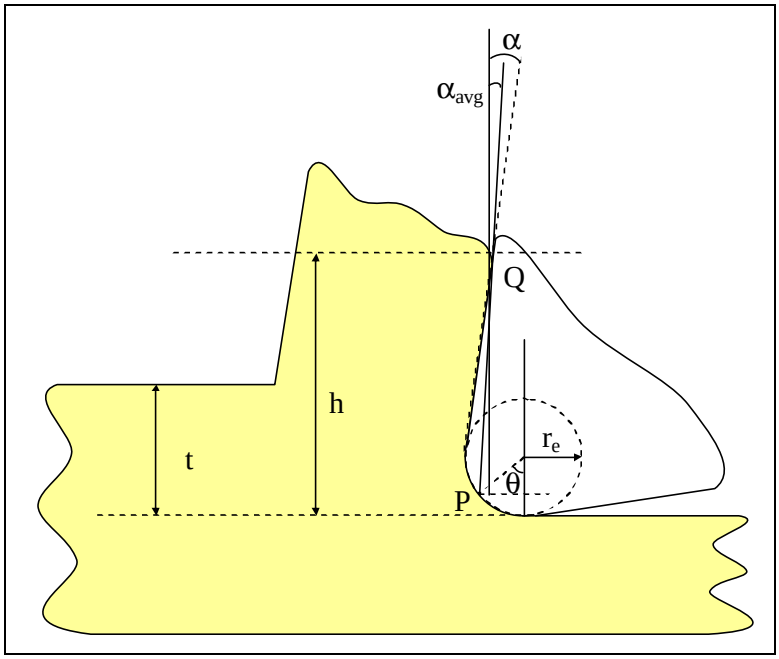

Figure 3.4 Adapted from Manjunathaiah [55]. Schematic for computing the average rake angle

If the tool geometry and cutting conditions are known, then there are two possibilities for the average rake angle. For the case where the uncut chip thickness is less than the radius of the cutting tool, the average rake angle is given by

$$\alpha_{avg} = \begin{cases} \tan^{-1}\left(-\dfrac{\sqrt{\left(2 - h/r\right)h/r} - \sin\eta}{h/r - 1 + \cos\eta} \right) & when \;\; h/r \le 1 + \sin\alpha \\ \tan^{-1}\left(\dfrac{\left(h/r - 1\right)\tan\alpha - \sec\alpha + \sin\eta}{h/r - 1 + \cos\eta} \right) & when \;\; h/r > 1 + \sin\alpha \end{cases} \quad . \quad (3.17)$$

If the uncut chip thickness is greater than the edge radius then the average rake angle is given by

$$\alpha_{avg} = \begin{cases} \tan^{-1}\left(-\dfrac{2\sqrt{\left(1 - h/r\right)h/r} - \sin\eta}{2h/r - 1 + \cos\eta} \right) & when \;\; h/r \le \dfrac{1 + \sin\alpha}{2} \\ \tan^{-1}\left(\dfrac{\left(2h/r - 1\right)\tan\alpha - \sec\alpha + \sin\eta}{2h/r - 1 + \cos\eta} \right) & when \;\; h/r > \dfrac{1 + \sin\alpha}{2} \end{cases} \quad . \quad (3.18)$$

3.1.4 Force Modeling Behavioral Analysis

A breakdown of the cutting forces predicted from the cutting force model is shown in Figure 3.5. The total forces consist of both the chip formation and plowing forces. The forces in the cut direction are typically dominated by the chip formation forces, while forces in the thrust direction are more evenly balanced between chip formation and plowing forces.

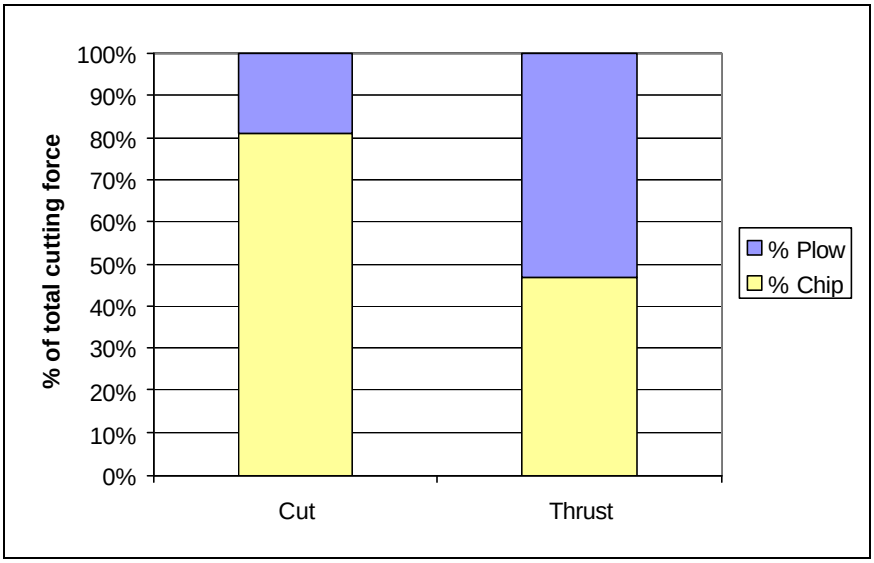

Figure 3.5 Force breakdown for orthogonal cutting conditions

A sensitivity analysis of the process parameters used to compute the cutting forces is also used to evaluate the behavior of the force model. A two-level, four-factor design of experiments is used to determine the effect of varying the input parameters on the predicted cutting force. The variables chosen are user-controlled parameters. The input factors are as follows:

- ER – edge or hone radius
- DOC – depth of cut
- Speed – cutting speed
- Rake – rake angle of the tool.

The responses of the model are listed below.

- Fc – chip formation force in cut direction
- Ft – chip formation force in thrust direction
- Pc – plowing force in cut direction
- Pt – plowing force in thrust direction
- phi – predicted shear angle

The range of input factors is provided in Table 3.1. The force computations are made assuming a 7.0 mm width of cut, AISI 4340 workpiece material, and tungsten carbide cutting tool.

Table 3.1 Cutting force input parameter levels

Variable	Low	High
ER (mm)	0.025	0.75
DOC (mm)	0.100	0.200
Speed (m/s)	1.0	2.0
Rake (deg)	0.0	6.0

The main effects plots for the chip formation forces *Fc* and *Ft* are shown in Figure 3.6 and Figure 3.7, respectively. The results show that the force in the cut direction is strongly influenced by the edge radius *ER* and the depth of cut *DOC* for the range of inputs explored. These two factors affect the shear zone and consequently the force in the cut direction. The cutting speed and the rake angle have less impact on the chip formation force in the cut direction. Increasing cutting speed produces a decrease in the cutting force which is consistent with thermal softening and lower cutting forces.

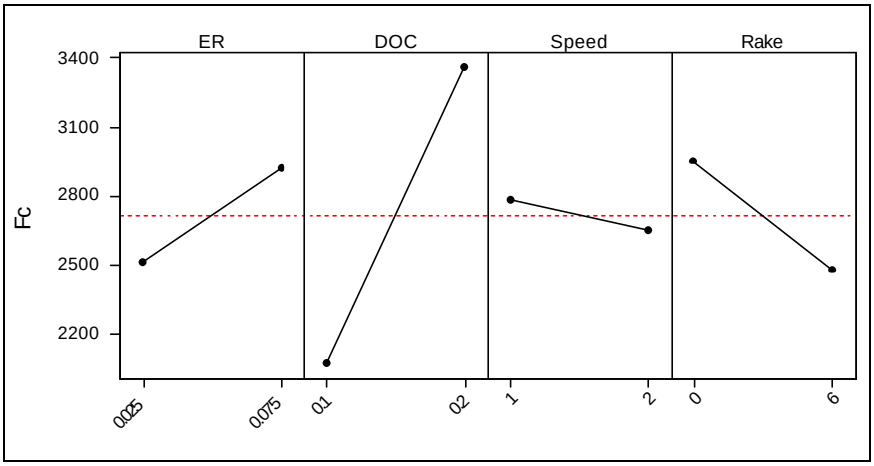

Figure 3.6 Main effects plot for *Fc* in orthogonal cutting

The chip formation thrust force *Ft* is also driven by the size of the edge radius depth of cut, and rake angle. It is more dependent on the cutting speed than the force in the cut direction. The tool has a tendency to pull into the workpiece for larger rake angles resulting in the decreased thrust force. Increasing the depth of cut and edge radius tends to push the tool away from the workpiece resulting in larger forces in the thrust direction. A summary of the main effects for chip formation forces is provided in Table 3.2.

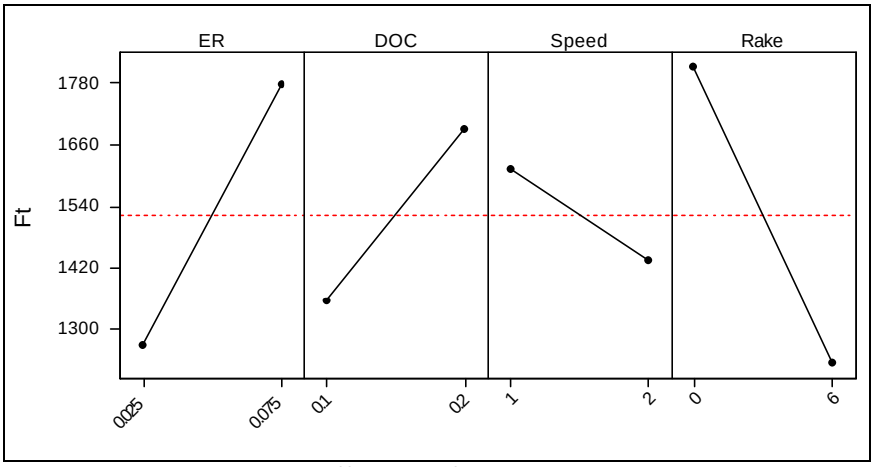

Figure 3.7 Main effects plot for *Ft* in orthogonal cutting

Table 3.2 Summary of effect of increasing input variables on *Fc* and *Ft*

Input Variable	*Fc*	*Ft*
ER	large increase	large increase
DOC	large increase	large increase
Speed	decrease	decrease
Rake	decrease	decrease
Comment	▪ Chip formation forces increase with edge radius due to change in effective rake angle ▪ Larger edge radius results in lower shear angle due to more negative effective rake angle ▪ Higher cutting speeds result in lower cutting forces due to thermal softening ▪ Larger rake angle lowers chip formation forces due to change in shear angle	

The main effects plots for the plowing force in the cut direction *Pc* and the plowing force in the thrust direction *Pt* are shown in Figure 3.8 and Figure 3.9, respectively. The plots show a strong dependence on the edge radius. This impact is expected since the formulation of the plowing force model is based largely on the edge radius. The depth of cut also has some impact on the plowing force, although not nearly as apparent as the edge radius.

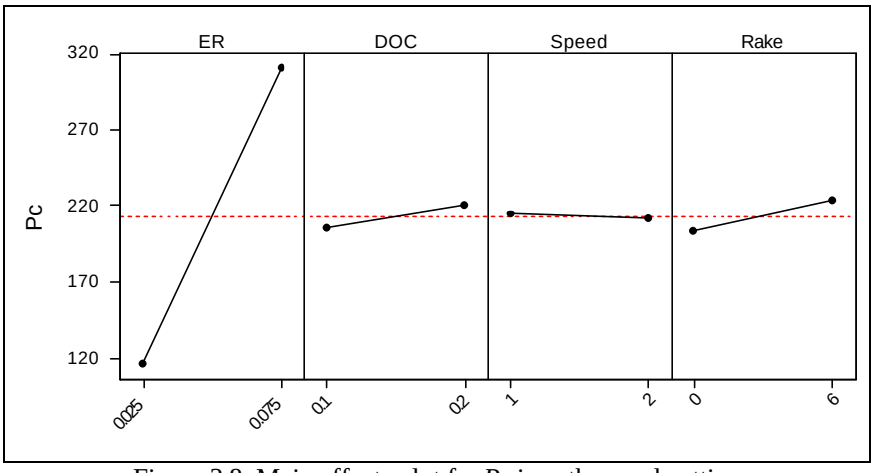

Figure 3.8 Main effects plot for *Pc* in orthogonal cutting

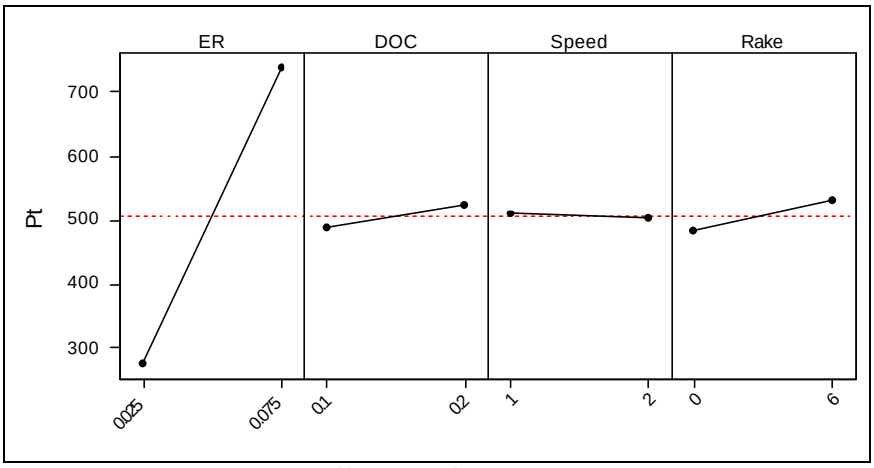

Figure 3.9 Main effects plot for *Pt* in orthogonal cutting

Table 3.3 Summary of effect of increasing input variables on *Pc* and *Pt*

Input Variable	*Pc*	*Pt*
ER	large increase	large increase
DOC	slight increase	slight increase
Speed	n/c	n/c
Rake	slight increase	slight increase
Comment	▪ Plowing forces increase with increasing edge radius. ▪ Other factors have minimal impact due to formulation of plowing force model. Considers primarily cutting edge radius.	

The influence of the predicted shear angle is apparent in the previous cutting force predictions. To illustrate the influence of the cutting parameters on the shear angle and the subsequent impact on cutting forces, a main effects plot of the shear angle predictions is shown in Figure 3.10. Increasing the edge radius produces a less positive rake angle. The same effect is seen when decreasing the depth of cut or decreasing the rake angle. A lower shear angle results in a longer shear zone and consequently higher cutting forces necessary for chip formation.

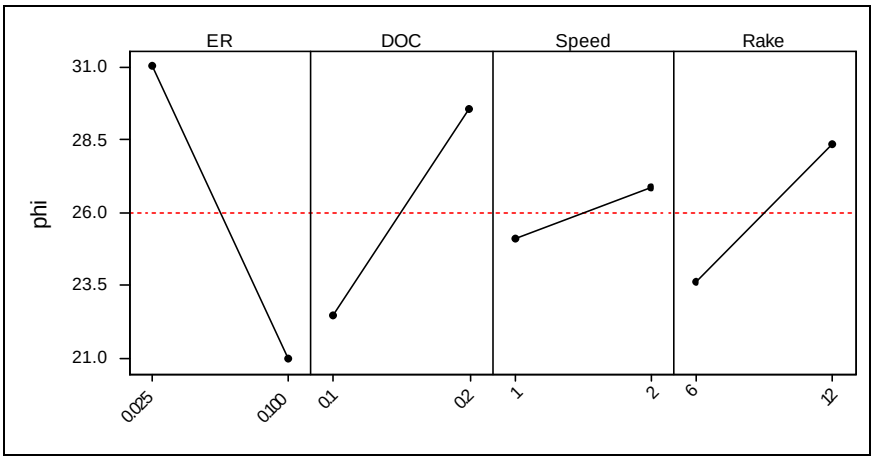

Figure 3.10 Main effects plot for *phi* in orthogonal cutting

Three additional parameters relevant to the force model are also varied to estimate the impact on the cutting force predictions. The Johnson-Cook parameters *C* and *m* and the friction coefficient for lubricated conditions *mu* represent factors which have more variability compared to known values such as depth of cut, speed, and rake angle. The main effects plot for total force in the cut direction *Fx* and the total thrust force *Fy* is shown in Figure 3.11 and Figure 3.12, respectively. For the range of values explored, *mu* has the most influence on the total force predictions. The material parameters *C* and *m* have a slight impact on the cutting forces. These results indicate that variability in the material behavior parameters and lubrication have an effect on the predicted cutting forces.

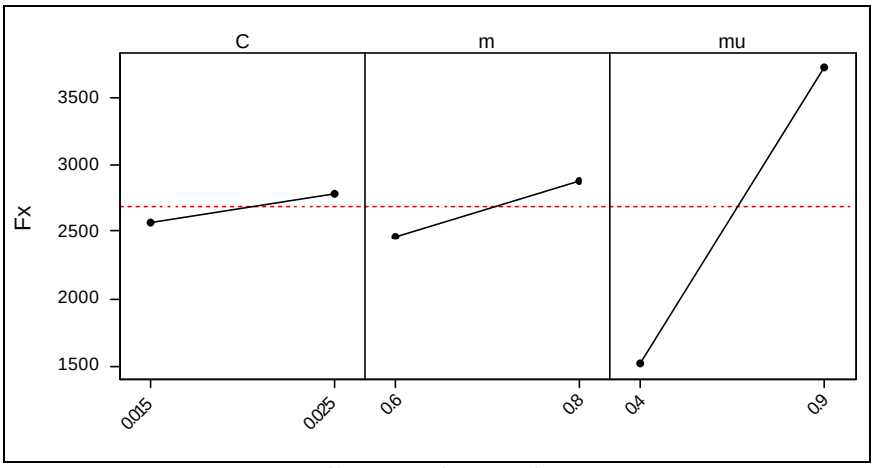

Figure 3.11 Main effects plot for total forces in cut direction

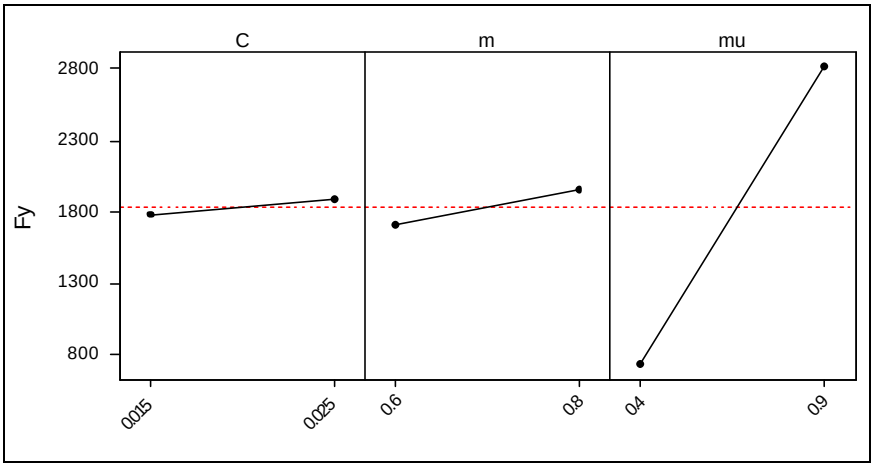

Figure 3.12 Main effects for total forces in thrust direction

The sensitivity analysis of the cutting force model shows that the edge radius is a significant parameter when predicting cutting forces. It has an impact on the effective cutting geometry and consequently, other cutting output parameters. For the range of friction coefficients explored, *mu* is also a significant parameter affecting the total cutting forces.

3.2 Temperature Modeling in Orthogonal Cutting

The thermal effects due to the cutting process can have a significant effect on the residual stresses produced. Researchers have shown that increased cutting temperatures

result in greater tensile residual stress on the surface of a machined component [2, 29]. Jaeger [58] advanced a method of determining the temperature rise due to moving heat sources. Extensions of his method have been used extensively in the literature to determine the temperature rise due to cutting [59-61]. That same approach to modeling the temperature rise due to cutting will be used in this research.

3.2.1 Modeling Workpiece Temperature Rise

In modeling the workpiece temperatures, two heat sources are assumed to exist. The first is the primary heat source generated from the shear zone. The second heat source is a result of rubbing between the tool and the workpiece. The workpiece surface is considered to be insulated in this study as illustrated in Figure 3.13. To satisfy the adiabatic condition at the workpiece boundary, an imaginary heat source is used [59].

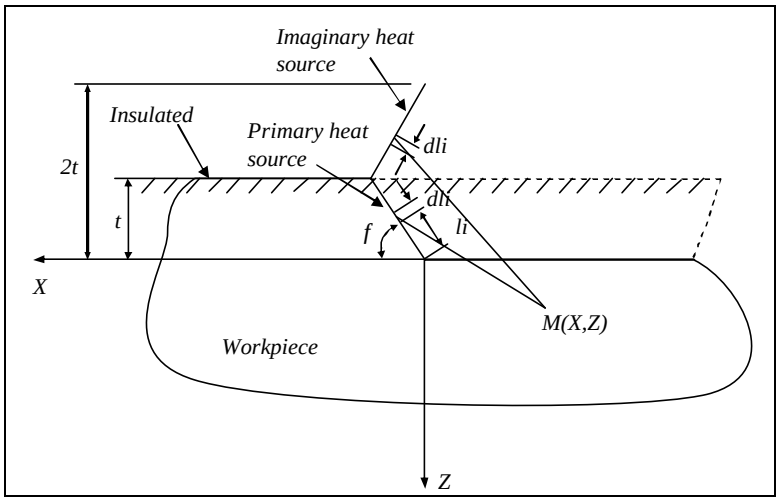

Figure 3.13 Adapted from [62]. Heat transfer model of primary source relative to workpiece

The temperature rise at a point *M(X, Z)* is the combination of the primary and imaginary heat sources. The total temperature rise at any point *M(X, Z)* due to the oblique moving heat source and the imaginary heat source is given by

$$q_{workpiece-shear}(X,Z)=\frac{q_{shear}}{2p\,k_{workpiece}}\int_0^L e^{-\frac{(X-l_i\sin j)V_{cut}}{2a_{workpiece}}}\left\{K_0\left[\frac{V_{cut}}{2a_{workpiece}}\sqrt{(X-l_i\sin j)^2+(Z-l_i\cos j)^2}\right]\right.$$
$$\left.+K_0\left[\frac{V_{cut}}{2a_{workpiece}}\sqrt{(X-l_i\sin j)^2+(Z+l_i\cos j)^2}\right]\right\}dl_i \quad (3.19)$$

where $j=\left(f-\frac{p}{2}\right)$ and $L=\frac{t}{\sin f}$.

A similar application of the moving heat source is used to determine the temperature rise due to rubbing between the cutting edge and the workpiece. The rubbing between the tool edge and the workpiece is treated as a moving band heat source. Since the workpiece surface is considered insulated, an imaginary heat source coincident with the original rubbing heat source is used to model the temperature rise. The moving band heat sources are shown in Figure 3.14. The temperature rise in the workpiece due to rubbing is given by Equation (3.20).

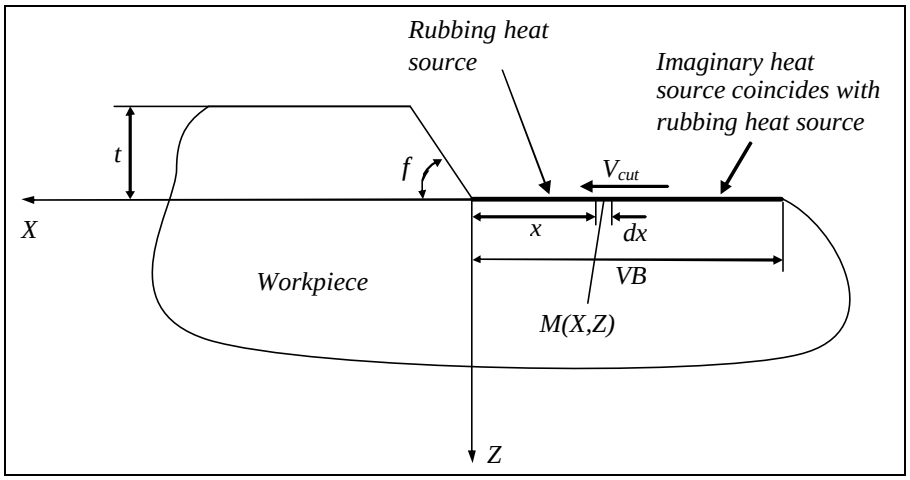

Figure 3.14 Adapted from [62]. Heat transfer model of rubbing heat source relative to workpiece

$$q_{workpiece-rubbing}(X,Z)=\frac{1}{p\,k_{workpiece}}\int_0^{VB} g\cdot q_{rubbing}(x)e^{-\frac{(X-x)V_{cut}}{2a_{workpiece}}}K_0\left[\frac{V_{cut}}{2a_{workpiece}}\sqrt{(X-x)^2+(Z)^2}\right]dx \quad (3.20)$$

g in the equation is a partition of heat transferred into the workpiece during cutting. An approximate value for the partition ratio based on material properties of the

tool and the workpiece is given by Equation (3.21) where k, r, C, k_t, r_t, *and* C_t, are the thermal conductivity, density, and specific heat of the workpiece and tool, respectively [63].

$$g = \frac{\sqrt{krC}}{\sqrt{krC} + \sqrt{k_t r_t C_t}}, \tag{3.21}$$

The heat sources q_{shear} and $q_{rubbing}$ are determined from the cutting parameters and the cutting force models described in the previous section. The resulting expressions for the shear plane heat source and the rubbing heat source are given by Equations (3.22) and (3.23), respectively.

$$q_{shear} = \frac{(F_c \cos f - F_t \sin f)(V_{cut} \cos a / \cos(f - a))}{(t)(w)\csc f} \tag{3.22}$$

$$q_{rubbing} = \frac{P_{cut} V_{cut}}{(w) VB} \tag{3.23}$$

For machining with coolant, the cooling effect is treated as a stationary heat sink. The coolant is assumed to be applied behind the tool as shown in Figure 3.15. By treating the coolant as a stationary heat sink, the analytical model for predicting the temperature rise due to a stationary heat source can be used [64].

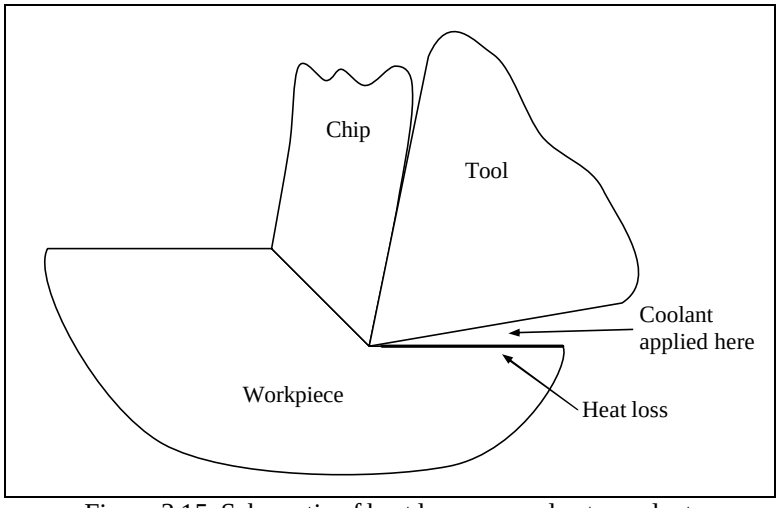

Figure 3.15 Schematic of heat loss source due to coolant

The temperature drop in the workpiece due to the stationary heat source associated with the coolant is given by Equation (3.24).

$$q_{cool}(X,Z) = \frac{q_{cool}}{2p\,k_t}\int_0^{l}\int_{-w/2}^{w/2}\left(\frac{1}{R_i}+\frac{1}{R_i'}\right)dydx \tag{3.24}$$

In Equation (3.24), l is the distance behind the tool tip to which coolant is acting, w is the width of the cut region, $R_i = \sqrt{(X_2 - x_i)^2 + (Y_2 - y_i)^2 + Z_2{}^2}$ and $R_i' = \sqrt{(X_2 - (2L_{VB} - x_i))^2 + (Y_2 - y_i)^2 + Z_2{}^2}$. The heat loss intensity q_{cool} is given by Equation (3.25) where $\bar{h}$ is the overall heat transfer coefficient, T is the temperature rise of the workpiece due to the shear plane and rubbing heat sources, and T_0 is the ambient temperature.

$$q_{cool} = \bar{h}(T - T_0) \tag{3.25}$$

The net change in the temperature of the workpiece due to machining and coolant is the superposition of the two heat sources and one heat sink.

$$q_{total}(X,Z) = q_{shear}(X,Z) + q_{rub}(X,Z) + q_{cool}(X,Z) \tag{3.26}$$

3.2.2 Temperature Modeling Behavioral Analysis

A typical temperature profile below the machined surface is shown in Figure 3.16. The maximum workpiece temperature occurs at the surface near the tool tip. The temperature drops quickly behind the tool tip. The exact temperature profile depends on the cutting parameters and the thermal properties of the workpiece material.

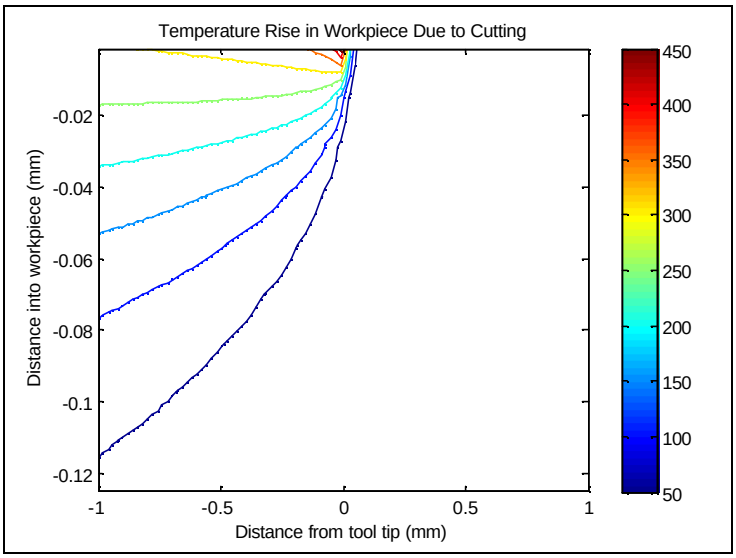

Figure 3.16 Temperature profiles beneath tool due to cutting

A sensitivity analysis similar to that used for the cutting forces is performed for the cutting temperatures in the workpiece. The inputs include the edge radius, depth of cut, cutting speed, and rake angle. The range of factors is identical to those in Table 3.1. The response variable is the average temperature 1.0 mm ahead, 1.0 mm behind the tool tip, and 0.25 mm beneath the surface. The main effects plot for the average temperature is shown in Figure 3.17. As the figure shows, the only input factor that results in a temperature increase when increased is the edge radius. The lower temperature attributed to increasing the depth of cut can be accounted for by referring to Figure 3.10. That figure shows that the shear angle increases with increasing depth of cut. Although the cutting force increases, it increases less than if the shear angle remained constant. As a

result, the heat intensity used to predict the cutting temperatures is actually lower compared to a shallower depth of cut. A similar argument can be made for the effect of the rake angle.

With regards to the cutting speed, an increase in cutting speed results in lower average temperatures in the workpiece. This is due to the nature of the force prediction and its interaction with the thermal model. The temperature prediction in the workpiece is isolated from the temperature prediction in the force model. The thermal softening experienced in the chip due to higher cutting speeds produces lower heat intensity in the shear zone. Additionally, the higher cutting speeds allow less time for the heat to penetrate into the surface which also lowers the average temperature around the tool tip.

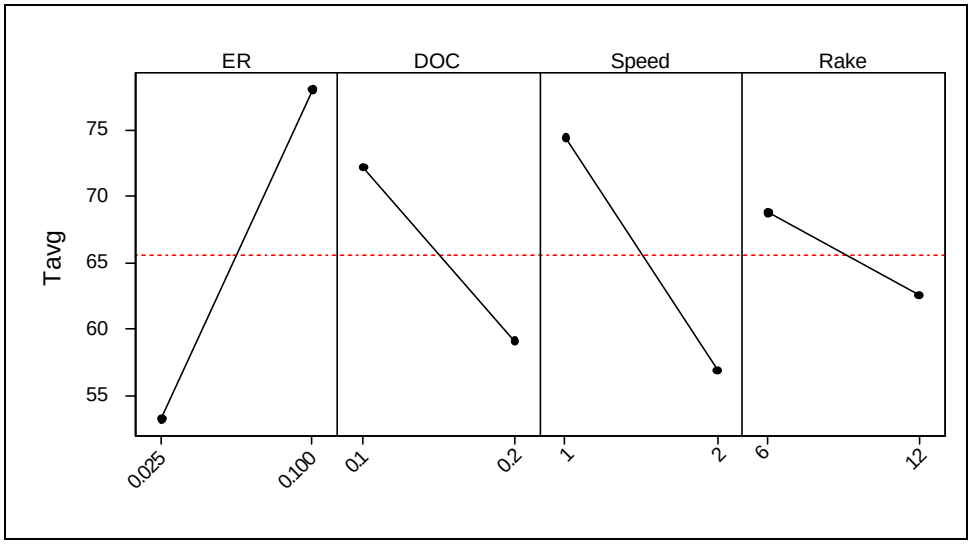

Figure 3.17 Main effects for average temperature near tool tip *Tavg*

3.3 Residual Stress Modeling in Orthogonal Cutting

3.3.1 Residual Stress Modeling

Capturing the stress history experienced by the workpiece during cutting is necessary for predicting the residual stresses. A rolling/sliding contact approach is used

to model the stress history in the workpiece. In Figure 3.18, the round object represents a load and the rectangular area represents the body being loaded. As the load passes over the body, every point at the same depth in the body will experience the same stress. For instance, the stress history experienced by point *A* during the passage of the load will be similar to the right side of Figure 3.18. The specific stress history depends on the boundary stresses between the load and the body.

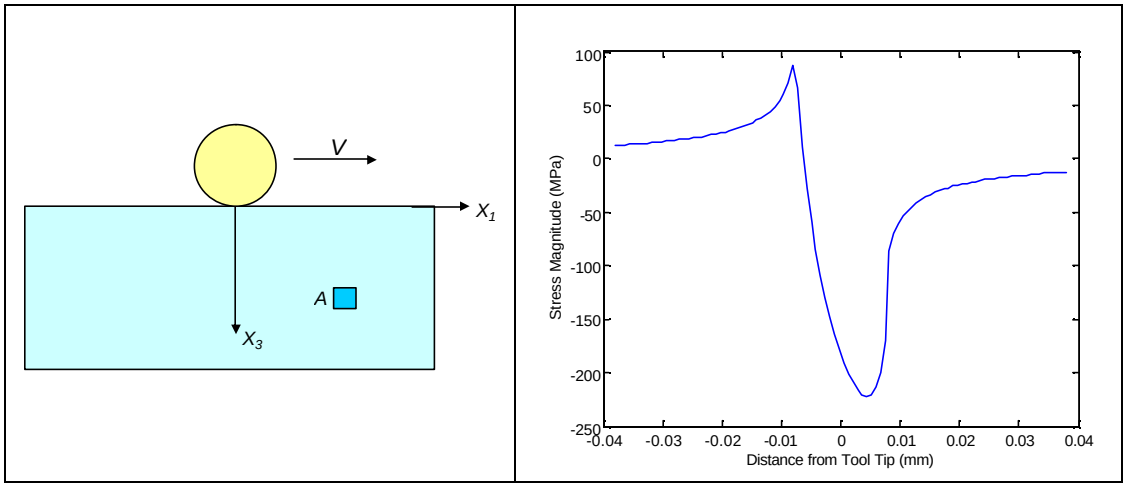

Figure 3.18 Contact stress load history

Two sources of mechanical stress due to cutting are considered. One is due to contact between the tool edge and the workpiece, and the other is from the stresses in the shear zone. The tool edge contributes to a normal load coupled with a tangential load. The shear zone adds an inclined shear stress and normal stress. These two sources comprise the stress history experienced by the workpiece. Both are shown in Figure 3.19.

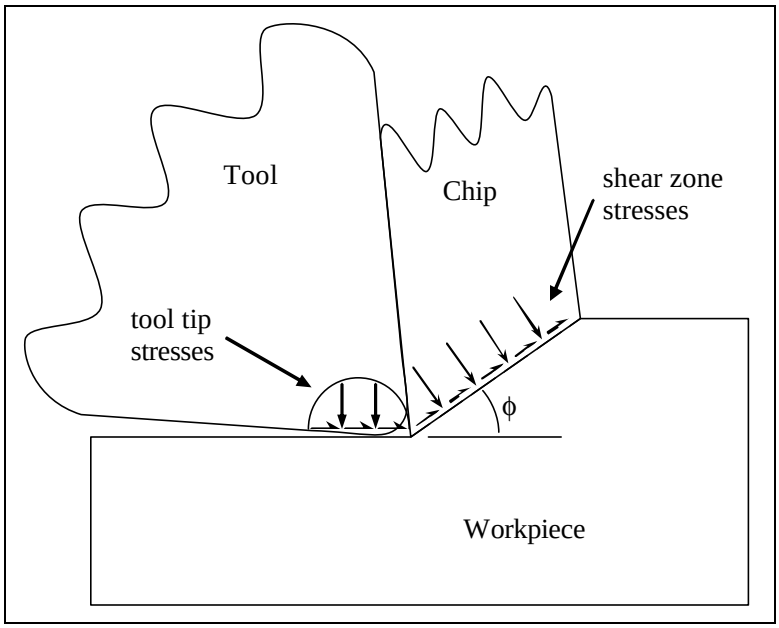

Figure 3.19 Stress sources for residual stress modeling

The stresses in the workpiece are computed by integrating the Boussinesq solution for normal and tangential point loads in semi-infinite bodies over the region of contact. The results of the integration are shown in Equation (3.27) [65].

$$
\begin{aligned}
s_x &= -\frac{2z}{p}\int_{-b}^{a}\frac{p(s)(x-s)^2}{\left[(x-s)^2+z^2\right]^2}ds - \frac{2}{p}\int_{-b}^{a}\frac{q(s)(x-s)^3}{\left[(x-s)^2+z^2\right]^2}ds \\
s_z &= -\frac{2z^3}{p}\int_{-b}^{a}\frac{p(s)}{\left[(x-s)^2+z^2\right]^2}ds - \frac{2z^2}{p}\int_{-b}^{a}\frac{q(s)(x-s)}{\left[(x-s)^2+z^2\right]^2}ds \\
t_{xz} &= -\frac{2z^2}{p}\int_{-b}^{a}\frac{p(s)(x-s)}{\left[(x-s)^2+z^2\right]^2}ds - \frac{2z}{p}\int_{-b}^{a}\frac{q(s)(x-s)^2}{\left[(x-s)^2+z^2\right]^2}ds
\end{aligned}
\tag{3.27}
$$

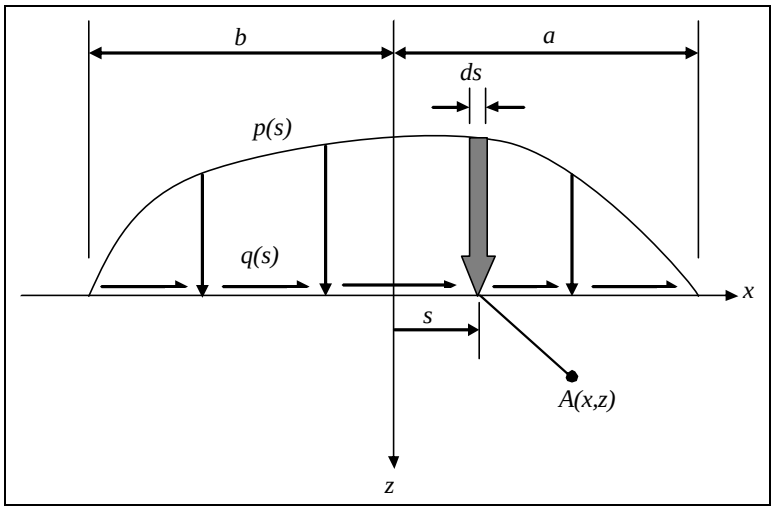

Figure 3.20 Adapted from Johnson [65]. Schematic of boundary stresses

In order to utilize Equation (3.27), the stress distributions *p(s)* and *q(s)* shown in Figure 3.20 are needed. The magnitude of the normal stress is determined from the geometry of the contact region and the plowing thrust force P_{thrust}. The normal pressure in the contact region due to the tool tip is assumed to be two-dimensional Hertzian. An analytical solution to Equation (3.27) exists for Hertzian contact [66]. The analytical solution requires the maximum pressure p_0 due to the normal load which is determined from Equation (3.28) where a is approximated as one-half CA from Equation (3.16). A uniform stress distribution has also been tested with similar results.

$$p_0 = \frac{2P_{thrust}}{p\,(wa)}. \tag{3.28}$$

The shear stress at the surface is assumed to be uniformly distributed and proportional to the stress induced by the plowing cutting force P_{cut} and the coefficient of friction m as shown in Equation (3.30).

$$t = m\left(\frac{P_{cut}}{w \cdot CA}\right) \tag{3.30}$$

In addition to the stresses induced by the edge hone, the shear stress produced by the shear plane is treated as a constant value equal to the flow stress of the material in that region. The inclined normal load is determined from the predicted cutting forces and the geometry of the shear plane. This type of approach has been used in previous research to estimate stresses in the workpiece due to the shear plane [20, 29].

The total mechanical stress in the workpiece is the sum of the stresses due to tool tip and the stresses due to the shear plane. In order to combine the stresses, the stresses predicted for the shear zone must be transformed from the shear zone coordinates *X'-Z'* to the workpiece coordinates *X-Z*. The respective coordinates are shown in Figure 3.21.

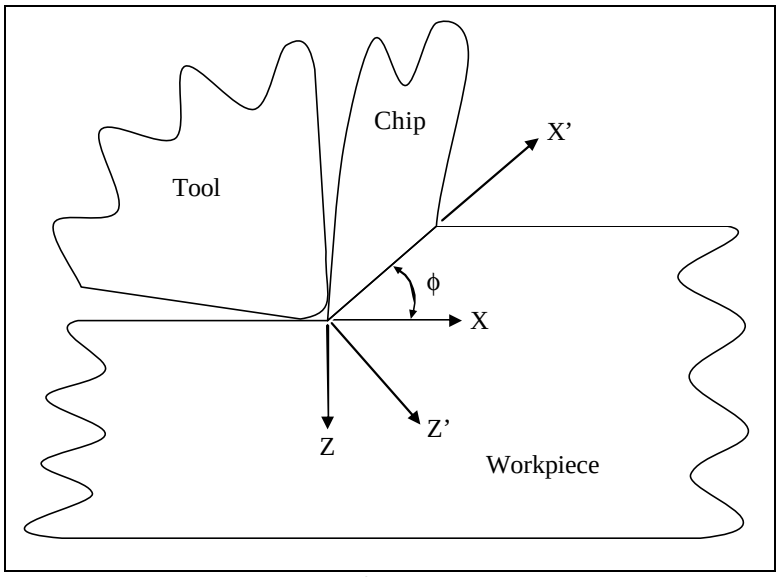

Figure 3.21 Coordinate system of shear plane with respect to workpiece

The stresses with respect to the *X'-Z'* coordinate system are computed from Equation (3.27). A rotation matrix (Equation (3.31)) is then used to transform the stresses in the *X'-Z'* coordinate system to the *X-Z* coordinate system. The stresses from the shear zone expressed in the workpiece coordinates are given by Equation (3.32). A typical combined stress field is shown in Figure 3.22.

$$[Q] = \begin{bmatrix} \cos f & \sin f \\ -\sin f & \cos f \end{bmatrix} \tag{3.31}$$

$$\left[s_{shear\_X-Z} \right] = [Q] \begin{bmatrix} s_{X'} & t_{X'Z'} \\ t_{X'Z'} & s_{Z'} \end{bmatrix} \left[Q^T \right] \tag{3.32}$$

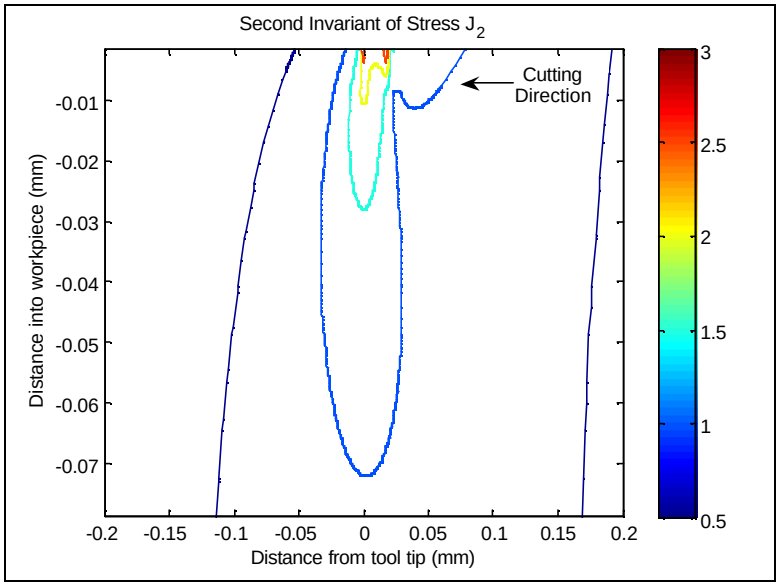

Figure 3.22 Stressfield contours in workpiece

Using the stress fields captured from the forces, contact zones, and thermal predictions, the residual stresses are computed from a rolling/sliding contact algorithm developed by McDowell [67]. The hybrid algorithm devised by McDowell captures desirable aspects of previous rolling/sliding contact models [68, 69]. The model provides a robust, stable prediction of subsurface plasticity and residual stresses over a wide range of loading conditions. Because of this, it is well suited for the type of contact experienced by the workpiece during the cutting process. The algorithm also admits arbitrary forms of kinematic hardening for non-proportional cyclic plasticity. The loading determines the subsurface residual stress and the size of the subsurface plastic zone.

The hybrid algorithm uses a blending function Y which is dependent on the instantaneous value of the modulus ratio h/G. G is the elastic shear modulus, h is the modulus function, and k is an algorithm constant. The blending function is shown in Equation (3.33).

$$\Psi = 1 - \exp\left(-k \frac{3}{2} \frac{h}{G} \right) \tag{3.33}$$

In the hybrid algorithm neither the assumption of zero strain rate in the cutting direction $\dot{e}_{xx} = 0$ [68] nor the assumption of elastic stress in the cutting direction $\dot{s}_{xx} = \dot{s}^*_{xx}$ [69] are assumed during plastic flow. For elastic-plastic loading, the blending function is used to describe the strain rate in the rolling/cutting direction as shown in Equation (3.34). Similarly, for the plane strain condition transverse to the rolling/cutting direction, the strain rate expression is given by Equation (3.35). Both equations are modified from the original expressions in [67] to account for thermal strain in the present application.

$$\begin{aligned} \dot{e}_{xx} &= \frac{1}{E}\left[\dot{s}_{xx} - n\left(\dot{s}_{yy} + \dot{s}^*_{zz} \right) \right] + a\Delta T + \frac{1}{h}\left(\dot{s}_{xx} n_{xx} + \dot{s}_{yy} n_{yy} + \dot{s}^*_{zz} n_{zz} + 2\dot{t}^*_{xz} n_{xz} \right) n_{xx} \\ &= \Psi\left(\frac{1}{E}\left[\dot{s}^*_{xx} - n\left(\dot{s}_{yy} + \dot{s}^*_{zz} \right) \right] + a\Delta T + \frac{1}{h}\left(\dot{s}^*_{xx} n_{xx} + \dot{s}_{yy} n_{yy} + \dot{s}^*_{zz} n_{zz} + 2\dot{t}^*_{xz} n_{xz} \right) n_{xx} \right) \end{aligned} \tag{3.34}$$

$$\dot{e}_{yy} = \frac{1}{E}\left[\dot{s}_{yy} - n\left(\dot{s}_{xx} + \dot{s}^*_{zz} \right) \right] + a\Delta T + \frac{1}{h}\left(\dot{s}_{xx} n_{xx} + \dot{s}_{yy} n_{yy} + \dot{s}^*_{zz} n_{zz} + 2\dot{t}^*_{xz} n_{xz} \right) n_{yy} = 0 \tag{3.35}$$

The above equations are solved simultaneously to determine the increments in stress for $\dot{s}_{xx}$ and $\dot{s}_{yy}$. The expressions are integrated over the passage of the load to determine the residual stresses due to cutting.

Additional equations necessary for implementing the incremental plasticity model are shown in Table 3.4. $\langle\ \rangle$ is the MacCauley bracket and is defined as $\langle x\rangle = 0.5(x + |x|)$. The plastic modulus function h determines the rate of material hardening.

Table 3.4 Equations used in incremental plasticity

Equation Description	Equation
Von Mises yield surface	$F = \frac{3}{2}(S_{ij} - a_{ij})(S_{ij} - a_{ij}) - R^2 = 0$
Deviatoric stress	$S_{ij} = s_{ij} - (s_{kk}/3)d_{ij}$
Plastic strain rate (normality flow rule)	$\dot{e}_{ij}^{p} = \frac{1}{h}\langle \dot{S}_{kl} n_{kl} \rangle n_{ij}$
Components of unit normal in plastic strain rate direction (on yield surface)	$n_{ij} = \frac{S_{ij} - a_{ij}}{\sqrt{2}k}$
Evolution of back stress for linear kinematic hardening	$\dot{a}_{ij} = \langle \dot{S}_{kl} n_{kl} \rangle n_{ij}$

In the model, residual stresses and strains should satisfy the boundary conditions prescribed by Merwin and Johnson [23] shown in Equation (3.36).

$$\begin{array}{cccc} (e_x)_r = 0 & (s_x)_r = f_1(z) & (e_y)_r = 0 & (s_y)_r = f_2(z) \\ (e_z)_r = f_3(z) & (s_z)_r = 0 & (g_{xz})_r = f_4(z) & (t_{xz})_r = 0 \end{array} \tag{3.36}$$

Meeting these boundary conditions after the passage of the load is necessary because no effort is made to maintain equilibrium during the loading cycle. Any non-zero components s_{zz}^{R}, t_{xz}^{R}, e_{xx}^{R}, and T^{R} are incrementally relaxed until the boundary conditions are met. If M steps are used for the relaxation process, then the stress increments are

$$\Delta s_{zz} = -\frac{s_{zz}^{R}}{M}, \qquad \Delta t_{xz} = -\frac{t_{xz}^{R}}{M}, \qquad \Delta e_{xx} = -\frac{e_{xx}^{R}}{M}, \qquad \Delta T = -\frac{T^{R}}{M} \quad . \tag{3.37}$$

At the end of the relaxation procedure, both s_{xx} and s_{yy} will be non-zero. These values are the true residual stresses that remain in the body.

During relaxation, there are two possibilities for material behavior: purely elastic relaxation and elastic-plastic relaxation. For purely elastic relaxation, $F < 0$ or $F = 0$ and $dS_{ij}n_{ij} \geq 0$. The elastic relaxation increments for s_{xx} and s_{yy} are given by Equation (3.38). For elastic-plastic relaxation, Equations (3.34) and (3.35) are solved for stress increments Δs_{xx} and Δs_{yy}, where Δ's replace the time derivatives.

$$\Delta s_{xx} = \frac{E\Delta e_{xx} + (1+n)(\Delta s_{zz} n - Ea\Delta T)}{(1-n^2)}$$
$$\Delta s_{yy} = \frac{nE\Delta e_{xx} + (1+n)(\Delta s_{zz} n - Ea\Delta T)}{(1-n^2)} \qquad (3.38)$$

3.3.2 Residual Stress Modeling Behavioral Analysis

A typical residual stress profile from the predictive model is shown in Figure 3.23. The model predicts residual stresses in the direction of the cut and transverse to cut direction. The prediction is two dimensional on the surface and at every level beneath the surface.

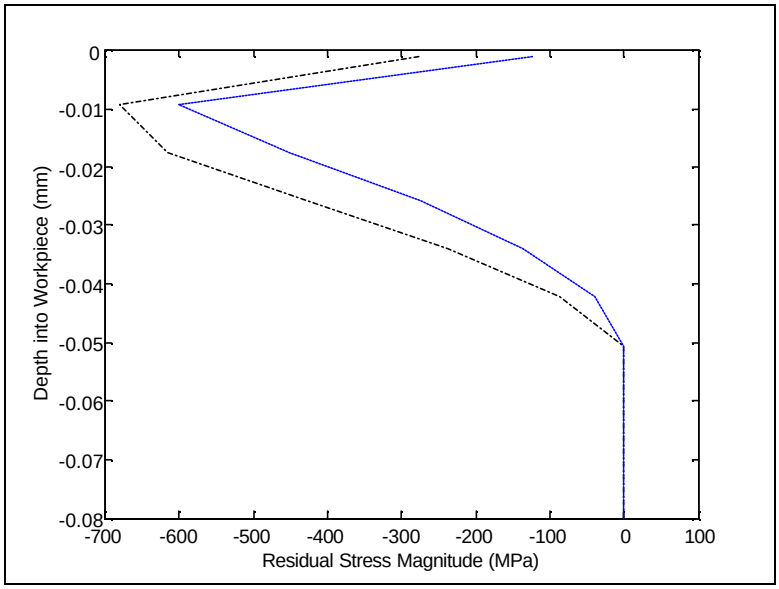

Figure 3.23 Typical residual stress profile produced from predictive model

A sensitivity analysis of model parameters on residual stress predictions has been performed. Four model inputs are used as independent variables. The variables are chosen to capture the effect of user input parameters on the behavior of the model. They include material flow stress parameters *C* and *m*, size of the tool edge *ER*, and the coefficient of friction or friction factor *mu*. The friction factor is treated as the friction between the tool and chip (Equation (3.14) in Chapter 3) and also as the friction factor between the tool and the workpiece (Equation (3.30) in Chapter 3). The levels for each factor are listed in Table 3.5.

Table 3.5 Residual stress input parameter levels

Variable	Low	High
C	0.015	0.025
m	0.6	0.8
ER (mm)	0.005	0.051
mu	0.4	0.9

The output responses of the model are shown below. The residual stress areas are chosen to capture the overall residual stress profile in terms of the tensile or compressive behavior for both the cut and transverse directions. The depth parameter is the location of maximum compressive residual stress.

- Depth – depth of maximum compressive residual stress into workpiece
- ACP – area of tensile residual stress in cut direction
- ACM – area of compressive residual stress in cut direction
- ATP – area of tensile residual stress in transverse direction
- ATM – area of compressive residual stress in cut direction

The main effects results for *Depth* are shown in Figure 3.24. The depth of the maximum compressive residual stress is strongly influenced by the friction coefficient and edge radius. These values directly (temperature, surface shear stress) and indirectly (cutting forces) determine the stress loading history of the workpiece. Both thermal and mechanical stresses have a bearing on the maximum depth of compressive residual stress. They are less dependent on material behavior and more dependent on the loading conditions. The actual values of the stresses however, are subject to the material behavior.

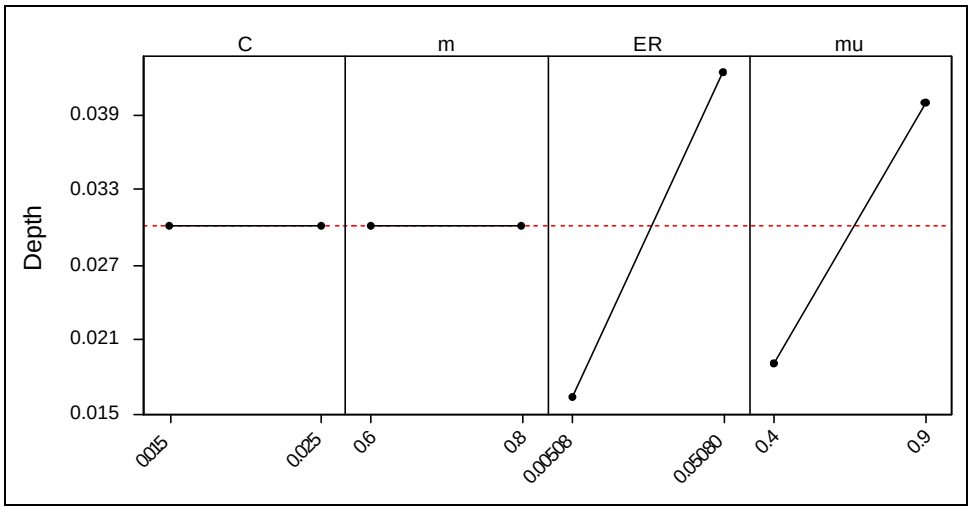

Figure 3.24 Main effects plot for *Depth* in orthogonal cutting

The main effects plots for the residual stress areas in the cutting direction are shown Figure 3.25 and Figure 3.26. The area of compressive residual stress in the cutting direction *ACM* is most noticeably affected by the edge radius and the friction. Larger values of edge radius result in higher levels of mechanical load compared to thermal load. The mechanical load due to the edge radius contributes to compressive residual stress formation. In contrast to the edge radius, larger values for friction impart more tensile character in the residual stress profile. This is due to the decrease in the shear angle caused by higher friction, larger shear loads, and higher temperatures in the workpiece. These factors play a role in the more tensile residual stresses predicted from the model. The influence of the thermal parameter *m* is interesting to note. It shows the impact of temperature on the flow stress of the material, which is an important parameter in the incremental plasticity modeling of residual stress.

The area of tensile residual stress in the cutting direction ACP is mostly affected by the friction coefficient. As mentioned previously, an increase in the friction coefficient results in an increase in the tensile character of the residual stress profile. A

decrease in the amount of compressive residual stress is captured as an increase in tensile residual stress.

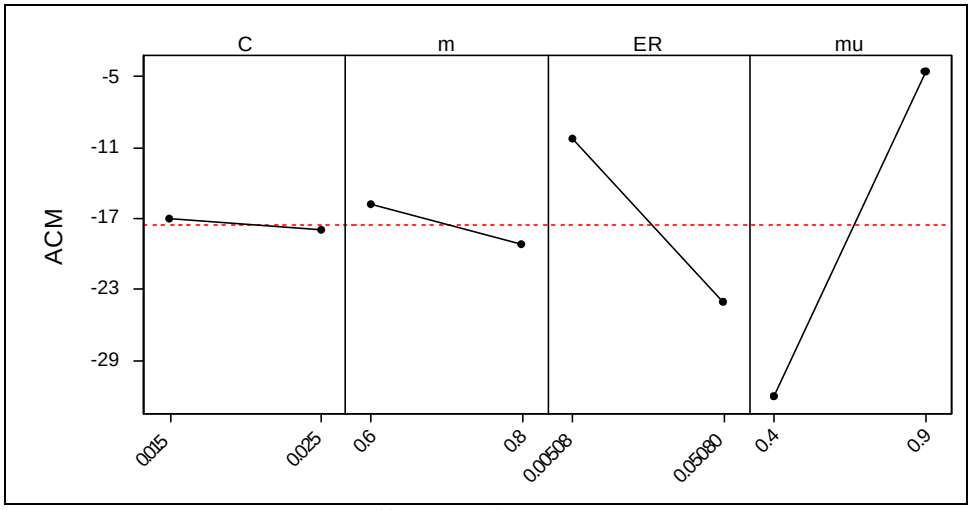

Figure 3.25 Main effects plot for *ACM* in orthogonal cutting

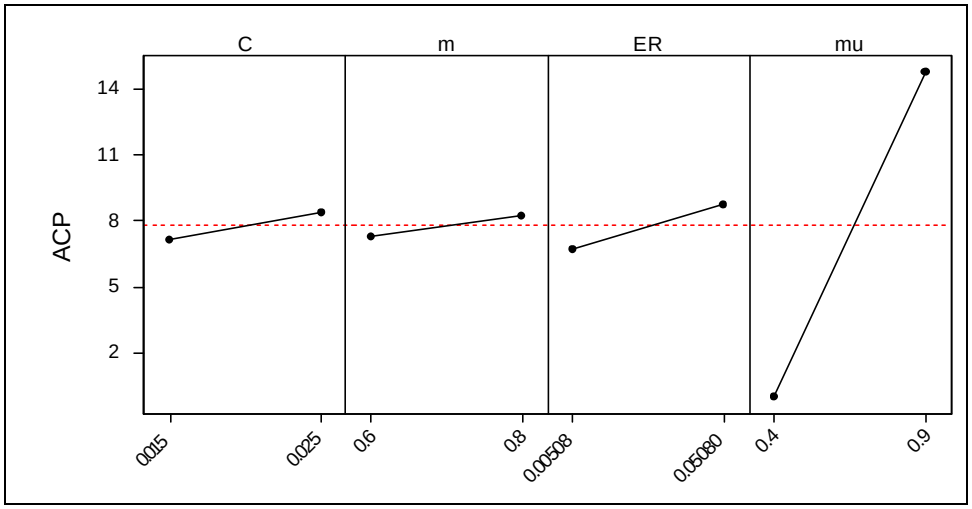

Figure 3.26 Main effects plot for *ACP* in orthogonal cutting

The main effects plots for the residual stress areas in the transverse direction are shown in Figure 3.27 and Figure 3.28. Similar to the residual stress areas in the cut direction, the residual stress areas in the transverse direction are affected by every parameter to some degree. The dominant factors are the friction coefficient and the edge radius. These results show that like the residual stresses in the cutting direction, the residual stresses in the transverse direction are affected by the behavior of the material under thermo-

mechanical loading. The maximum surface temperature is also significant in the residual stress profile in that it has a bearing on whether the residual stresses are tensile or compressive. A summary of the main effects for the residual stress results is provided in Table 3.6.

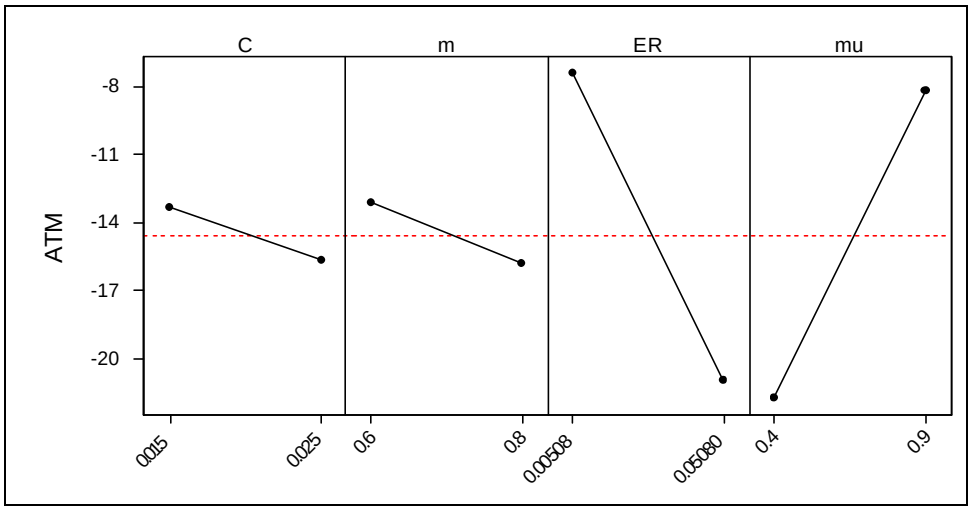

Figure 3.27 Main effects plot for *ATM* in orthogonal cutting

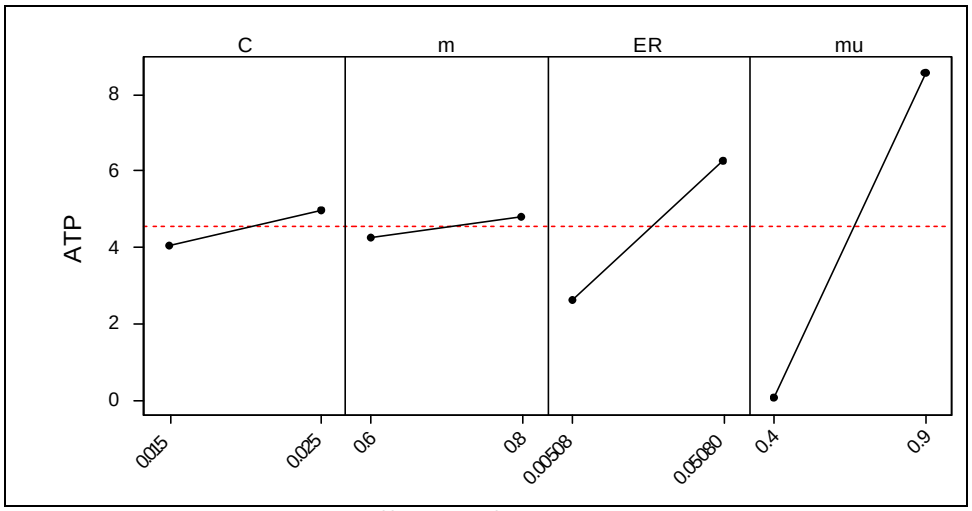

Figure 3.28 Main effects plot for *ATP* in orthogonal cutting

Table 3.6 Summary of effect of increasing input variables on *atp, atm, acp, and acm*

Input Variable	*ACP*	*ACM*	*ATP*	*ATM*
C	slight increase	n/c	slight increase	increase
m	slight increase	slight increase	slight increase	increase
ER	slight increase	increase	increase	increase
mu	increase	decrease	increase	decrease
Comment	▪ Friction has a strong influence on overall residual stress profiles ▪ Large edge radius results in larger values of compressive residual stress ▪ The two Johnson-Cook parameters *C* and *m* directly influence the plastic behavior of the material under thermo-mechanical loading. ▪ *m* shows the impact of temperature on the flow stress of the material ▪ Increasing friction results in higher levels of tensile residual stress due to the higher forces and shear stresses in the machined part			

The sensitivity analysis of residual stress paramters shows that for almost every model output, the friction coefficient *mu* and the edge radius *ER* have a pronounced impact on all outputs. This is due to the effect that friction plays on the inputs into the residual stress prediction. A higher friction coefficient results in higher cutting forces. The higher cutting forces result in higher temperatures and plastic deformation in the workpiece.

3.4 Interpretation of the Residual Stress Profile

As mentioned in Chapter 2, Jacobus [22] presented an approach to understanding the residual stress profile. Because of the importance in assessing the impact of the combination of mechanical and thermal loading on the residual stress profile, an overview of the descriptive model is provided.

Jacobus suggested the workpiece is comprised of distinct layers as shown in Figure 3.29. Layer *S* corresponds to the surface and near-surface layers of the workpiece where both thermal and mechanical effects are significant. Layer *D* represents the region where only mechanical loads are significant. Layer *B* represents the remainder of the workpiece where residual stress magnitudes are negligible.

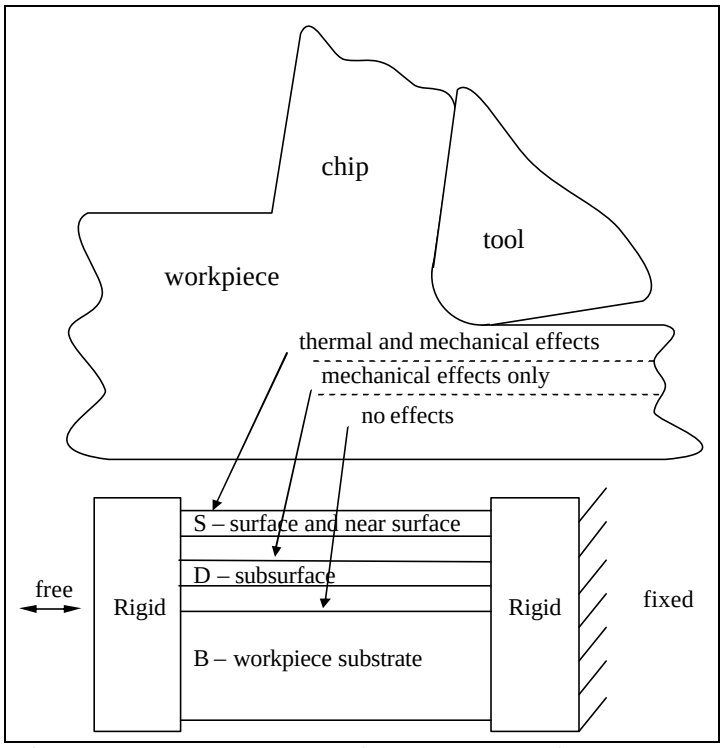

Figure 3.29 Adapted from Jacobus [22]. Schematic for development of machining-induced residual stress

In modeling the elastic constraint imposed on each layer by its neighbors, rigid supports are fixed to the end of each of the layers, with one rigid support fixed and the other free to translate. The total strain in the *S* layer is the sum of elastic strain e_S^E, plastic strain e_S^P, and thermal strain e_S^T.

$$e_S = e_S^E + e_S^P + e_S^T \tag{3.39}$$

In a similar vein, the total strain in layer *D* where only mechanical effects are significant may be written as the sum of elastic and plastic components.

$$e_D = e_D^E + e_D^P \tag{3.40}$$

The strain in the workpiece substrate is purely elastic and given by Equation (3.41).

$$e_B = e_B^E \tag{3.41}$$

The constraints require that the total strains be equal in each of the layers.

$$e_S = e_D = e_B \tag{3.42}$$

Equilibrium of the structure without external loading is given by

$$s_S d_S + s_D d_D + s_B d_B = 0 \tag{3.43}$$

Where d_S is the thickness of the surface/near-surface layer, d_D is the thickness of the sub-surface layer, and d_B is the thickness of the bulk of the workpiece. After the workpiece has cooled, the thermal strain e_S^T will be zero. Equation (3.42) can then be re-written as

$$\frac{s_S^r}{E} + e_S^P = \frac{s_D^r}{E} + e_D^P = \frac{s_B^r}{E} \tag{3.44}$$

where the superscript r indicates residual stresses. Simultaneous consideration of compatibility and equilibrium results in the expression for residual stresses in the surface/near-surface layer.

$$s_S^r = -Ee_S^P \frac{d_D + d_B}{d_S + d_D + d_B} + Ee_D^P \frac{d_D}{d_S + d_D + d_B} \tag{3.45}$$

For conditions where the bulk of the workpiece is much larger than the residual stressed zones, ($d_S << d_B$ and $d_D << d_B$), Equation (3.45) can be approximated by

$$s_S^r \approx -Ee_S^P \tag{3.46}$$

Similarly, expressions for residual stresses in the sub-surface and bulk layer are approximated by Equation (3.47) and Equation (3.48), respectively.

$$s_D^r \approx -Ee_D^P \tag{3.47}$$

$$s_B^r \approx 0 \tag{3.48}$$

During the cutting process, thermal and plastic strains exist in the surface/near-surface layer. If the elastic strains in the surface/near-surface and sub-surface layers are of similar value, then

$$e_S^P = e_D^P - e_S^T . \tag{3.49}$$

Since the temperature always increases in the workpiece as a result of cutting, the thermal strains in the surface/near-surface layer are non-negative. Assuming the flow of material around the tool is continuous the far-field boundary conditions require that $\left|e_S^P\right| \geq \left|e_D^P\right| \geq 0$ in the absence of thermal effects. Another explanation for this condition is that the magnitude of the sub-surface plastic strain is always greater than or equal to that of the surface/near-surface plastic strain.

Jacobus proposed the following scenarios that are possible for machining-induced residual stress.

- Case 1: $e_D^P > e_S^T \geq 0$. From the compatibility condition in Equation (3.49) and considering thermal strains are non-negative, $e_S^P > 0$. Consequently, the surface/near-surface residual stress $s_S^r < 0$. For the sub-surface layer, the residual stress is $s_D^r < 0$. The results are shown in Figure 3.30.
- Case 2: $e_S^T > e_D^P > 0$. From the compatibility condition, $e_S^P < 0$. Therefore, the surface/near-surface residual stress $s_S^r > 0$. The residual stress in the subsurface $s_D^r < 0$. This condition results in tensile residual

stresses near the surface and compressive in the sub-surface. The residual stress profile is illustrated in Figure 3.30.

- Case 3: $e_D^P < 0$. This condition results in $e_S^P \le e_D^P < 0$ and residual stresses $s_S^r \ge s_D^r > 0$. The residual stresses in all the layers are tensile. The profile is provided in Figure 3.30.

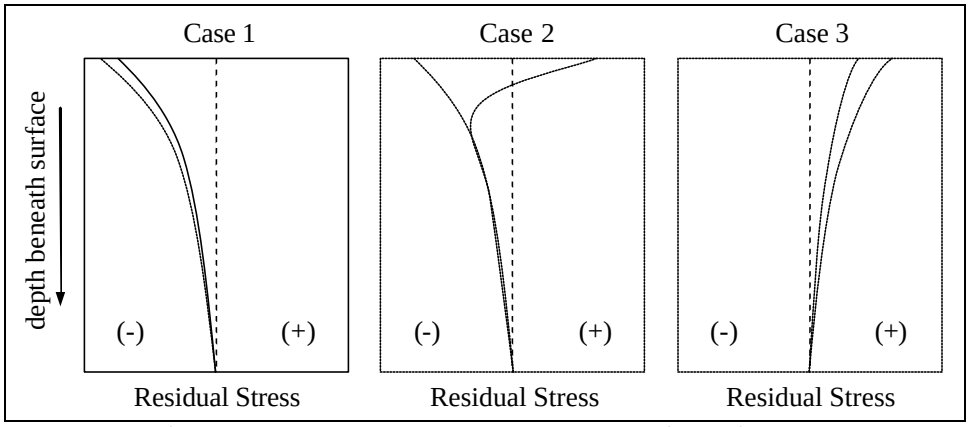

Figure 3.30 Adapted from Jacobus [22]. Possible residual stress fields from one-dimensional model. Dotted lines indicate residual stresses from purely mechanical loads. Solid lines indicate residual stresses from combined thermal and mechanical effects.

The modeling proposed by Jacobus and referenced here provides a quantitative rationale for the potential residual stress profiles generated by machining in the cutting direction. When coupling the effects of plastic and thermal strains, the temperature increases are shown to increase the tensile character of the residual stress profile which is consistent with published experimental data.

3.5 Summary

The information presented in this chapter provides the general technique used to predict residual stresses generated from machining. Section 3.1 describes the methods used to predict cutting forces in orthogonal cutting. Two sources of cutting forces are

considered: chip formation forces and plowing forces. The chip formation forces are the basis for determining stresses in the shear zone. The plowing forces contribute to the stresses between the tool and workpiece. A sensitivity analysis of the cutting force model shows that chip formation forces are dependent on the cutting parameters while the plowing forces are primarily affected by the size of the cutting edge radius.

Section 3.2 introduces the method of predicting the temperature rise in the workpiece due to cutting. The methods are based on the modeling techniques developed by Hou and Komanduri [59, 60] considering moving heat sources. Like the cutting force predictions, two sources of heat are assumed to generate the temperature rise in the machined part: the shear zone and the rubbing between the tool and the workpiece. The cutting forces predicted from Section 3.1 are used to determine the magnitude of the heat intensities used for temperature predictions. A sensitivity analysis of the cutting parameters shows that increasing the edge radius results in higher temperatures while increasing cutting speed, depth of cut, and rake angle result in lower average temperatures in the vicinity of the tool tip.

Section 3.3 of the chapter describes the technique used to predict residual stresses from cutting. The modeling incorporates both mechanical and thermal loads in an incremental plasticity model. The material behavior is assumed to be dependent on strain, strain rate, and temperature. Additionally, material hardening is also captured. The model parameters including friction, edge radius, and the Johnson-Cook parameters for strain rate and temperature are all found to influence the resulting residual stress profiles.

Section 3.4 presents the work of Jacobus [22] in establishing a rationale for the shape profile of residual stresses due to combined thermal and mechanical loading. The residual stress profiles are dependent on the amount of thermal and mechanical loading and the position of the loading. Three scenarios are possible for residual stress profiles generated from machining.

In the following chapters, details specific to the type of machining such as orthogonal cutting, milling, and turning will be provided in order to implement the models presented in this chapter. In particular, the details relevant to implementing the model for different geometries encountered in turning and milling will be discussed.

CHAPTER 4

MODELING RESULTS FOR ORTHOGONAL CUTTING

In this chapter, the modeling techniques described in the Chapter 3 are implemented and compared with experimental data for several materials. The materials modeled include Ti 6Al-4V, AISI 316L, and AISI 4340. Cutting force predictions are compared with experimental data for machining Ti 6Al-4V and AISI 316L. Cutting temperatures predictions are presented for each of the materials. Residual stress predictions are made by combining the results from the force and temperature models.

Computer code used to execute the residual stress model is developed in Matlab 7.1. The programs are executed on a Dell Latitude D610 with a Pentium M 1.86 GHz processor and 512 MB of memory. Average run times for orthogonal cutting are approximately 60 seconds for force, temperature, and residual stress predictions.

Johnson-Cook flow stress parameters for the materials used for model predictions are listed in Table 4.1. Additional material properties used to model residual stresses and forces are provided in Table 4.2.

Table 4.1 Johnson-Cook flow stress paramters for materials used

Material	A (MPa)	B (MPa)	C	m	n
Ti 6Al-4V [70]	998	653	0.020	0.70	0.45
AISI 316L [71]	305	441	0.057	1.04	0.10
AISI 4340 [44]	792	510	0.014	1.03	0.26

Table 4.2 Additional material properties used in the model

Material	E (GPa)	ν	H (GPa)	ρ (kg/m^3)	k (W/m°C)	C_P (J/kg°C)	α ($°C^{-1}$)	T_m (°C)
Ti 6Al-4V	114	0.33	30	4420	6.7	560	9.2e-6	1668
AISI 316L	193	0.28	60	7750	16.2	500	16.2e-6	1400
AISI 4340	200	0.28	70	7800	40.0	500	11.0e-6	1400

4.1 Cutting Force Validation for Orthogonal Cutting

Cutting force data from Budak and Altintas [72] is used to validate the force models for orthogonal cutting. The conditions for the experiments are shown in Table 4.3. The cutting edge radius for the predictions is assumed to be 0.013 mm.

Table 4.3 Cutting conditions for orthogonal cutting [72]

Case	Rake Angle (deg)	Speed (m/s)	Depth of Cut (mm)	Width of Cut (mm)	Edge Radius (mm)
1	8	0.500	0.025-0.153	3.8	0.013
2	12	0.500	0.025-0.153	3.8	0.013
3	15	0.500	0.025-0.153	3.8	0.013

The cutting force predictions and experimental results are shown in Figure 4.1 to Figure 4.3. The figures show that the predicted values are consistent with the experimental values for the conditions tested. For all cases, the predicted cutting forces and experimental results are close, with the largest difference of around 25%. These results show that the combination of chip formation and plowing forces used to predict total cutting forces in orthogonal cutting performs well for the range of cases used in the Budak and Altintas experiments.

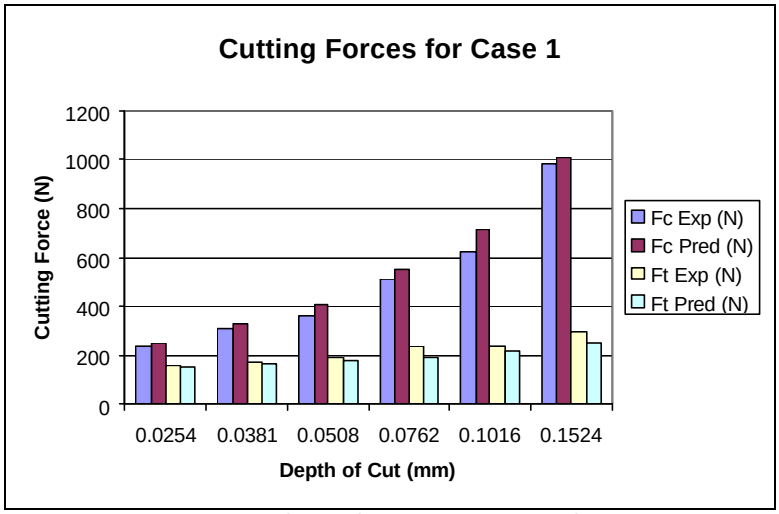

Figure 4.1 Cutting forces for varying depths of cut: Case 1

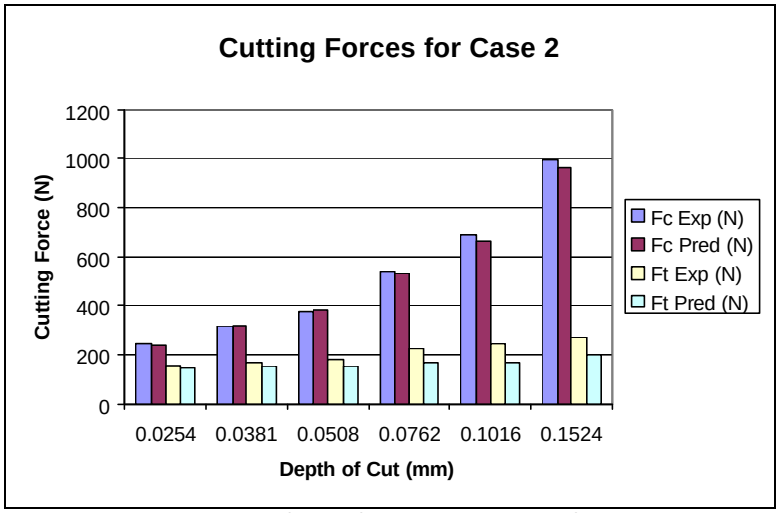

Figure 4.2 Cutting forces for varying depths of cut: Case 2

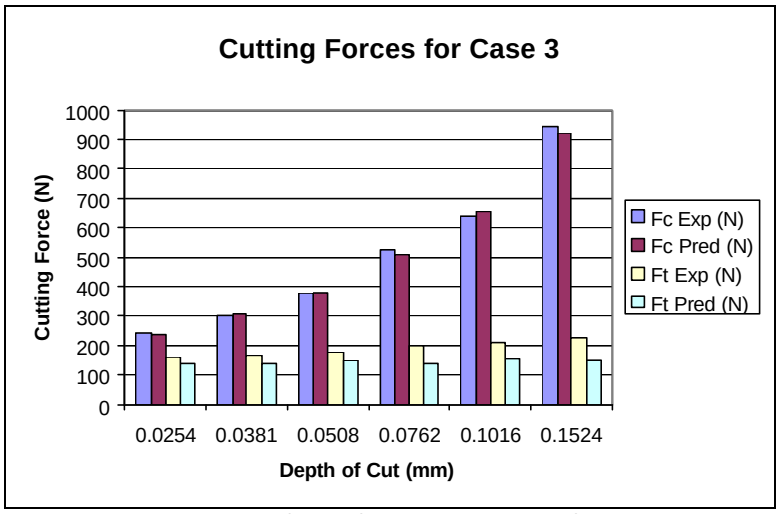

Figure 4.3 Cutting forces for varying depths of cut: Case 3

Additional comparisons of orthogonal cutting of Ti 6Al-4V are made with broaching data collected from the MAI program [73]. The conditions for those tests are shown in Table 4.4. The conditions are similar to those used by Budak and Altintas. However, the cutting speeds are slower and the maximum depth of cut is larger.

Table 4.4 Broaching conditions for Ti 6Al-4V

Case	Rake Angle (deg)	Speed (m/s)	Depth of Cut (mm)	Width of Cut (mm)	Edge Radius (mm)
4	12	0.152	0.064	7.0	0.013
5	12	0.152	0.102	7.0	0.013
6	12	0.152	0.254	7.0	0.013
7	12	0.330	0.064	7.0	0.013
8	12	0.330	0.102	7.0	0.013
9	12	0.330	0.254	7.0	0.013

The cutting force predictions for the MAI data are shown in Figure 4.4. The data are scaled with respect to the maximum predicted cutting force. Experimental data was not collected for Case 6; however, a prediction for that cutting condition is still presented. The figure illustrates that the forces in the cut direction are well predicted for each of the

cutting conditions except for Case 9. The depth of cut for Case 9 is 2.5× larger than Case 8. Assuming the shear stress of the material and the shear angle do not change significantly, then based on the predictive model, the cutting force in Case 9 should be approximately 2.5× larger than that of Case 8. However, the experimental data show that the force in the cut direction only increases by 54%. This result could indicate a depth of cut limitation in the predictive cutting force model for the conditions used in the experiments. Additionally, the broaching conditions for Case 9 were found to produce an unstable cutting condition [73].

The predictions for forces in the thrust direction capture the trend of increasing force for increasing depth of cut. However, the predicted forces are slightly larger than the measured forces. This can be attributed in part to the assumption of the size of the cutting edge radius. For the broaching conditions, the cutting edge radius is assumed to be 0.013 mm for the calculations. For a smaller edge radius, the thrust force values would be reduced, while the cutting force values would remain approximately unchanged.

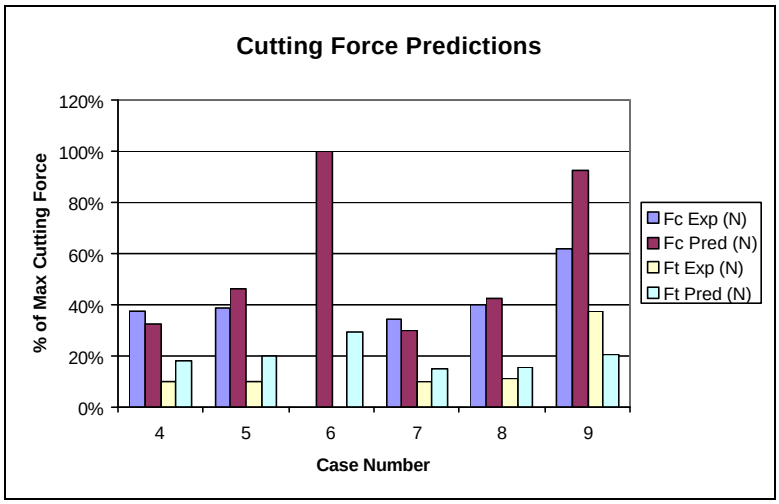

Figure 4.4 Force results from MAI experiments

Cutting force predictions are also made for AISI 316L austenitic stainless steel. The experimental conditions for the orthogonal cutting of AISI 316L stainless steel are given in Table 4.5. The conditions presented aim to capture the effect of increasing speed on the resulting cutting forces.

Table 4.5 Cutting conditions for predicting forces in AISI 316L [74]

Case	Tool	Material	Edge Radius (mm)	Width of Cut (mm)	Feed (mm/rev)	Speed (m/s)
10	KC950	AISI 316L	0.060	4	0.100	1.67
11	KC950	AISI 316L	0.060	4	0.100	2.08
12	KC950	AISI 316L	0.060	4	0.100	2.50
13	KC950	AISI 316L	0.060	4	0.100	3.33

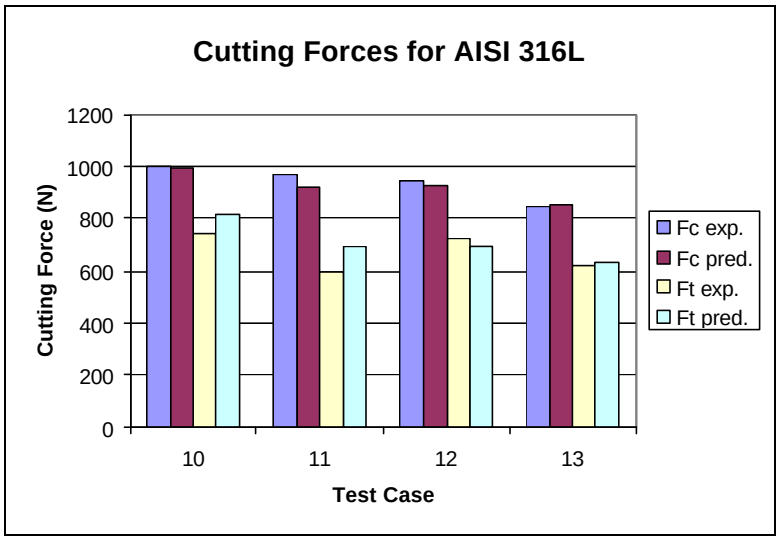

Figure 4.5 Cutting force comparisons for AISI 316L

The results show that an increase in cutting speed results in a decrease in cutting force. Higher cutting speeds produce higher temperatures in the shear zone. Consequently, the cutting forces decrease due to thermal softening. This trend is captured in the predictions as well as the experimental data. The cutting force model

performs well for the conditions in Cases 10-13 in predicting forces in both the cut and thrust directions.

4.2 Orthogonal Cutting Temperature Results

Cutting temperature predictions are made for the cutting conditions in Table 4.4, Table 4.5, and Table 4.7. The cutting forces are used to determine the heat intensity generated by cutting. As a result, the accuracy of the cutting temperatures is assumed to be related to the accuracy of the force prediction.

The following tables show the maximum surface temperature for each of the conditions described by Cases 4-9. The average temperature column in Table 4.6 represents the average temperature in the workpiece in a region 1.0 mm ahead and behind the tool tip and 0.125 mm beneath the workpiece surface. The temperature predictions assume reasonable values when considering the effects of both the oblique shear plane heat source as well as the rubbing heat source. A convective behavior in the direction of workpiece motion is observed.

Table 4.6 Temperature predictions for Cases 4-9

Case	Max. Surface Temp. (°C)	Avg. Temp. (°C)
4	383	98
5	391	109
6	397	121
7	394	91
8	388	96
9	371	97

The temperature predictions in Table 4.6 show an increase in cutting temperatures for increasing depths of cut at lower cutting speeds (Cases 4-6). However, for the higher cutting speed cases, the maximum surface temperature actually decreases. For higher cutting speeds, the cutting forces decrease due to thermal softening in the shear zone. The lower forces result in lower heat intensities calculated from Equations (3.22) and (3.23). Consequently, the temperature rise in the workpiece is lower while the temperature in the shear zone is higher.

Table 4.7 Cutting condtions for Cases 14-19 [22]

Case	Tool	Material	Edge Radius (mm)	Feed (mm/rev)	Width of Cut (mm)	Speed (m/s)
14	TPG-432	AISI 4340	0.025	0.100	3	5.00
15	TPG-432	AISI 4340	0.075	0.100	3	5.00
16	TPG-432	AISI 4340	0.025	0.200	3	5.00
17	TPG-432	AISI 4340	0.075	0.200	3	5.00
18	TPG-432	AISI 4340	0.050	0.150	3	5.00
19	TPG-432	AISI 4340	0.050	0.125	3	5.00

Table 4.8 Temperature predictions for Cases 14-19

Case	Max. Surface Temp. (°C)	Avg. Temp. (°C)
14	360	64
15	575	85
16	330	61
17	463	72
18	391	67
19	465	73

Similar results are found for temperature predictions of orthogonally cut AISI 4340 using the conditions in Table 4.7. The temperature predictions are shown in Table 4.8. The surface temperatures for machined AISI 4340 vary by a larger amount than the surface temperatures predicted for the other cases. This is due to the effect of the increased edge radius used in the particular test cases. For Case 14, the edge radius is 0.025 mm while the depth of cut is 0.100 mm. The overall effect on the cutting geometry due to the edge radius is minimal. The bulk of the cutting edge is still defined by the specified tool geometry. However, in Case 15, the edge radius is approximately the same size as the depth of cut. As a result, the effective rake angle is more negative. The more negative rake angle produces a lower shear angle during chip formation. For example, the predicted shear angle for Case 14 is approximately 26°. For Case 15, the predicted shear angle is 19°. The effect of a lower shear angle is higher cutting forces along with a larger heat source. These two effects combine to produce higher temperatures in the vicinity of the tool tip. These results are consistent with the behavioral analysis Section 3.2.2.

4.3 Orthogonal Cutting Residual Stress Results

Residual stress predictions are compared with experimental data for broached Ti-64, orthogonally cut AISI 4340, and orthogonally cut AISI 316L. The experimental data for Ti-64 only consists of surface residual stress measurements. Residual stress data for AISI 4340 and AISI 316L include the surface and sub-surface measurements.

The experimental data from the broaching operation is scaled with respect to the maximum residual stress at the surface in the cut direction. The data show residual

stresses on the surface that range from 73% of the maximum compressive residual stress for 0.064 mm depth of cut to 100% of the maximum for 0.254 mm depth of cut with negligible dependence on cutting speed. The predictions show a slight dependence on cutting speed for the surface residual stresses. However, the overall trends are within the range of experimental residual stress data.

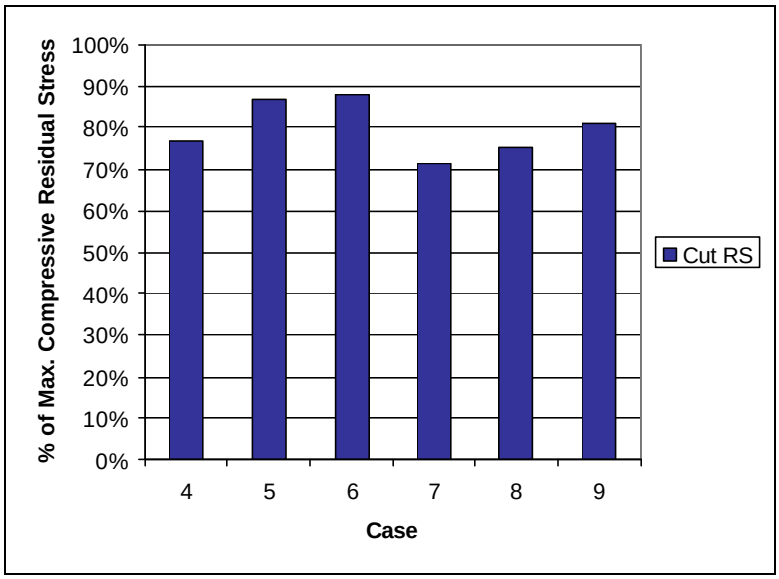

Figure 4.6 Surface residual stress values in cut direction for Cases 4-9

Sub-surface residual stress predictions are also made for Cases 4-9. Although sub-surface residual stress experimental data is not available for comparison, the model predictions are made to show the effect of varying cutting conditions on the sub-surface residual stress profiles. The results are presented in Figure 4.7. They indicate that the range of cutting speeds used for the broaching experiments has a minimal impact on the surface and sub-surface residual stresses. This is due in part to the low thermal conductivity of Ti-64. Since the majority of the heat generated by cutting does not penetrate into the workpiece, the difference in the temperature rise in the workpiece has minimal impact on the residual stress profiles.

In contrast to cutting speeds, however, variation in the depth of cut produces noticeable changes in the sub-surface residual stress profile. Increasing the depth of cut results in a larger chip formation zone or shear plane. The effect of which is a larger stressed zone. When combined with the thermal load and the plowing load, the results is a larger plastically deformed region beneath the surface of the workpiece, and consequently, deeper penetration of the machining-induced residual stress field.

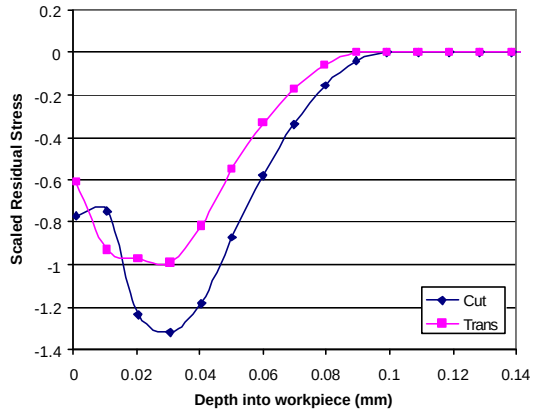

Case 4

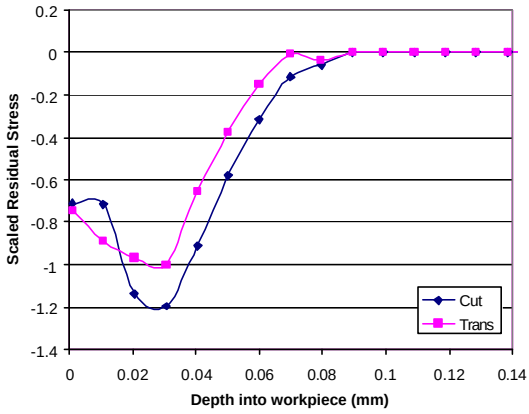

Case 7

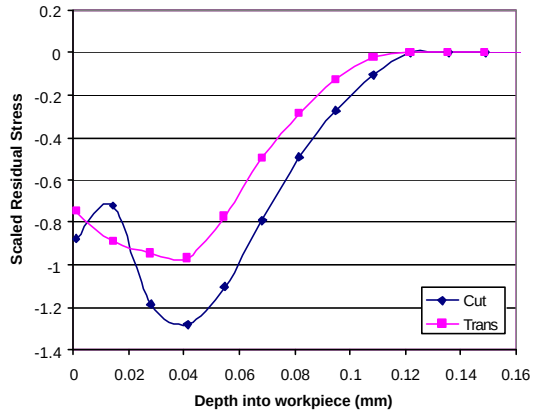

Case 5

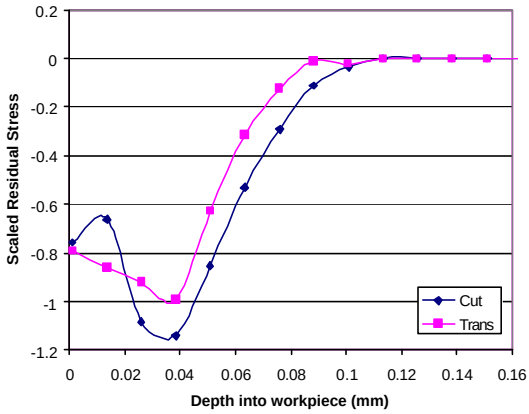

Case 8

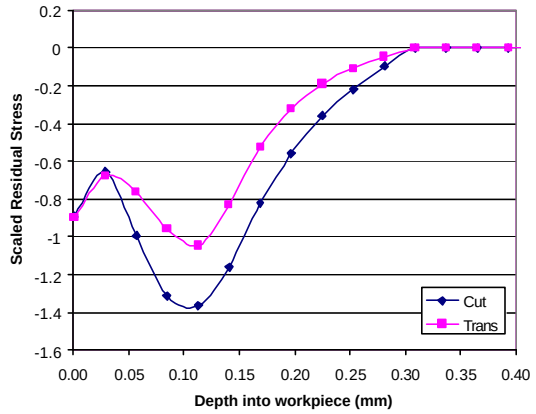

Case 6

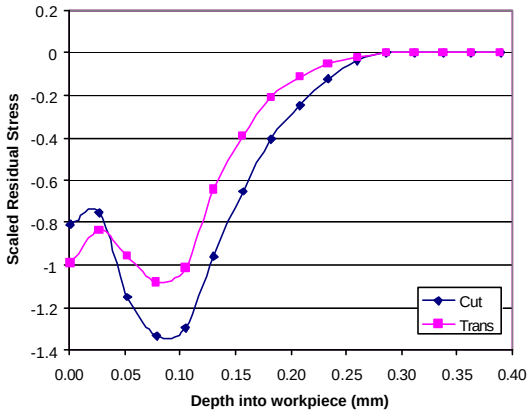

Case 9

Figure 4.7 Sub-surface residual stress predictions for Cases 4-9

The conditions used to generate machining-induced residual stress in AISI 316L differ slightly from the conditions used in the force predictions. Specifically, the depths

of cut (feed) are increased for the cutting conditions listed in Table 4.5. The conditions for residual stress predictions are listed in Table 4.9.

Table 4.9 Cutting conditions for predicting residual stresses in AISI 316L [74]

Case	Tool	Material	Edge Radius (mm)	Width of Cut (mm)	Feed (mm/rev)	Speed (m/s)
10	KC950	AISI 316L	0.060	4.000	0.100	1.67
11a	KC950	AISI 316L	0.060	4.000	0.100	2.08
12a	KC950	AISI 316L	0.060	4.000	0.200	2.08
13a	KC950	AISI 316L	0.060	4.000	0.250	2.08

Residual stress predictions for Cases 10-13a are shown in Figure 4.8 to Figure 4.11. Similar to the residual stress predictions for Ti-64, increasing the depth of cut increases the depth of penetration of the machining-induced residual stresses. This can be seen by comparing the results between Cases 11a and 13a. For example, the predicted residual stress diminishes to zero around 0.260 mm for a feed rate of 0.100 mm (Case 11a). For a feed rate of 0.250 mm, the residual stress reaches zero around 0.430 mm. The surface residual stresses remain relatively constant for increases in feed rate. The predictive model performs well in capturing the trends associated with the change in cutting depth.

The effect of feed can be explained from a modeling perspective. The increase in feed produces a larger depth of cut which results in a longer shear zone and a larger stressed region in the workpiece. Since the edge radius is assumed constant for each of the cutting conditions in the specified cases, the influence of the shear zone in the overall stress field produced by cutting is more prominent.

Increasing cutting speed in the range of speeds tested has minimal effect on the residual stress profile. This can be seen in comparison of Figure 4.8 to Figure 4.9. The minimal impact on the residual stress results is also captured in the predictive model. These results are also consistent with the experimental data pertaining to Ti-64.

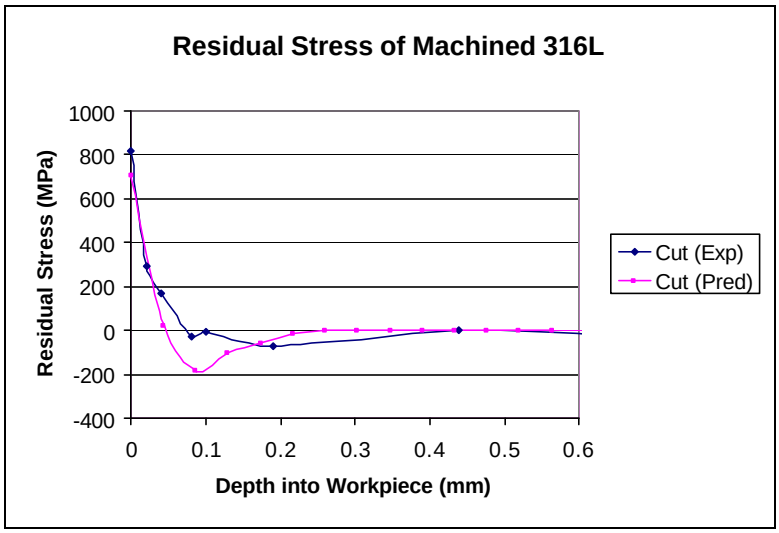

Figure 4.8 Residual stress predictions for Case 10

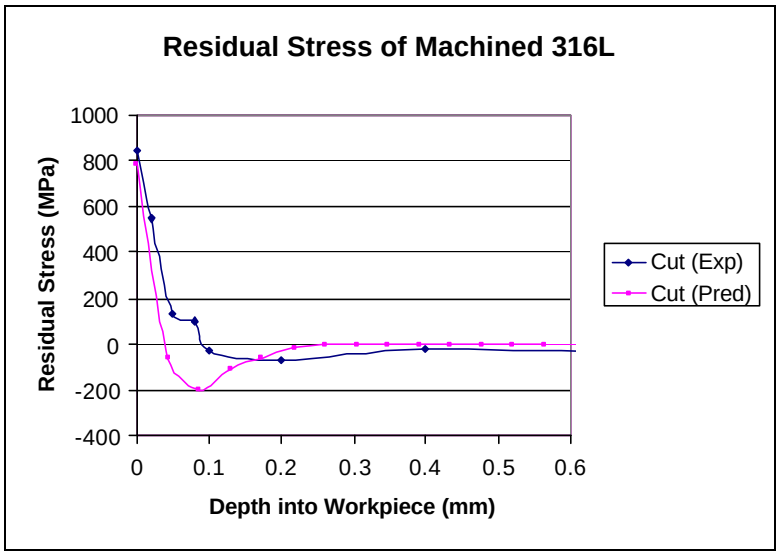

Figure 4.9 Residual stress predictions for Case 11a

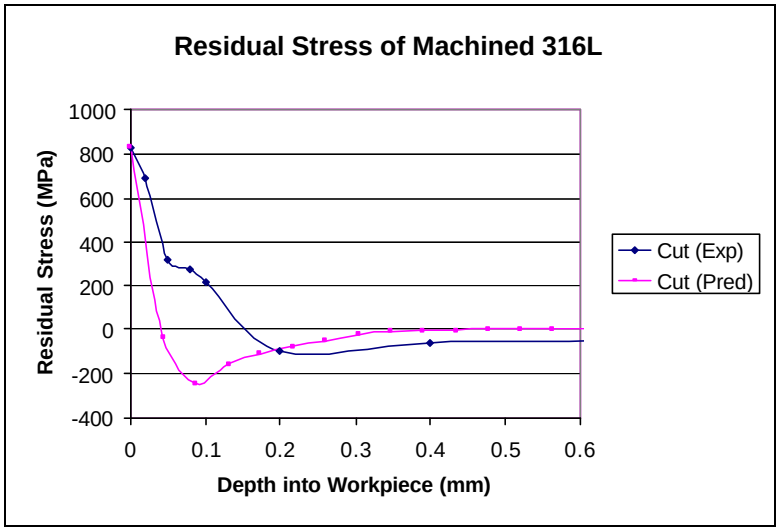

Figure 4.10 Residual stress predictions for Case 12a

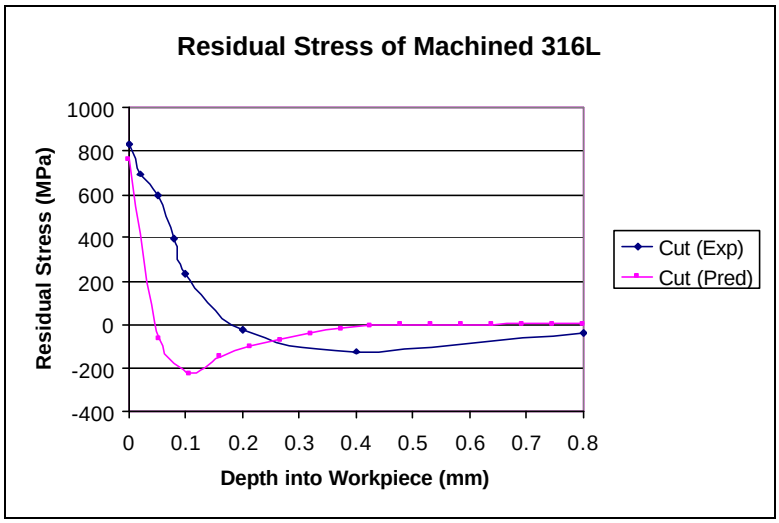

Figure 4.11 Residual stress predictions for Case 13a

Although the predicted trends are generally in line with the experimental data, the actual residual stress values deviate from the measured values in the sub-surface. The measured compressive residual stresses appear to penetrate deeper beneath the surface in a more gradual fashion than the predicted values. For example, the prediction for Case 10 (Figure 4.8) shows a peak compressive residual stress of approximately -200 MPa at a depth of 0.010 mm. The measured peak residual stress value is -66 MPa at a depth of 0.019 mm. This attribute is apparent in each of the cases.

The deviation is due in part to the mechanical loading history experienced by the material. The combined loads due to the tool edge and the shear zone contribute to the mechanical load. The size of the contact zone of the tool edge (Figure 3.19) relative to the shear zone load dictates the residual stress profile. In these cases, it is possible that the computation for the size of the tool width is under estimating the actual contact size. For a contact size that is smaller than the shear zone, the compressive profile will have a more pointed peak compared to a situation where the tool edge contact size is approximately the same size as the shear zone. Under those conditions, the residual stress profile will have a smoother curve.

The residual stress predictions for AISI 4340 steel are shown below. The depth of penetration of residual stresses for the 4340 steel is shallower than that for the AISI 316L. For each of the conditions examined, the residual stresses are of negligible magnitude by 0.200 mm below the surface. The general trends present in the measured residual stress profiles are also captured by the predictive model.

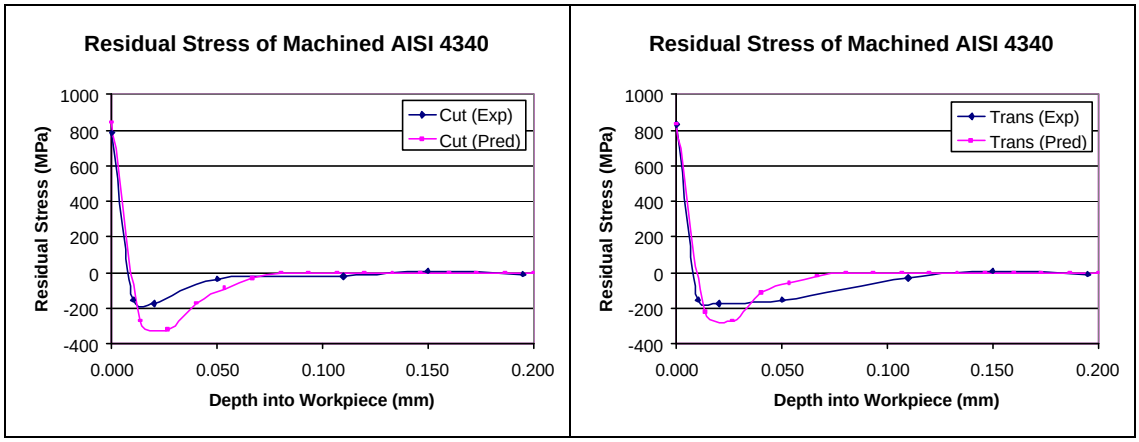

Figure 4.12 Residual stress predictions for cut and transverse directions for Case 14

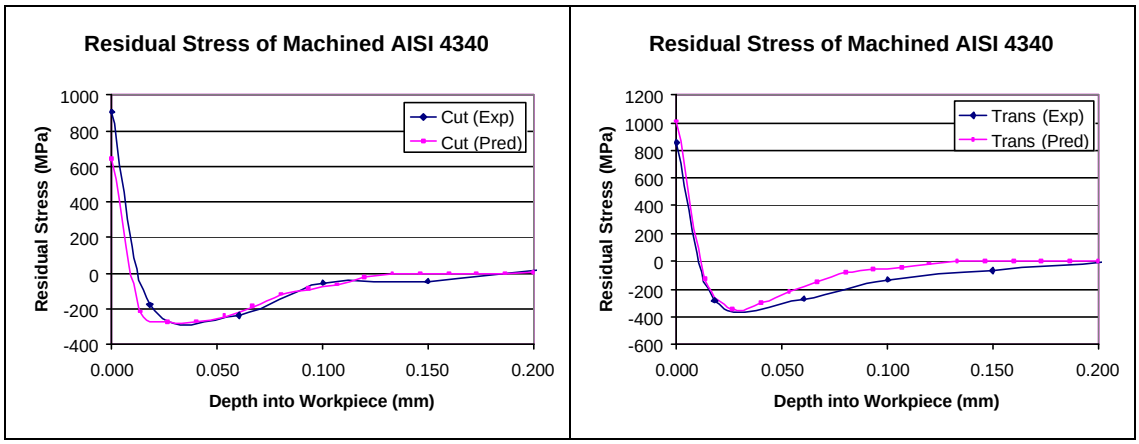

Figure 4.13 Residual stress predictions for cut and transverse directions for Case 15

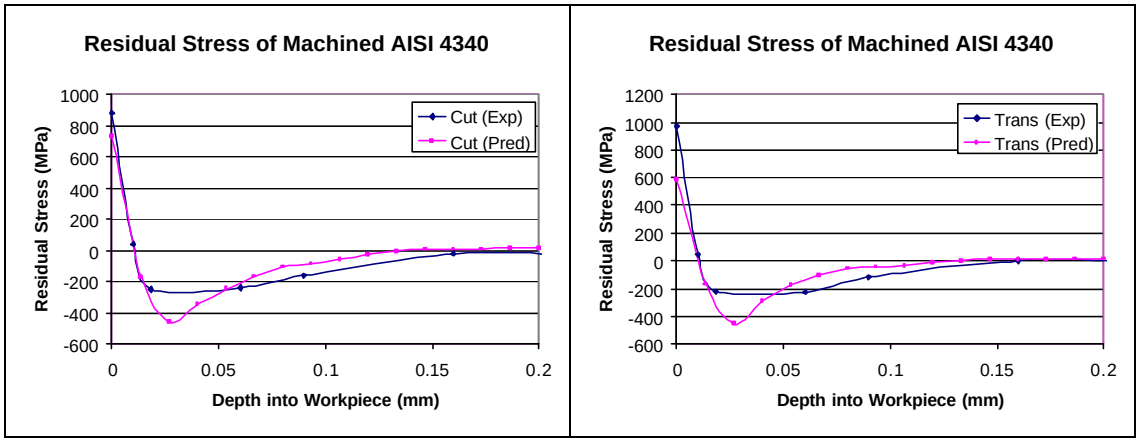

Figure 4.14 Residual stress predictions for cut and transverse directions for Case 16

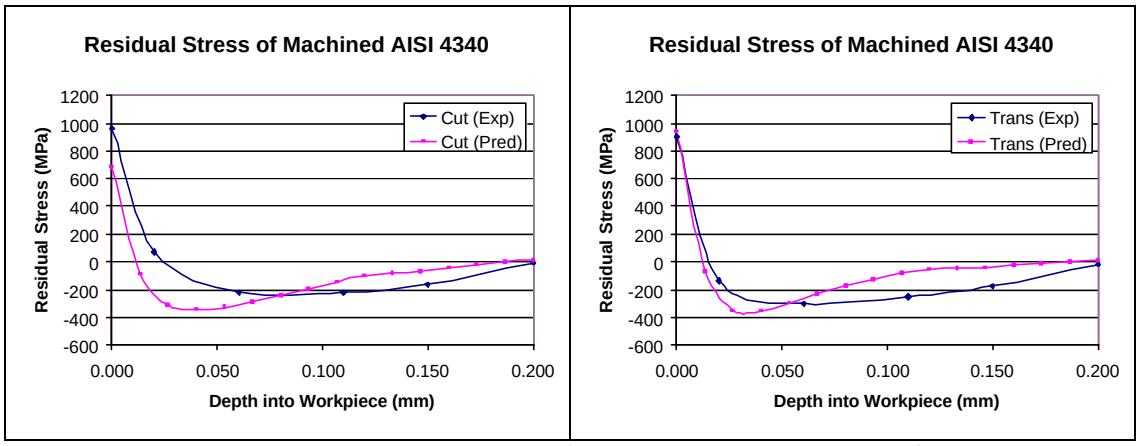

Figure 4.15 Residual stress predictions for cut and transverse directions for Case 17

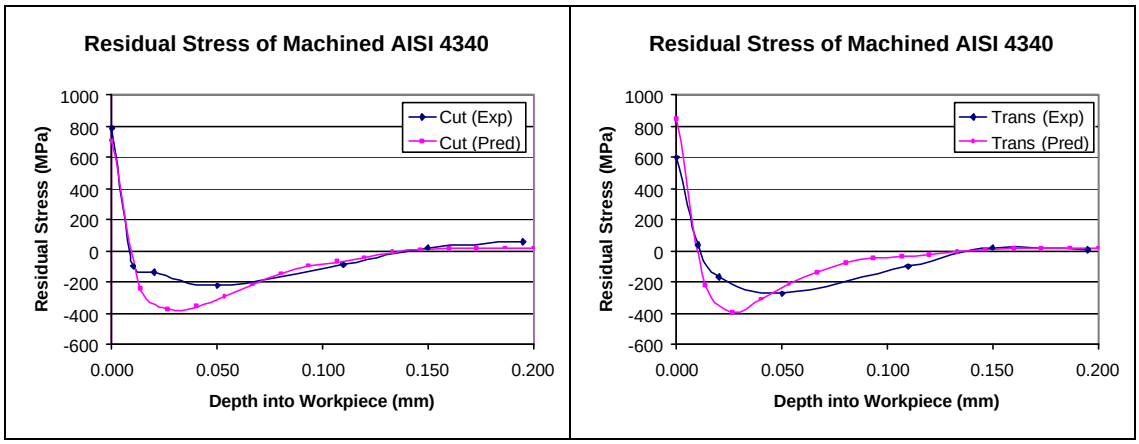

Figure 4.16 Residual stress predictions for cut and transverse directions for Case 18

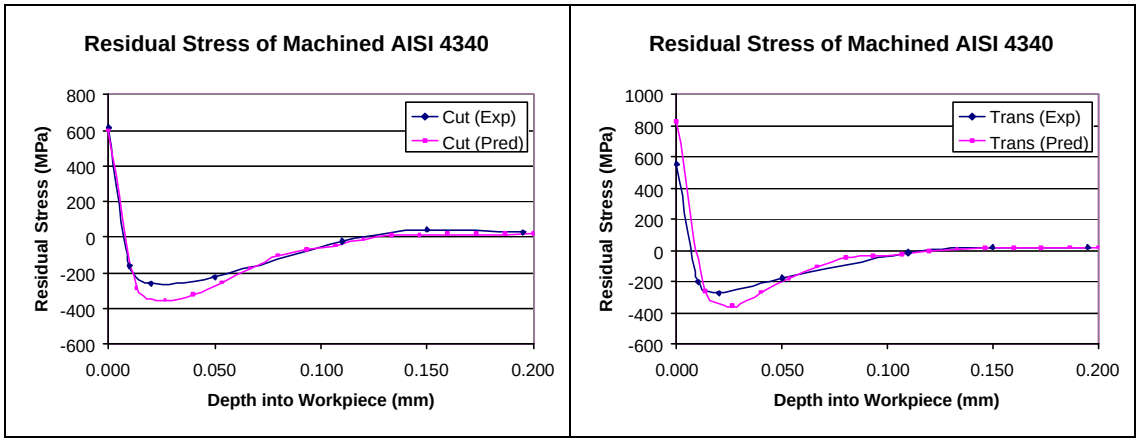

Figure 4.17 Residual stress predictions for cut and transverse directions for Case 19

The experimental data for the machined AISI 4340 illustrate the additional impact of the cutting edge radius on the residual stress formation. In Case 14, using a 0.025 mm hone radius tool, the residual stress is approximately 0 MPa beyond 0.100 mm. However, in Case 15 with a hone radius of 0.075 mm, the residual stress does not reach 0 MPa until approximately 0.200 mm beneath the cut surface. These results show that the roundness of the cutting edge increases the stressed region.

The residual stress predictions for the conditions listed in Cases 14 and 15 capture the impact of increasing the edge radius. The model predictions, like the experimental data, show an increase in the region of compressive residual stress beneath the workpiece surface for increased edge radius. This can be attributed to the effect of edge radius on

the contact region between the tool and the workpiece. Machining with a tool that has a larger hone radius results in higher cutting forces as well as a larger region of contact in the cutting zone. Consequently, the maximum depth of the sub-surface residual stress increases with increasing edge radius.

In Cases 16 and 17, the depth of cut is increased. Like the experimental data for AISI 316L, the data for AISI 4340 show an increase in the depth of residual stress due to machining for increasing depths of cut. Data for Cases 18 and 19 capture intermediate values of edge radius and depth of cut. The residual stress results for those two cases are similar to the other results for AISI 4340.

The experimental data and model predictions show tensile residual stresses on the surface machined samples. The tensile residual stresses indicate that the thermal effects are significant at the surface [75] and correspond to Case 2 in Figure 3.30.

4.4 Summary

In this chapter, the modeling approach proposed in Chapter 3 is applied to orthogonal cutting. Cutting forces are predicted for broaching Ti 6Al-4V as well as orthogonal cutting of AISI 316L. The cutting force predictions for AISI 316L agree very well with experimental data. Predictions of broaching forces for Ti 6Al-4V agree well for depths of cut between 0.065 mm and 0.102 mm. For the largest depth of cut of 0.254 mm, the cutting stability was found to decrease compared to the other conditions. As a result, the difference between the predicted cutting forces and the measured cutting forces is greater. The cutting force predictions consist of both chip formation and plowing forces. The plowing forces due to the roundness of the cutting edge contribute a

significant portion of to the predicted thrust forces, while the contribution to the forces in the cut direction is less pronounced.

Temperature predictions are made for the newly machined surface in the vicinity of the tool tip. The maximum temperature beneath the tool tip along with the average temperature around the tool tip is predicted. The predicted temperatures are reasonable for the machining conditions used. The cutting parameters that influence the temperature are the depth of cut and the edge radius of the tool. Both of these parameters affect the shear angle and the resulting temperature profile in the workpiece.

Residual stress predictions are made for broaching Ti 6Al-4V and orthogonal cutting of AISI 4340 and AISI 316L. The experimental data for broaching is limited to surface residual stress measurements. The predicted surface residual stresses are within the range of measured residual stresses for Ti 6Al-4V. The results are encouraging in the sense that the trends of residual stress are captured. For the steels, full residual stress profile data is used for comparison. The predictions agree well with the experimental data in the sense that the model captures the effects of edge radius as well as depth of cut on the residual stress profile generated by orthogonal cutting. The predicted magnitudes of residual stress as well as the depth of penetration are consistent with the experimental data.

CHAPTER 5

MODELING RESIDUAL STRESSES IN MILLING

5.1 Introduction

In this chapter, the modeling techniques for predicting residual stresses in milling are presented along with experimental validation. Modeling milling is an extension of the orthogonal cutting model described in Chapter 3. Additionally, the effect of cutting fluid is implemented in the models for predicting forces and temperatures. Experimental data from milling Ti 6Al-4V are compared with model predictions. The data consists of milling forces for both slot and finish milling. Residual stress measurements are presented for slot milling and face milling.

5.2 Milling Force Modeling

The milling force model is an extension of the orthogonal force model. Geometric considerations must be made to use the oblique/orthogonal models described in the previous section to predict milling forces. The cutter is divided into slices along its axis as shown in Figure 5.1. The cutting action of each slice is treated as an oblique cut, with each edge having an inclination angle equal to the helix angle of the cutter [76].

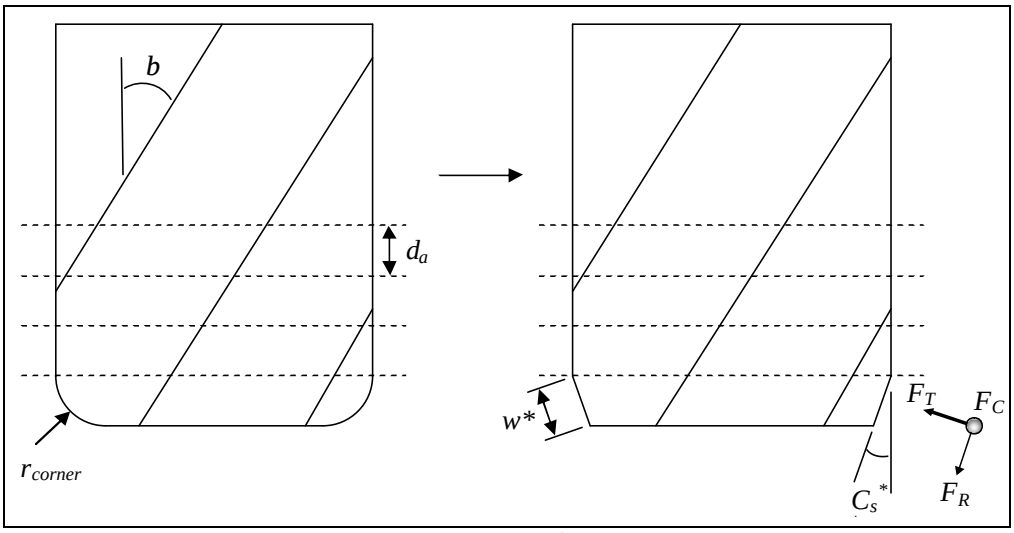

Figure 5.1 Axial slicing of helical end mill

For oblique cutting, an additional force component F_R exists due to the inclination angle i (Figure 5.2). In order to predict F_R, the inclination angle, chip flow angle h_c, and rake angle a_n need to be known. From Stabler's flow rule [77], the chip flow angle is equal to the inclination angle as shown in Equation (5.1).

$$h_c = i \tag{5.1}$$

If F_C is the total force in the cut direction and F_T is the total force in the thrust direction, then the expression for the resultant force F_R is

$$F_R = \frac{F_C\left(\sin i - \cos i \sin a_n \tan h_c\right) - F_T \cos a_n \tan h_c}{\sin i \sin a_n \tan h_c + \cos i}. \tag{5.2}$$

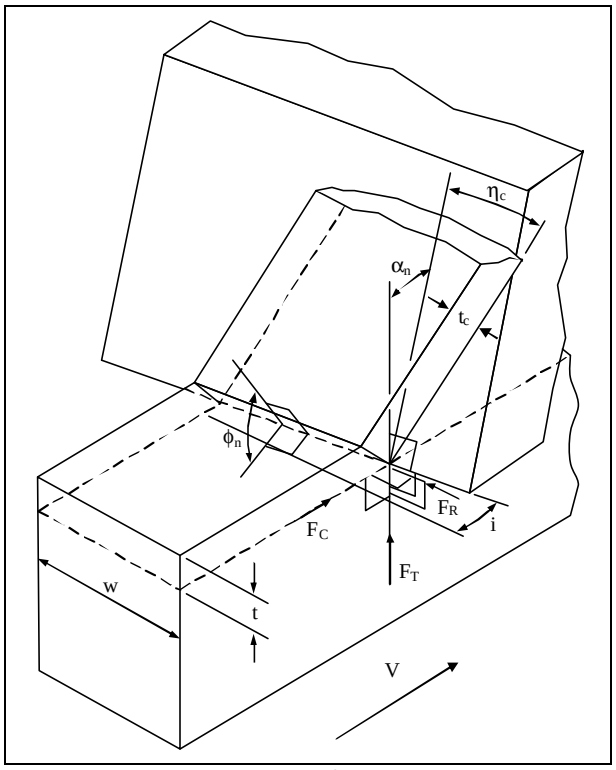

Figure 5.2 Oblique chip formation model [41]

The corner radius r_{corner} presents additional challenges with respect to cutting force predictions. The cutting force model described in Chapter 3 is for orthogonal or oblique cuts. In order to utilize the cutting force models, the effect of the corner radius being engaged during the cut must also be modeled. The use of an equivalent straight cutting edge to capture the effect on the corner radius has been used by previous researchers [78-80]. The transformation method described in [41], which is a compilation of the previous research, is used in the present modeling effort to capture the effect of the corner radius on cutting forces. Details of the transformation are presented below.

The chip flow angle due to the effect of the nose radius is computed based on geometric considerations and experimental observations. Elemental frictional forces are integrated along the cutting edge to find the resultant frictional force. The direction of

the resultant force is assumed to be the direction of chip flow. A schematic of a tool tip with a nose radius larger than the depth of cut is shown in Figure 5.3.

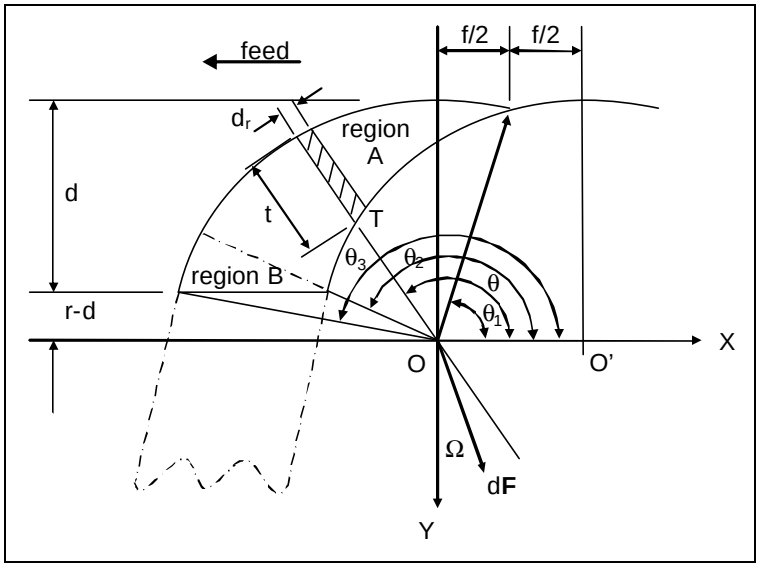

Figure 5.3 Geometry of chip flow model for nose radius tools proposed by Young et al. [41]

The direction of the elemental friction forces is given by

$$\overline{\Omega} = \tan^{-1}\left(\frac{NUM}{DEN}\right) \tag{5.3}$$

where

$$NUM = \left[-r\sin q\right]_{q_1}^{q_3} + \frac{1}{2}\left[\sin q\left(r^2 - f^2\sin^2 q\right)^{1/2} + \frac{r^2}{f}\sin^{-1}\left(\frac{f}{r}\sin q\right)\right]_{q_1}^{q_2} + f\left[\frac{\sin(2q)}{4} + \frac{q}{2}\right]_{q_1}^{q_2} + \left[(r-d)\ln(\sin q)\right]_{q_2}^{q_3} \tag{5.4}$$

and

$$DEN = \left[-r\cos q\right]_{q_1}^{q_3} + \frac{1}{2}\left[\cos q\left(r^2 - f^2\sin^2 q\right)^{1/2} + \frac{r^2 - f^2}{f}\ln\left\{\left(f\cos q\right) + \left(r^2 - f^2\sin^2 q\right)^{1/2}\right\}\right]_{q_1}^{q_2} + \frac{f}{4}\left[\cos(2q)\right]_{q_1}^{q_2} + \left[-(r-d)q\right]_{q_2}^{q_3} \tag{5.5}$$

The limits of integration are given by Equation (5.6).

$$\begin{aligned} q_1 &= \cos^{-1}\left(\frac{f}{2r}\right) \\ q_2 &= p - \tan^{-1}\left[\frac{r-d}{\sqrt{2rd-d^2}-f}\right] \\ q_3 &= p - \sin^{-1}\left(\frac{r-d}{r}\right) \end{aligned} \tag{5.6}$$

The predicted chip flow direction is then given by

$$h_0 = \frac{p}{2} - C_s - \overline{\Omega}. \tag{5.7}$$

Finally, the equivalent side cutting edge angle is given by Equation (5.8)

$$C_s^* = C_s + h_0. \tag{5.8}$$

The equivalent inclination angle i^*, equivalent rake angle a_n^*, and the equivalent chip flow direction h_c^* are shown in Equation (5.9).

$$\begin{aligned} i^* &= \operatorname{asin}\left(\cos(h_c)\sin(i) - \sin(h_c)\sin(a_n)\cos(i)\right) \\ a_n^* &= \operatorname{asin}\left[\frac{\sec(h_c)\sin(i) - \sin(i^*)}{\tan(h_c)\cos(i^*)}\right] \\ h_c^* &= i^* \end{aligned} \tag{5.9}$$

For a chip load h_{chip} and axial depth of cut d_a, the equivalent depth of cut t^* and width of cut w^* used for computing cutting forces are given by Equations (5.10) and (5.11)

$$t^* = h_{chip}\cos(C_S^*) \tag{5.10}$$

$$w^* = \frac{d_a}{\cos(C_S^*)} \tag{5.11}$$

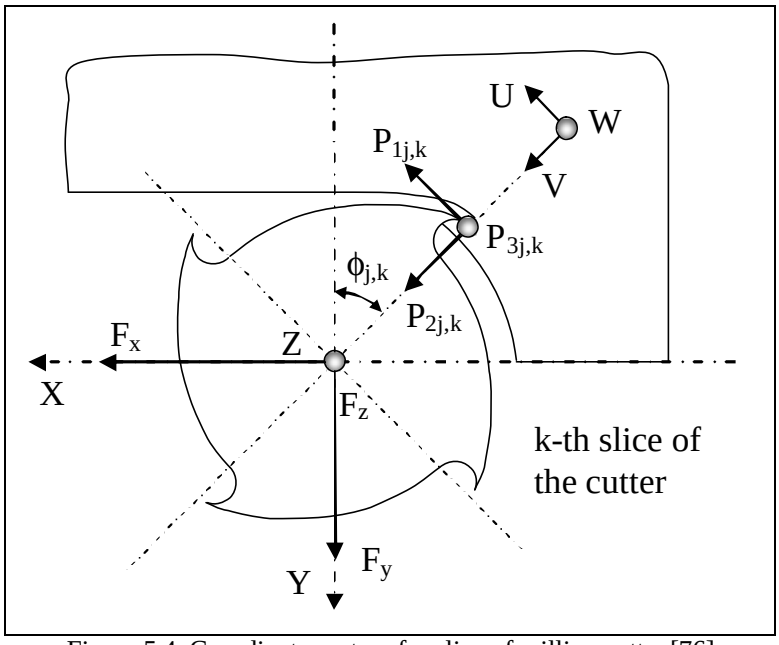

Figure 5.4 Coordinate system for slice of milling cutter [76]

The equivalent cutting conditions are used to predict the cutting forces F_C, F_T, and F_R. Those forces are then transformed to represent forces in the cutting, feed, and radial directions P_1, P_2, and P_3, respectively shown in Figure 5.4. The transformation is given by Equation (5.12).

$$\begin{aligned} P_1 &= F_C \\ P_2 &= -F_T \cos\left(C_S^*\right) - F_R \sin\left(C_S^*\right) \\ P_3 &= F_T \sin\left(C_S^*\right) - F_R \cos\left(C_S^*\right) \end{aligned} \tag{5.12}$$

After the forces are predicted for each slice, an additional transformation is performed to represent the cutting forces in the workpiece coordinate system. The force contribution from each slice is then summed produce the total milling force as a function of the cutter rotational position. The total forces (Equation (5.13)) from the combination of elemental slices correspond to the forces measured by the dynamometer.

$$F_X(f) = \sum_{j=1}^{r}\sum_{k=1}^{N_t} P_{1j,k}\cos\left(f_{j,k}\right) - P_{2j,k}\sin\left(f_{j,k}\right)$$
$$F_Y(f) = \sum_{j=1}^{r}\sum_{k=1}^{N_t} P_{1j,k}\sin\left(f_{j,k}\right) + P_{2j,k}\cos\left(f_{j,k}\right) \quad (5.13)$$
$$F_Z(f) = \sum_{j=1}^{r}\sum_{k=1}^{N_t} P_{3j,k}$$

In the Equation (5.13), r is the number of axial slices in the cutter and N_t is the number of flutes. The immersion angle $f_{j,k}$ of each tooth depends on the helix angle b and the height of the slice along the axis of the cutter. The expression for the immersion angle for each slice of each tooth is given by Equation (5.14).

$$f_{j,k} = f - (k-1)f_{pitch} - \frac{2\tan(b)}{D_{cutter}}z(j) \quad (5.14)$$

In the above equation, f is the rotational position of the cutter, D_{cutter} is the diameter of the cutter, and *z(j)* is the height of the cutter slice in the axial direction. f_{pitch} is the cutter pitch given by Equation (5.15).

$$f_{pitch} = \frac{2p}{N_t} \quad (5.15)$$

If the axial depth of cut is larger than the corner radius, the first slice of the cutter is considered to include the entire corner radius. The rest of the cutter that is engaged in cutting is divided into axial steps. The number of axial steps chosen depends on the cutting conditions.

Because milling is an intermittent cutting process, one additional aspect of modeling milling forces is establishing whether or not the flute is engaged in cutting. In milling, there are two main methods of feeding the cutter into the workpiece. The first is called conventional milling or up milling [81]. In up milling, the maximum chip

thickness occurs at the end of the cut. This is the most prevalent method of milling. The second method of milling is called climb milling or down milling. For down milling, the maximum chip thickness occurs at the beginning of the cut. The angular region in which the cutter is engaged in cutting is known as the immersion angle [82].

An illustration of the immersion angle for up milling is shown in Figure 5.5. For up milling with a cutter of diameter D and radial depth of cut d_r, the angle at which the flute begins to cut, f_{entry}, is 0°. The point at which the flute exits the workpiece is designated by f_{exit} and given by Equation (5.16).

$$f_{exit} = \arccos\left(\frac{D-2d_r}{D}\right) \tag{5.16}$$

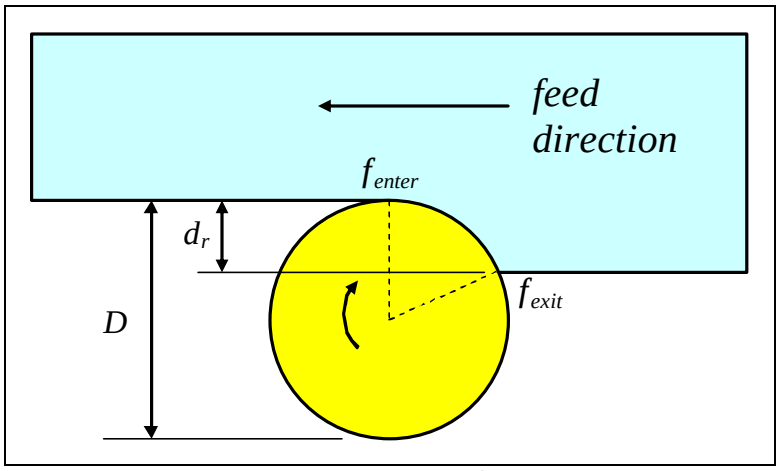

Figure 5.5 Immersion angles for up milling

An illustration of the immersion angle for down milling is shown in Figure 5.6. For down milling with a cutter of diameter D and radial depth of cut d_r, the expression for the angle at which the flute beings to cut is given by Equation (5.17). The exit angle f_{exit} is 0°.

$$f_{entry} = -\arccos\left(\frac{D-2d_r}{D}\right) \tag{5.17}$$

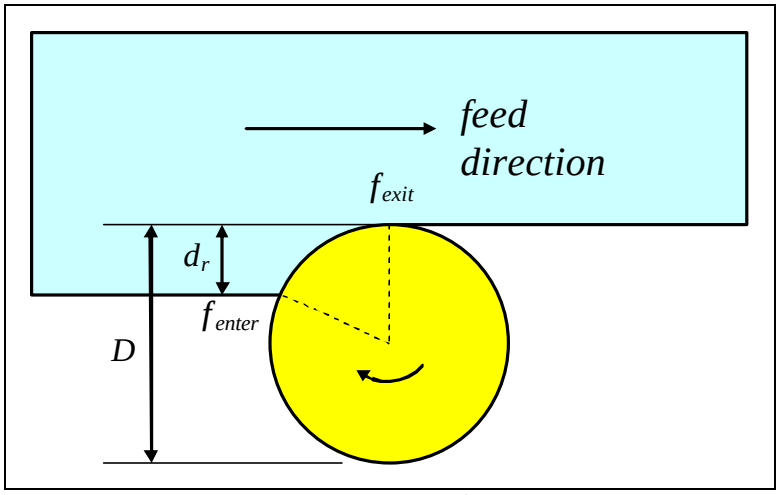

Figure 5.6 Immersion angles for down milling

Figure 5.7 illustrates the immersion angles for slot milling. In slot milling, the entry angle for the flute f_{entry}, is 0°. The flute is completely engaged in the cut until it reaches 180°.

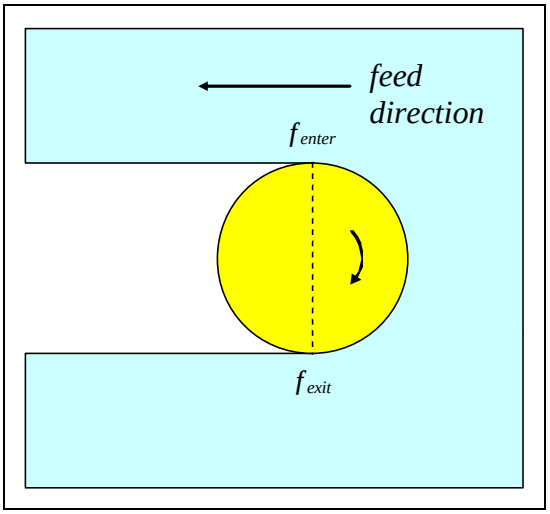

Figure 5.7 Immersion angles for slot milling

A summary of the entry and exit angles for the various milling operations is provided in Table 5.1.

Table 5.1 Summary of entry and exit angles for milling operations

Milling Type	Entry Angle	Exit Angle
Up Milling	0°	$\arccos\left(\frac{D-2d_r}{D}\right)$
Down Milling	$-\arccos\left(\frac{D-2d_r}{D}\right)$	0°
Slot Milling	0°	180°

5.3 Milling Experimental Details

The experimental data for milling was collected as part of the Metals Affordability Initiative (MAI) Machining Distortion program [83]. Cutting forces were measured using a Kistler Milling Dynamometer while milling Ti 6Al-4V (Figure 5.8.) Measurements of tool deflection and dimensional control were also performed. Specimens were generated in order to measure machining-induced residual stress for typical machining parameters. Care was taken to ensure that cutting force frequencies were low enough to be captured by the dynamometer. Consequently, force measurements were taken at lower spindle rotational speeds. These speeds were still within standard machining practices (0.25 to 0.51 surface m/s). Castrol 6519 ClearEdge lubricant was used during the machining. It is a water-based, water-soluble cutting fluid. It was applied in a flood manner through 6.4 mm diameter nozzles at low pressure.

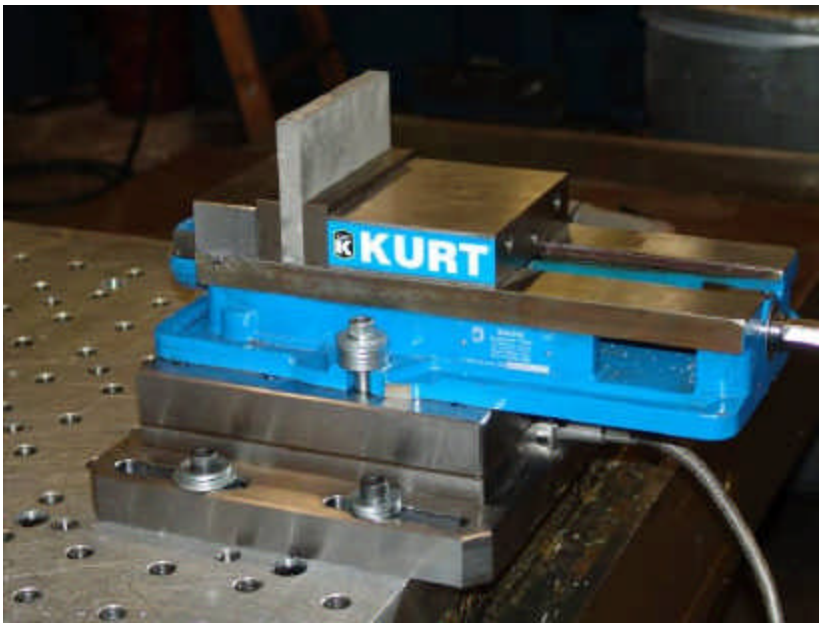

Figure 5.8 Dynamometer for cutting force measurements on Ti 6Al-4V

The orientation of force output from the dynamometer is shown in Figure 5.9. Forces measured to the right indicate a positive *X* force. Forces in the downward direction indicate a positive *Y* force. And forces into the paper indicate a positive *Z* force.

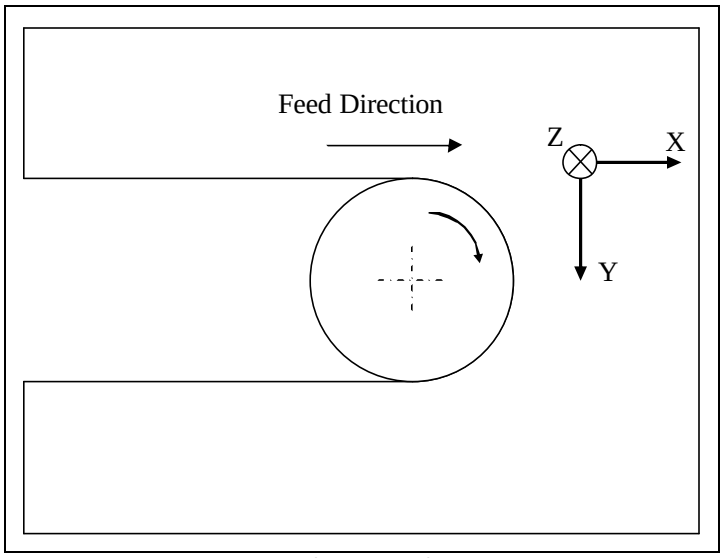

Figure 5.9 Force configuration for the dynamometer

Both finishing and full slot cuts are made for the experiments. The finishing cuts are modeled with the down milling configuration while the slot cuts are modeled with the full slot configuration. The orientation of the cutting directions is shown in Figure 5.10.

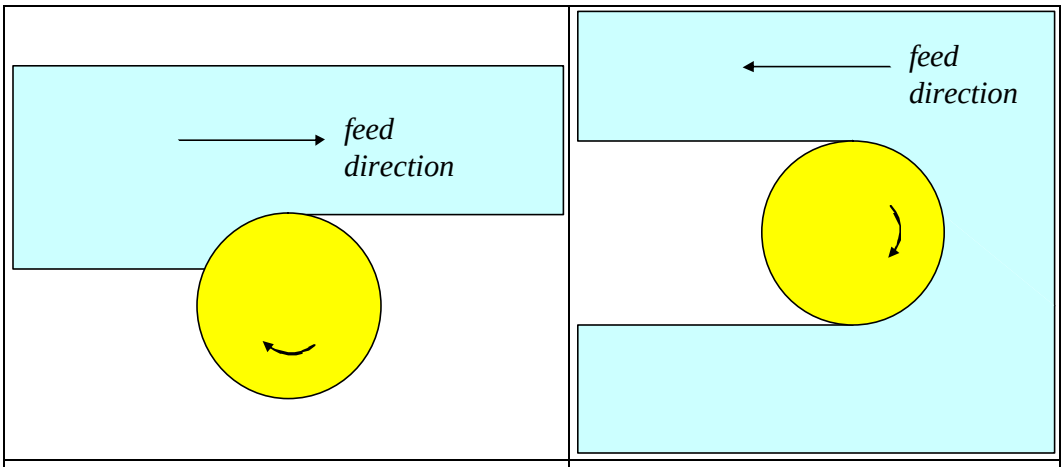

Figure 5.10 Cutting directions during force measurement

The experimental test conditions are shown in Table 5.2. Tungsten carbide and high speed steel cutters are used. Representative samples of the cutters are shown in Figure 5.11. Cases 1-4 are used to validate the cutting force model for milling. Residual stresses are measured for Cases 5-8. In Table 5.2, D is the cutter diameter and r is the corner radius of the cutter. For each of the conditions, the edge sharpness is assumed to be 7.0 μm.

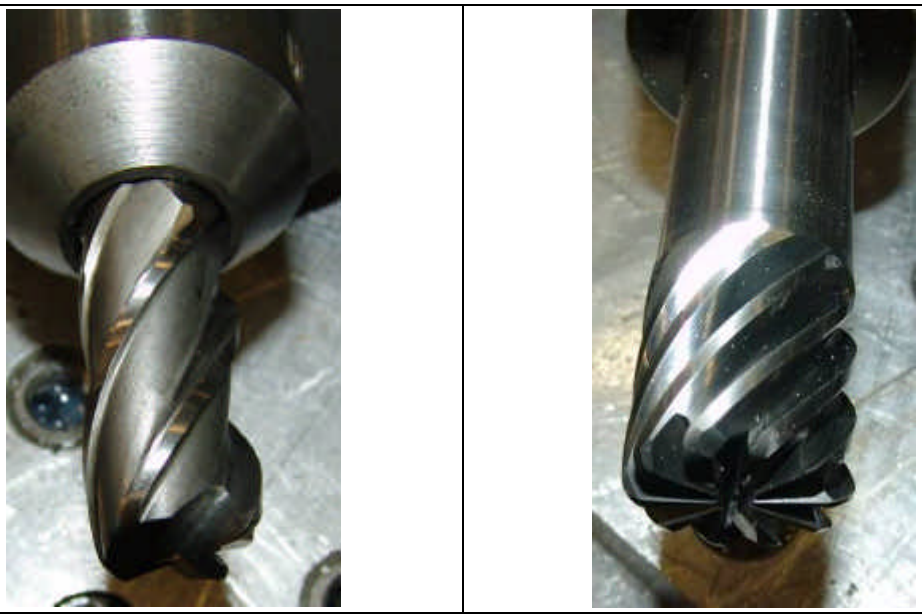
4-flute High Speed Steel (M42) End Mill | 10-flute Carbide End Mill

Figure 5.11 End mills used to generate specimens for residual stress measurement

Table 5.2 Milling experimental conditions

Case	Speed (rpm)	Type	Tool	Num of Flutes	Chip Load (mm/flute)	Axial DOC (mm)	Radial DOC (mm)	D (mm)	r (mm)
1	344	Down	W-C	4	0.080	8.89	0.89	19.05	3.05
2	344	Slot	W-C	4	0.080	0.89	--	19.05	3.05
3	509	Slot	W-C	6	0.080	0.25	--	25.40	3.05
4	509	Slot	W-C	6	0.080	2.03	--	25.40	3.05
5	1528	Down	W-C	10	0.080	20.32	0.89	25.40	3.05
6	1146	Down	W-C	10	0.080	0.76	17.78	25.40	3.05
7	191	Down	HSS	4	0.080	20.32	0.89	19.05	3.05
8	191	Down	HSS	4	0.080	0.760	17.78	19.05	3.05

Electro-polishing and X-ray diffraction measurements were performed on the four specimens at Proto Manufacturing. Measurements were made at 0.005 mm intervals up to 0.051 mm into the workpiece. Beyond 0.051 mm, measurements were made at 0.013 mm intervals until 0.127 mm. X-ray measurements in the remainder of the material were taken at 0.025 mm intervals. The conditions used for the measurements are shown in Table 5.3.

Table 5.3 X-ray diffraction measurement conditions

Parameter	Value	Parameter	Value
Target	0.154 nm	*Psi Tilts*	10
Target Power	200 W (30kv,6.7mA)	*Tilts*	(0, 20.00, 14.03, 7.42, 0.66)
Material	Ti 6Al-4V	*Collection Time*	2 sec. x 20 exposures
X-Ray Elastic Constant	84.116 GPa	*Total Collection Time*	5 min.
Crystallographic Plane	{213}	*Psi Zero Assignment*	Curve fit elliptical
Bragg Angle	142°		

The specimens were generated with the side and the end of the two end mills shown in Figure 5.11. For all machining tests, end mills were new with sharp cutting edges. The surface generated with the side of the end mill is called the rib, and the surface generated with the corner radius is the called the web. Both of these regions are illustrated in Figure 5.12.

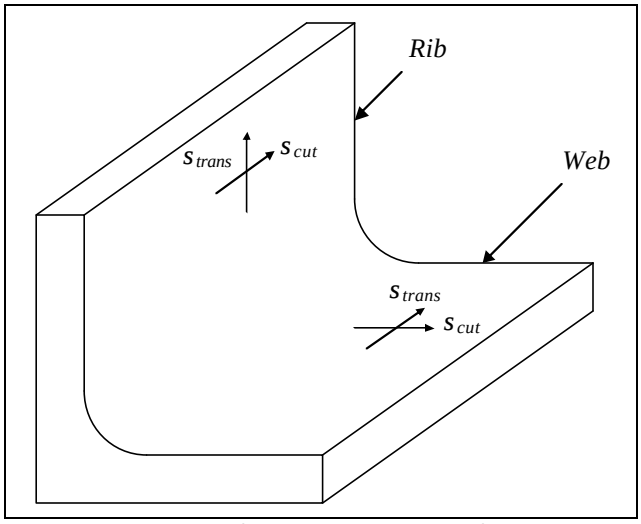

Figure 5.12 Orientation of stress measurements for milling samples

5.4 Milling Force Prediction Results

The results for the force predictions are shown below. *Fx*, *Fy*, and *Fz* represent forces in the feed, normal to the feed, and axial directions, respectively. Each of the plots captures the cutting forces for one revolution of the milling cutter. The average cutting forces for each revolution are shown in Table 5.4. All force predictions are made assuming the coefficient of friction due to the lubrication is $m = 0.4$ and the overall heat transfer coefficient $\bar{h} = 2000 \frac{W}{m^2 - ^\circ C}$. The cutting force data are presented relative to the maximum measured value of force for each cutting direction.

The cutting force predictions for Case 1 match the experimental data very well in terms of force magnitudes and shape. The conditions for Case 1 are representative of

those used in finishing cuts and rib cuts. The cutting conditions are such that the axial depth of cut is greater than the corner radius. Therefore, both the rounded portion of the cutter and straight segment of the cutter are engaged. Cutting on the corner radius causes a positive axial force. Cutting that occurs on the straight edge of the cutter causes a negative axial force due to the helix angle. The balance of forces in the axial direction changes from positive to negative throughout the rotation of the cutter. These effects are captured in Figure 5.15. The milling force model also captures the duration of engagement of each cutting tooth.

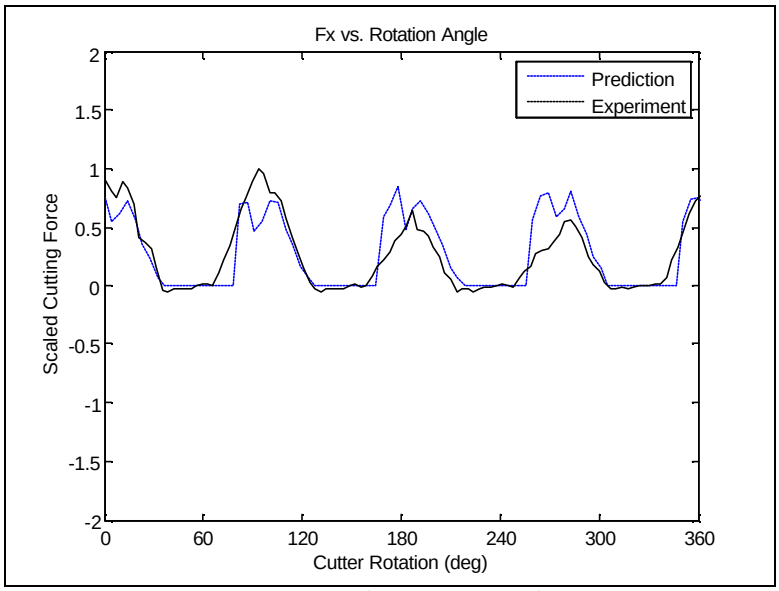

Figure 5.13 Milling force *Fx* results for Case 1

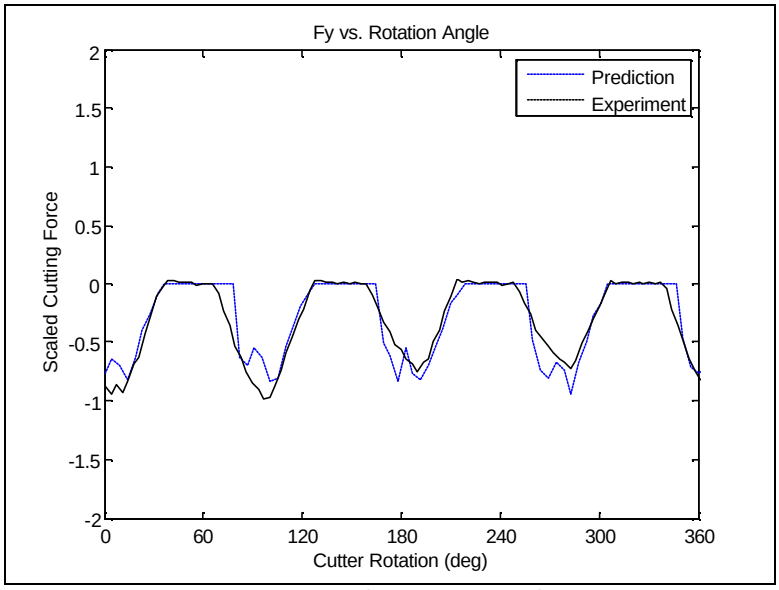

Figure 5.14 Milling force *Fy* results for Case 1

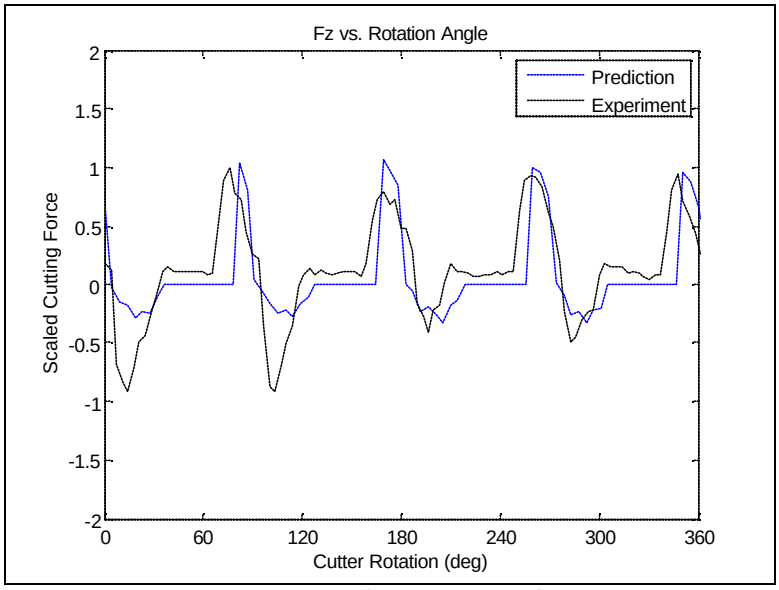

Figure 5.15 Milling force *Fz* results for Case 1

Case 2 is a slot milling operation with a moderate axial depth of cut. Only a portion of the corner radius is engaged for the cutting condition. As a result, the axial force is completely positive. Similar to Case 1, the engagement and disengagement of the flutes during the cutter rotation is captured very well by the predictive model. Forces in the feed direction *Fx* are shown in Figure 5.16. The relative predicted forces oscillate from around -0.5 to 0.0 as the flutes engage and disengage. The relative average force

per revolution is approximately -0.3. The measured forces oscillate from -1.0 to 0.2 with an average value of approximately -0.4. The results are similar for forces in the direction normal to feed *Fy*. The predicted forces oscillate between approximately -0.6 and -0.9 with the average force over the rotation -0.8. The measured forces range from -0.4 to -1.0 and have an average force of -0.7.

In both cases, the shape of the force profile during the cutter revolution is captured well by the predictive model even though the cutting force magnitudes differ from the experimental data. The discrepancy can be attributed in part to cutter runout. The runout can be seen in Figure 5.16 and Figure 5.17 as variations in the force peaks during the cutter rotation.

Radial runout is due to the axis of rotation of the spindle and axis of rotation of the cutter being out of alignment. In practice, runout can be attributed to several sources including cutter axis offset, cutter axis tilt, errors in forming the cutter, variation in insert size, or pocket irregularities [84]. Because the size of the runout is comparable to the chip load during milling, it can be a source of considerable variation in cutting forces. In spite of the runout, the milling force model performs well at predicting forces in the feed and normal directions.

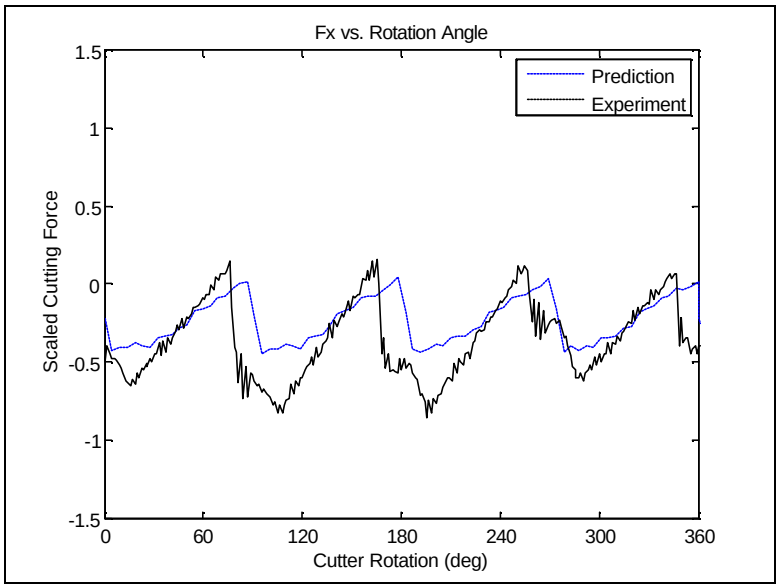

Figure 5.16 Milling force *Fx* results for Case 2

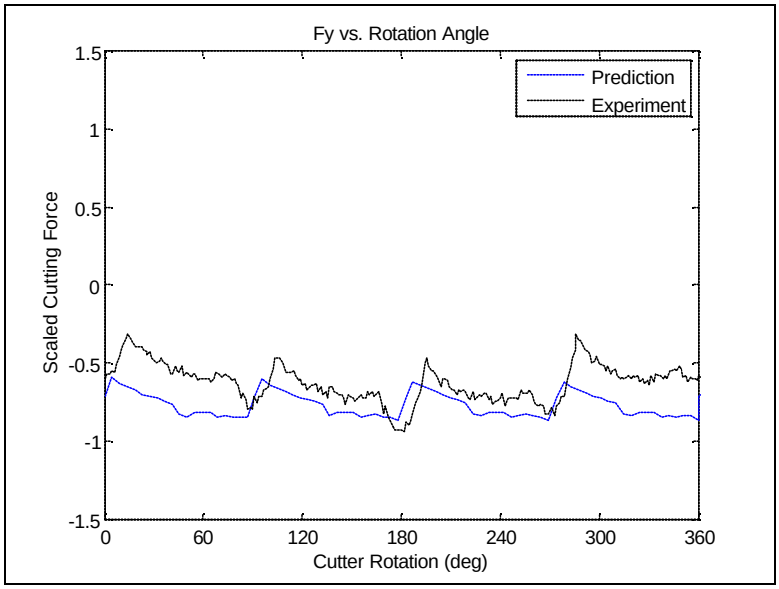

Figure 5.17 Milling force *Fy* results for Case 2

While the forces predicted in the feed and normal direction are very good for Case 2, there is a noticeable difference between predicted cutting forces and measured cutting forces is in the axial direction as shown in Figure 5.18. The experimental data show force peaks at approximately 90°, 180°, 270°, and 360°. However, the predictions show dips in the cutting forces at those positions. This discrepancy is of note due to the fact

that for other slot milling conditions, the cutting forces at similar positions show force valleys.

For a four-flute cutter in a slot milling operation, two flutes are engaged with the workpiece for a majority of the rotation. However, there is a point in the rotation where theoretically only one flute is engaged. That point in the rotation occurs when the flute engaged in cutting is at 90°. Since the axial forces from each of the flutes acts in the same direction, it would be expected that the minimum cutting force occurs when only one flute is cutting. This scenario is captured in the predictive cutting model where the minimum force values are at 90°, 180°, 270°, and 360°. However, in the experimental data, force valleys are found at those locations.

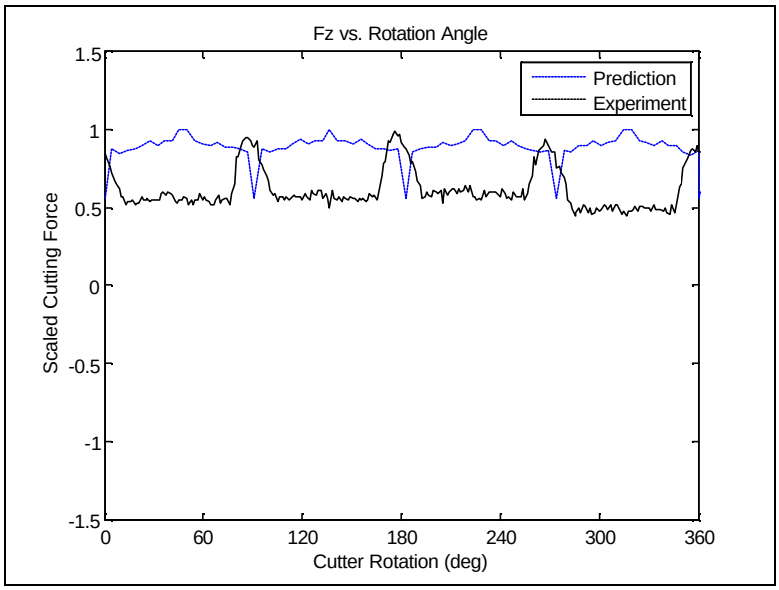

Figure 5.18 Milling force *Fz* results for Case 2

A second set of axial force measurements for the same conditions is utilized in an effort to understand the axial force results. The force data are plotted in Figure 5.19. It shows a broader peak for the measured axial forces, closer to what is expected for the cutting conditions. However, the force valley is not as sharp as predicted. The difference

between the two data sets shows that variability in measured cutting forces can be significant within the same set of cutting conditions.

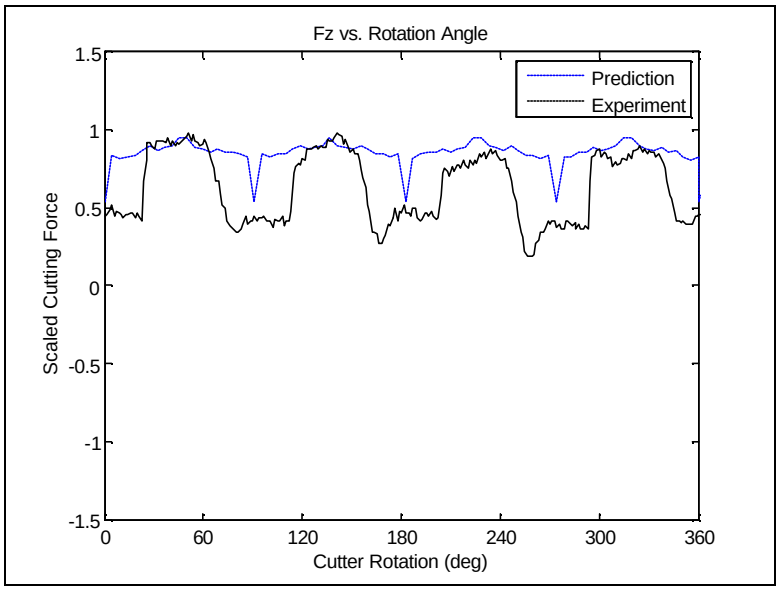

Figure 5.19 Additional milling force *Fz* results for Case 2

Case 3 is also a slot milling operation utilizing a 6-flute cutter. The axial depth of cut, like Case 2, is smaller than the corner radius. As a result, all of the cutting occurs on the corner radius. The force components in all three directions are well predicted. The shape of the predicted force profiles coincide almost exactly with the measured force profiles as shown in Figure 5.20 to Figure 5.22.

The experimental data show low frequency force oscillations throughout the cutter rotation. For instance, in Figure 5.20, the relative peak cutting feed cutting force at 60° is approximately 1.0. However, at 120°, the cutting force is slightly less than 0.7. For an ideal milling operation, the peak cutting forces at those locations should be the same. The variation in forces, similar to the previous case, indicates the presence of cutter runout. Even with the presence of runout, the model does a very good job of capturing the cutting forces as a function of cutter rotation.

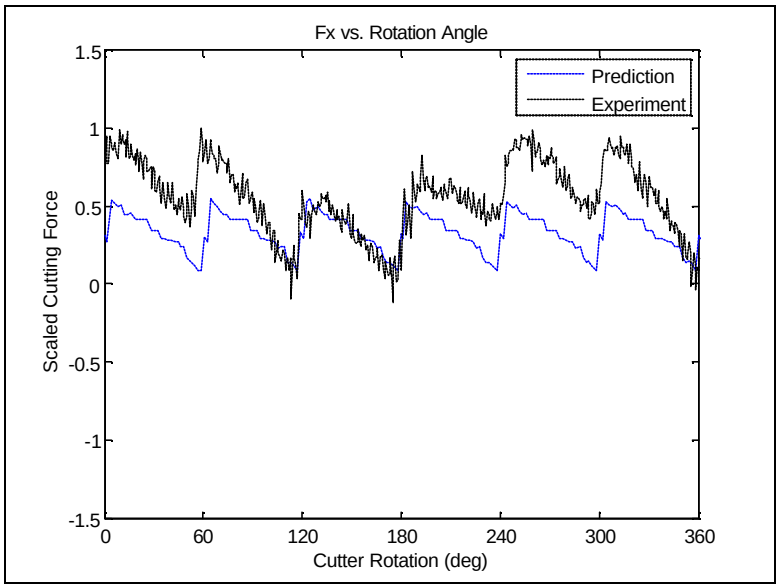

Figure 5.20 Milling force *Fx* results for Case 3

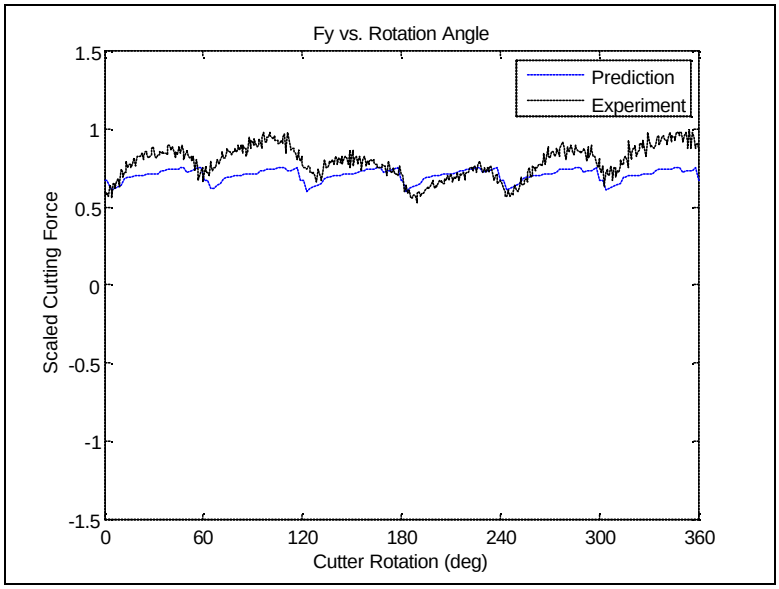

Figure 5.21 Milling force *Fy* results for Case 3

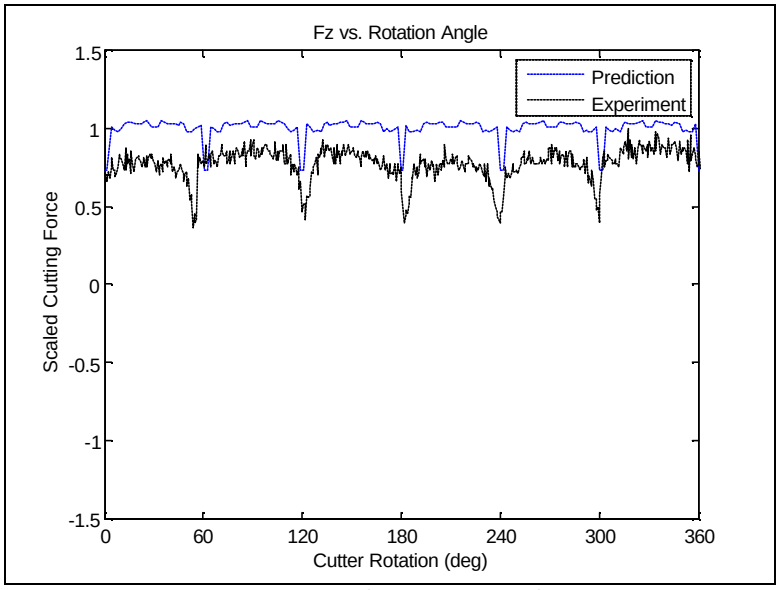

Figure 5.22 Milling force *Fz* results for Case 3

The results for Case 4 are shown in Figure 5.23 to Figure 5.25 . The conditions are similar to Case 3, except for a larger axial depth of cut. The larger axial depth of cut results in larger cutting forces in all directions. This trend is captured by the predictive model. Similar to Case 3, the presence of runout is visible in the experimental data. It induces a low frequency oscillation in the force data.

The difference between predicted and experimental forces can be attributed to the runout as well as the larger engagement of the corner radius during cutting. The side cutting angle C_S^* discussed in the milling force model may be over-predicted for the larger axial depth of cut used in Case 4. As a result, the predicted forces will be larger than expected, particularly in the axial direction.

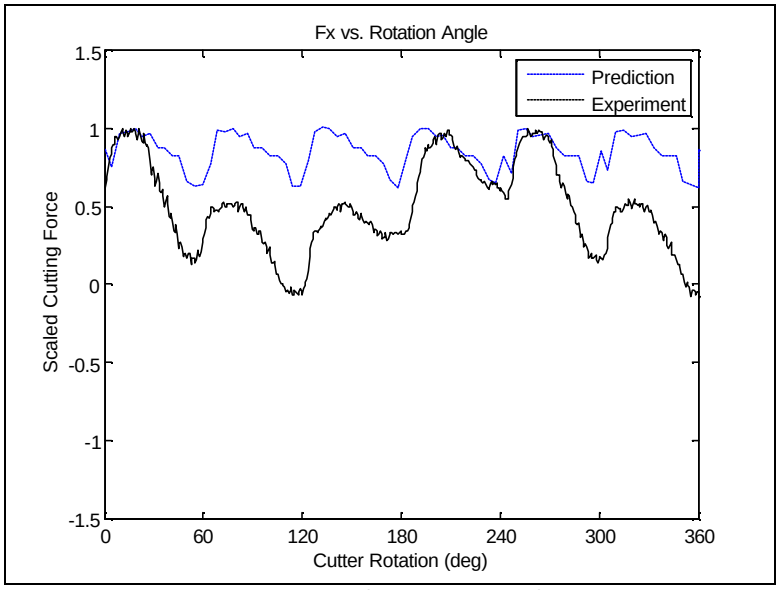

Figure 5.23 Milling force *Fx* results for Case 4

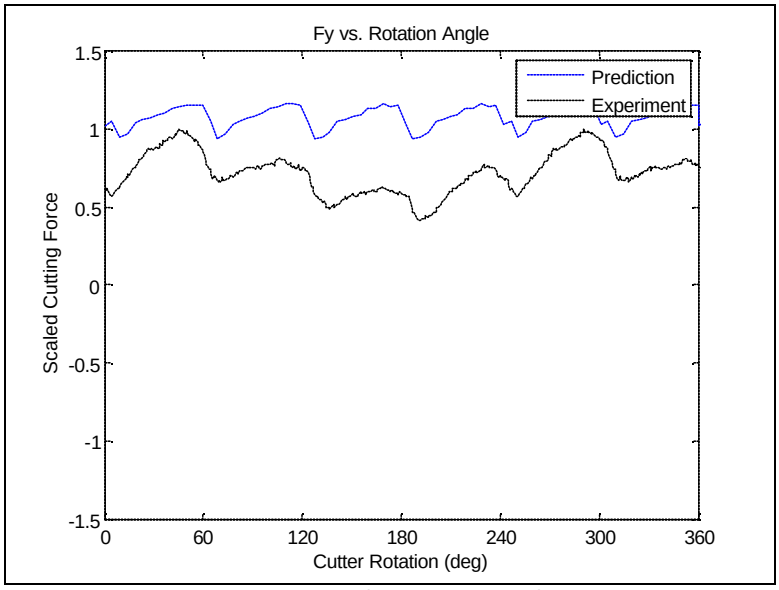

Figure 5.24 Milling force *Fy* results for Case 4

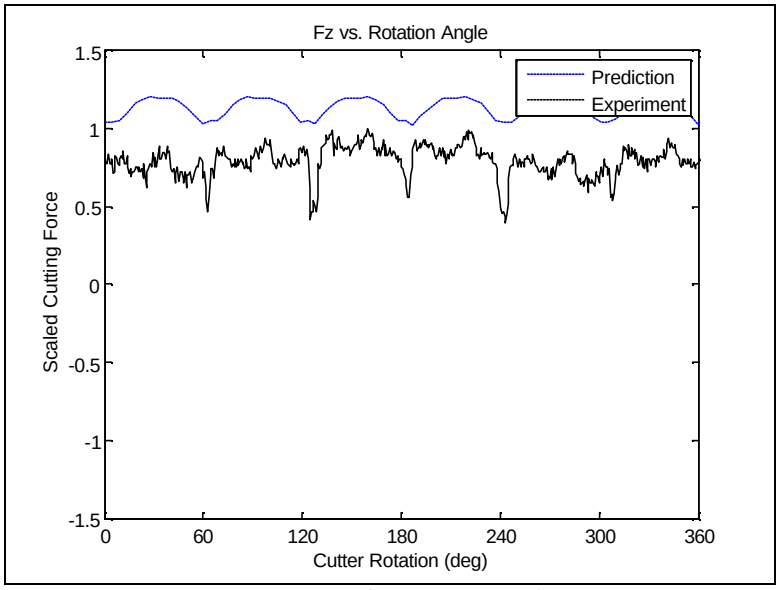

Figure 5.25 Milling force *Fz* results for Case 4

Table 5.4 summarizes the average cutting force results in Cases 1-4. The relative magnitudes of the average milling forces for a single rotation of the cutter are listed. For Cases 1-3, the majority of the average cutting forces are within 35% of the measured average values. The two forces that stand out however are the average axial force *Fz* Cases 1 and 2. Referring to Figure 5.15, the regions where the cutter is not engaged with the workpiece should produce zero cutting force. However, there is an approximately 0.1 relative force offset in the measured axial force. Consequently, the measured average force differs from the predicted average force by what appears to be a significant amount. However, if the 0.1 offset is removed, the computed average for the axial force becomes 0.03. The resulting error is 12%.

The larger prediction for the average axial force in Case 2 is due to the shape of the predicted cutting force. The predictions show a narrow force valley, while the measurement shows a wide force valley. The wider force valley causes the measured average axial force to be lower for a rotation of the cutter.

Table 5.4 Relative average milling forces for Cases 1-4

Case	Force Direction	Average Predicted	Average Measured	% Error
1	Fx	1.10	1.00	9.6%
	Fy	1.40	1.31	6.7%
	Fz	0.02	0.13	80.9%
2	Fx	0.66	1.00	34.3%
	Fy	3.15	2.59	21.8%
	Fz	2.51	1.76	42.3%
3	Fx	0.76	1.00	23.7%
	Fy	2.73	3.10	12.2%
	Fz	2.10	1.99	5.9%
4	Fx	1.69	1.00	68.7%
	Fy	4.30	2.73	57.4%
	Fz	1.01	0.71	41.9%

Average forces for Case 4, as Figure 5.23 to Figure 5.25 show, are higher than the measured average forces. This is due in part to the over-prediction of equivalent side cutting angle C_S^*. The larger axial depth of cut conditions used for Case 4 results in greater cutting forces in all directions.

5.5 Milling Temperature Modeling

The temperature modeling for milling differs from that used in Chapter 4 in the sense that lubrication is used. The coolant is modeled as being applied behind the tool tip as discussed in Section 3.2. The effect of the lubrication is a reduction in the workpiece temperature. Figure 5.26 provides a typical temperature profile under the tool tip without coolant while Figure 5.27 shows the temperature contour with coolant. The temperature difference at the surface for the cooled condition is approximately 130 °C.

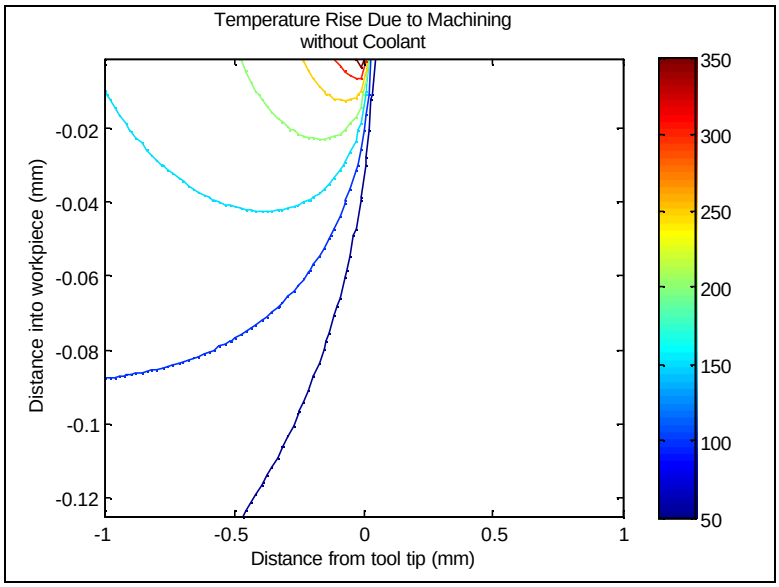

Figure 5.26 Temperature contours without coolant

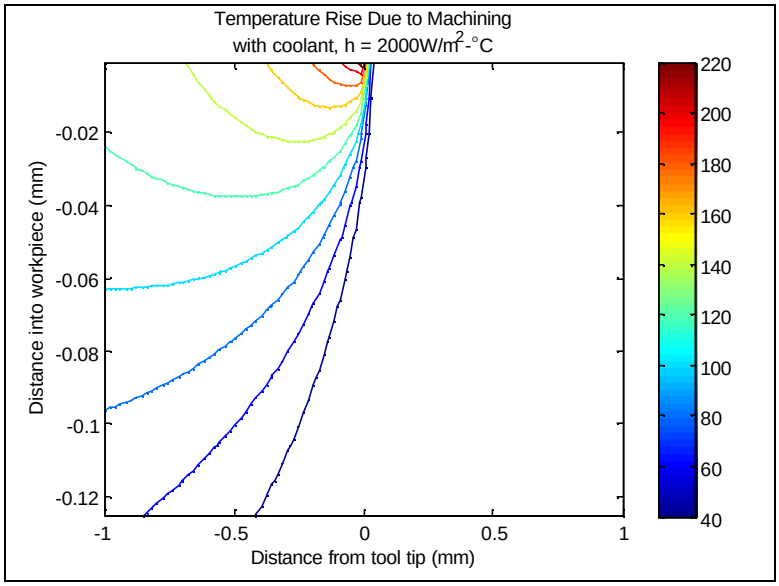

Figure 5.27 Temperature contours with coolant

Figure 5.28 compares the temperature difference between machining dry and with the coolant. As would be expected, the greatest temperature difference occurs at the surface. This is due to the greater temperature difference between the workpiece and the coolant at that location and the higher heat loss intensity.

An interesting feature of Figure 5.28 is the high temperature gradient. The predicted temperature drops by nearly 350 °C within 0.08 mm. This would indicate that

the effects of temperature on residual stress are more prominent near the workpiece surface. If residual stresses exist beyond that depth, they will be due to mechanical loading.

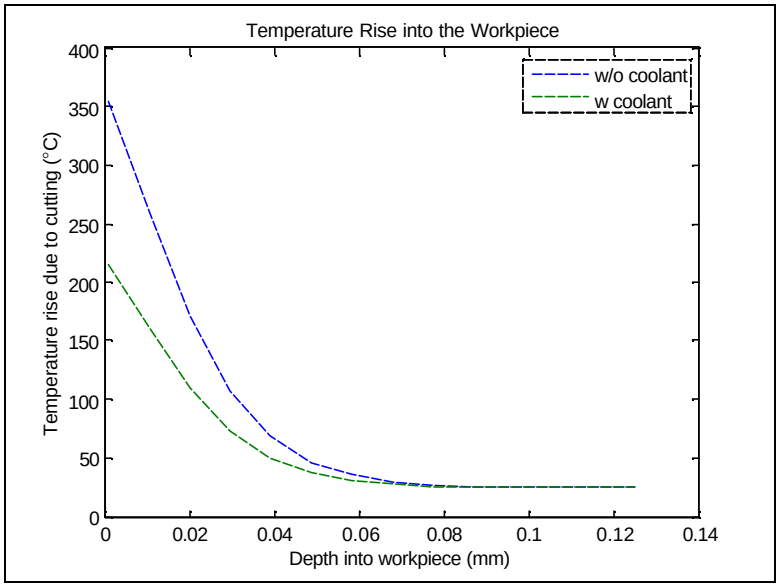

Figure 5.28. Temperature rise directly beneath the tool tip

5.6 Milling Residual Stress Results

Residual stress measurements are made on the ribs for Cases 5 and 7 and measurements are made on the webs for Cases 6 and 8. Force measurements are unavailable for the machining conditions used to generate the samples in Cases 5-8. The results from the residual stress measurements and the model predictions are shown below. The residual data are scaled relative to the maximum measured value in the cut direction for Case 5. The residual stresses were measured to a depth of 0.381 mm, although the values oscillated about zero beyond approximately 0.076 mm. Because of this, the residual stresses are treated as diminishing to zero beyond 0.076 mm. The data plotted below show the residual stresses between the surface and 0.076 mm below the surface. Error bars for each of the measured data points indicate the standard deviation

for the data point. The standard deviation information was provided by Proto as part of the measurement data.

The residual stress results for Case 5 are shown in Figure 5.29 and Figure 5.30. The data show low levels of compressive residual stress produced by the cutting process. The maximum compressive residual stress exists at the surface and has a relative value of approximately -1.0 in the cut direction and -0.8 in the transverse direction. The penetration of the residual stress produced from cutting is fairly shallow. Due to the oscillation, the exact depth of penetration is difficult to discern. However, judging by the overall trend, the residual stress due to machining appears negligible beyond 0.020 mm.

The predicted residual stresses are of greater magnitude than the measured residual stresses. One significant potential source of that error is the helical geometry of the milling cutter. Due to the helix angle of the cutter, the depth of cut at each rotational position of the cutter varies along the axis of the cutter. As a result, the cutting force varies along the axis of the cutter. Isolating the exact point of cut during the rotation in which the surface of the residual stress measurement is made is not a straight-forward proposition. In the current modeling procedure, the axial slice chosen to represent the cutting forces imparted on the newly generated surface is the one that has the largest depth of cut at the newly formed surface. This assumption could lead to an over-estimating the forces at the surface. However, each of the predictions for the residual stresses in the ribs is made in the same fashion to maintain consistency.

Another factor is the overlapping effect of subsequent flutes on the surface finish. The contact between the machined surface and the passing flutes may also impact the surface residual stresses. These effects are not considered in the present model.

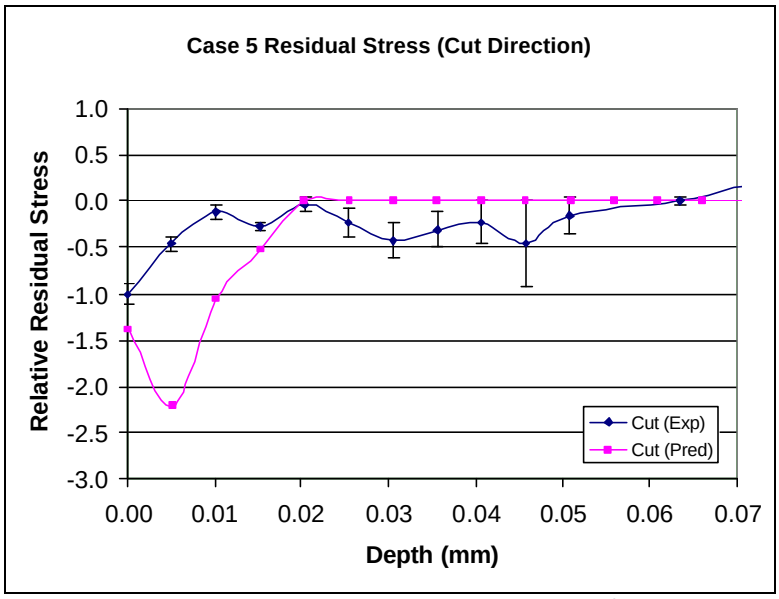

Figure 5.29 Residual stress results in cut direction for Case 5

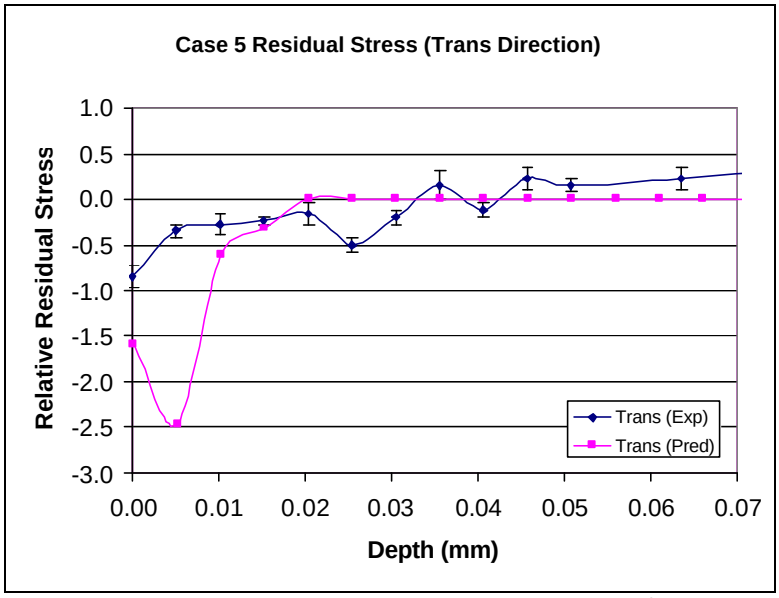

Figure 5.30 Residual stress results in transverse direction for Case 5

The results for Case 6 are shown in Figure 5.31 and Figure 5.32. The residual stresses for Case 6 are measured on the web of the machined part. Similar to Case 5, the depth of penetration of the residual stresses are reasonably well predicted. Residual stresses in the cut direction diminish to zero at approximately 0.015 mm. The same is true for the residual stress in the transverse direction. The predicted residual stresses

penetrate to approximately 0.025 mm. The residual stresses reach zero around 0.018 mm. The predictions in indicate the residual stresses should diminish at approximately 0.025 mm. In both directions, the residual stresses are slightly over-predicted with regards to magnitudes. The explanation provided for the low compressive residual stresses in Case 5 are also relevant to Case 6.

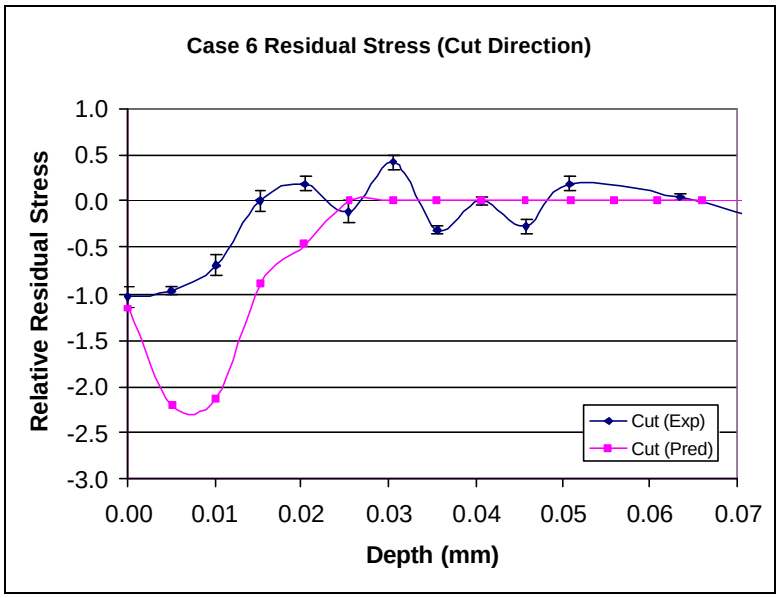

Figure 5.31 Residual stress results in cut direction for Case 6

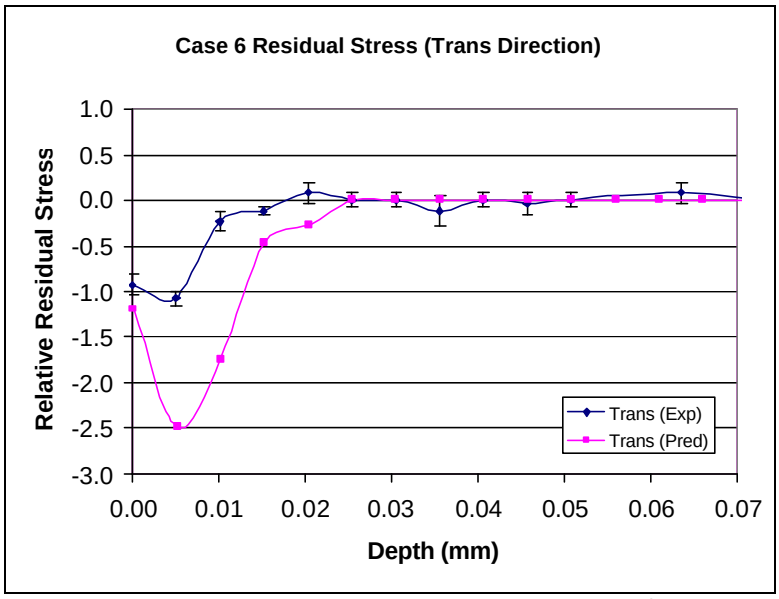

Figure 5.32 Residual stress results in transverse direction for Case 6

Case 7 uses cutting conditions similar to those used in Case 5 except for the type of cutter and the cutting speed. The results are shown in Figure 5.33 and Figure 5.34. The conditions used in Case 7 yield larger measured compressive residual stresses. For lower cutting speeds, the mechanical loads dominate the residual stress formation. When mechanical loads dominate, the residual stress formation is more compressive [2]. An additional characteristic of the residual stress results for Case 7 is the slightly larger depth of penetration.

Both of these traits can be explained from a modeling perspective. The larger depth of penetration of the residual stress is due to its dependence on mechanical loading. For Case 7, the predicted shear angle for the slice treated as producing the residual stress is approximately 20°. For Case 5, the shear angle is approximately 30°. The lower shear angle produces a larger mechanically stressed zone beneath the newly generated surface. Consequently, the residual stress formation in that region will be more compressive and penetrate deeper beneath the surface.

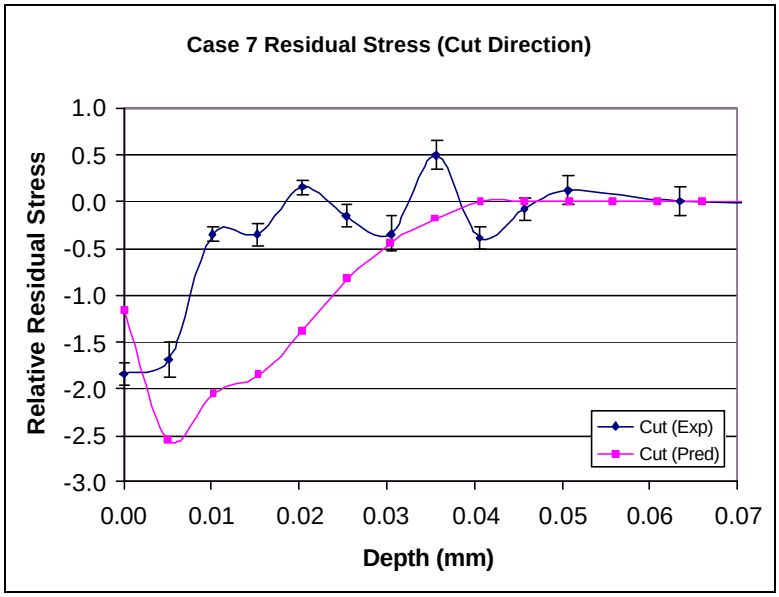

Figure 5.33 Residual stress results in cut direction for Case 7

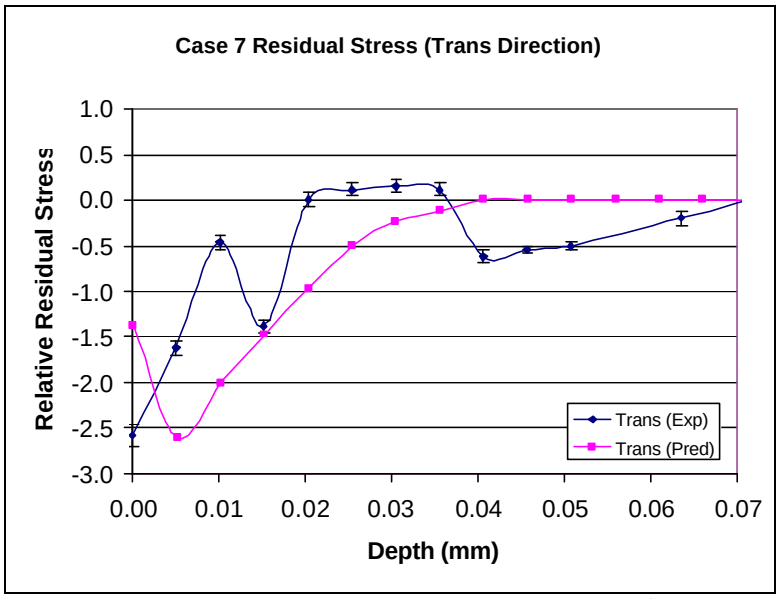

Figure 5.34 Residual stress results in transverse direction for Case 7

The residual stress results for Case 8 are shown in Figure 5.35 and Figure 5.36. Case 8, like Case 6, is a slot milling operation with the measured surface of interest being the web. A large radial depth of cut coupled with a shallow axial depth of cut results in a machined surface that is generated largely by the corner radius. The slow cutting speed results in the mechanical load exerting more dominance compared to the thermal load. Similar to the previous cases, the exact depth of penetration is difficult to isolate from the experimental data. However, the trend with regards to both the compressive nature of the residual stress as well as the depth to which it penetrates is captured by the predictive model.

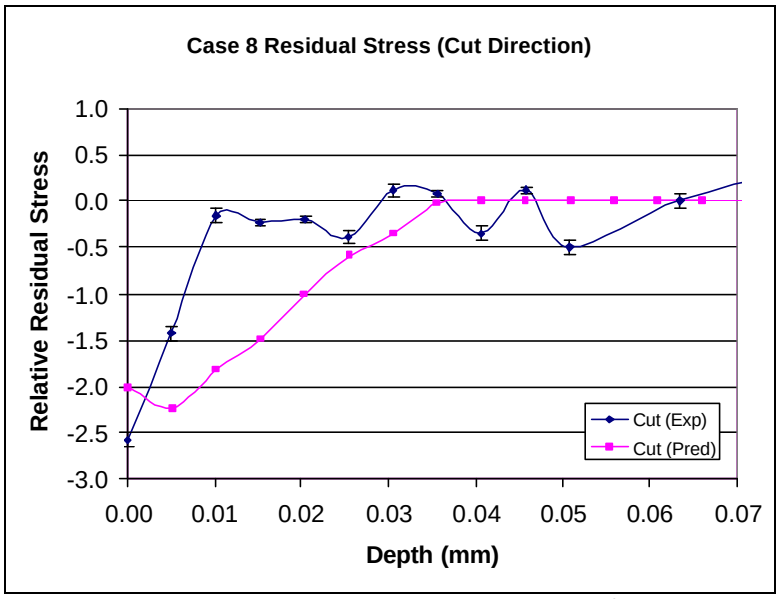

Figure 5.35 Residual stress results in cut direction for Case 8

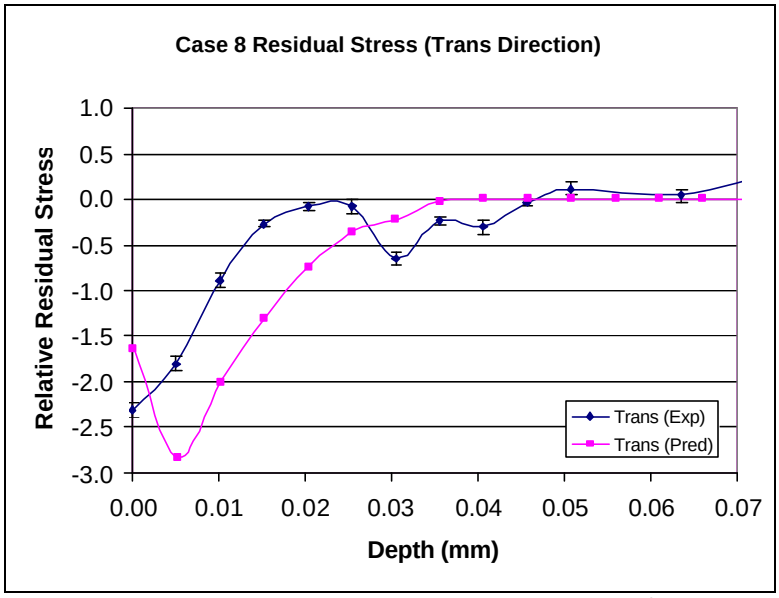

Figure 5.36 Residual stress results in transverse direction for Case 8

The comparisons between predicted residual stresses and measured residual stresses show that the predictive model performs well in terms of capturing the depth of penetration as well as the general residual stress profile for milling. In most cases, the predicted residual stress magnitudes are larger than the measured values. This discrepancy can be attributed to the variability in the precise location of the cutting edge

that generates the newly formed surface. In spite of this, the model consistently predicts the correct trends for the residual profiles for milling conditions.

5.7 Milling Sensitivity Analysis

A sensitivity analysis of model parameters on face milling has been performed. Five model inputs are used as independent variables. The variables are chosen to capture the effect of user input parameters on the behavior of the model. They are as follows:

- C – Johnson-Cook strain rate constant
- m – Johnson-Cook temperature constant
- ER – edge or hone radius of the cutting tool
- mu – coefficient of friction between tool and workpiece
- h – overall heat transfer coefficient.

The friction factor is treated as the friction between the tool and chip (Equation (3.14) in Chapter 3) and also as the friction factor between the tool and the workpiece (Equation (3.30) in Chapter 3). The levels for each factor are listed in Table 5.5.

Table 5.5 Milling residual stress input factor levels

Variable	Low	High
C	0.015	0.025
m	0.6	0.8
ER (mm)	0.005	0.051
mu	0.4	0.9
h (W/m^2-°C)	2000	5000

The output parameters of the model are listed below.

- Fx – average force in feed direction
- Fy – average force normal to feed direction
- Fz – average axial force
- Tmax – maximum surface temperature
- Acp – area of tensile residual stress in cut direction
- Acm – area of compressive residual stress in cut direction
- Atp – area of tensile residual stress in transverse direction
- Atm – area of compressive residual stress in cut direction
- Depth – depth of maximum compressive residual stress into workpiece

The model inputs for the milling sensitivity analysis are the similar to those used in the orthogonal cutting analysis. However, there are several differences in the model outputs. Instead of a single force value for cutting and thrust directions, the average force over a revolution of the cutter is used as the output. There is also an axial force output *Fz* which is the average force per revolution in the axial direction. Additionally, the effect of the heat transfer coefficient is also incorporated into the analysis because coolant is used in the milling process.

The friction coefficient *mu* has a pronounced effect on most of the outputs. Cutting forces increase in magnitude for higher values of *mu*. However, it has less influence on the average axial force *Fz*. This is because the axial force is more influenced by the cutter geometry in face milling because of the length of the tooth engagement in the axial direction. The average normal force *Fy* is more influenced by the edge radius because that variable directly influences the thrust force. The thrust force

plays a primary role in the predicted normal force due to the transformation from the tool edge coordinates to the global coordinates.

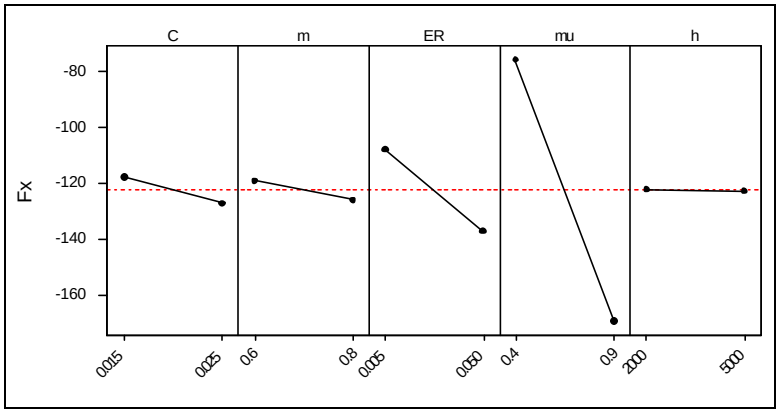

Figure 5.37 Main effects plot for *Fx* milling

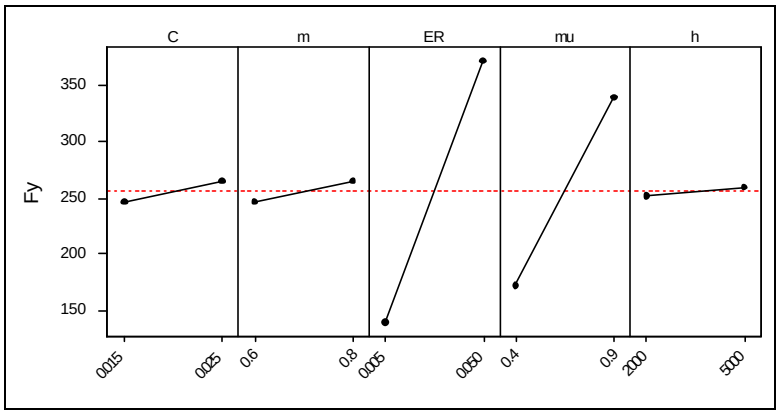

Figure 5.38 Main effects plot for *Fy* milling

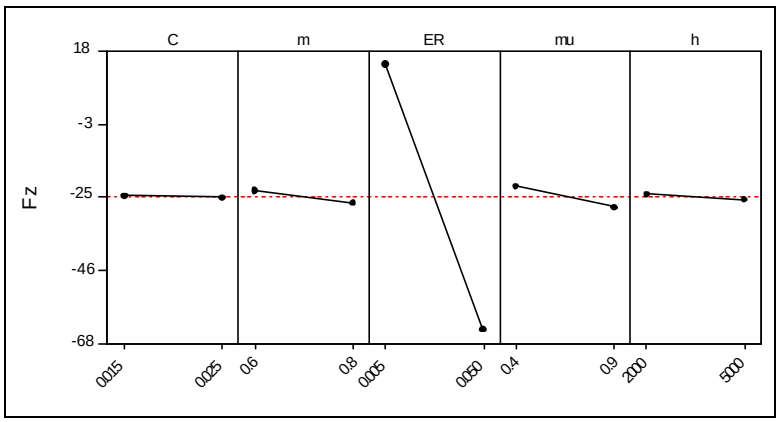

Figure 5.39 Main effects plot for *Fz* in milling

Table 5.6 Summary of effect of increasing input variables on *Fx, Fy, and Fz*

Input Variable	*Fx*	*Fy*	*Fz*
C	minimal increase	minimal increase	n/c
m	minimal increase	minimal increase	n/c
ER	increase	increase	increase
mu	increase	increase	minimal increase
h	n/c	n/c	n/c
Comment	▪ Increasing the friction coefficient increases average cutting forces ▪ Friction has less influence on in axial direction because tool geometry dominates forces ▪ Increasing edge radius increases cutting forces due to increase in plowing effect ▪ The heat transfer coefficient has minimal impact on cutting forces		

The cutting temperature is largely affected by the hone radius and the friction coefficient. This is due to the higher cutting forces generated when the hone radius is large or the friction coefficient is high. The material constants *C* and *m* have a small impact due to their influence on cutting forces. The heat transfer coefficient, as modeled in the current application, has a negligible impact on the cutting temperature. The effects are summarized in Table 5.7.

The depth of maximum compressive residual stress is impacted by the friction coefficient *mu* and hone radius *ER*. This result is consistent with the fact that the depth of penetration of residual stress depends on the tool geometry as well as the cutting forces. Those two parameters have a strong influence in defining the loading history experienced by the workpiece. The effects are summarized in Table 5.7.

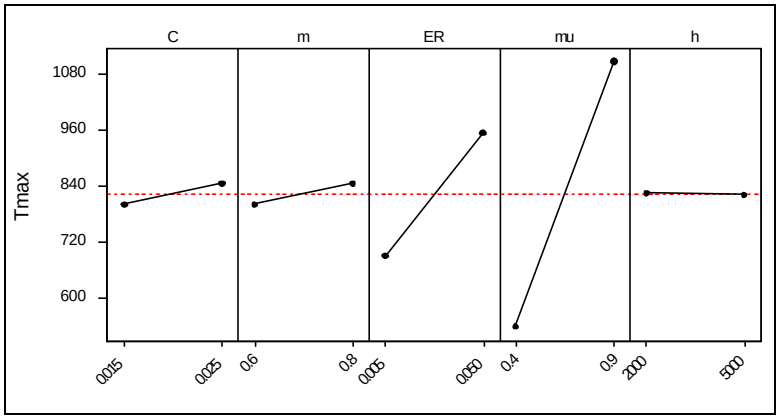

Figure 5.40 Main effects plot for T_{max} milling

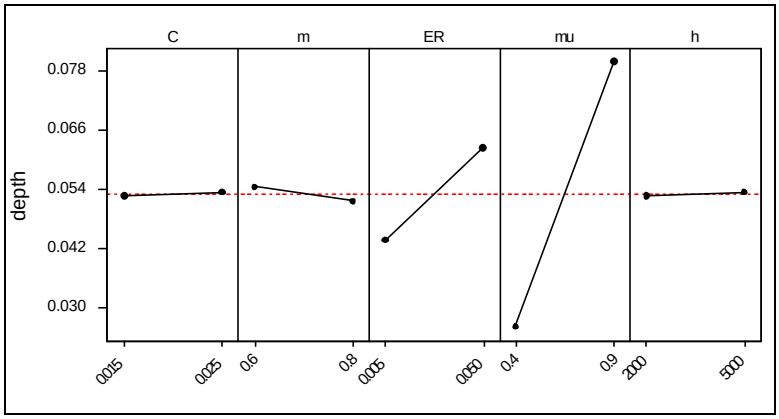

Figure 5.41 Main effects plot for *Depth* in milling

Table 5.7 Summary of effect of increasing input variables on *Tmax and Depth*

Input Variable	*Tmax*	*Depth*
C	minimal increase	n/c
m	minimal increase	n/c
ER	increase	Increase
mu	increase	Increase
h	minimal decrease	n/c
Comment	▪ Increase in edge radius increases plowing forces and resulting temperatures ▪ Same can be said for increasing friction coefficient ▪ Other variables have negligible effect	▪ Friction coefficient affects boundary stresses which shape the residual stress profile ▪ Edge radius also influences boundary stresses which shape the residual stress profile

The residual stress areas are influenced by most of the variables. These results show a similar trend to the results from the broaching analysis. The Johnson-Cook variables *C* and *m* play a role because they affect how the material behaves under thermo-mechanical loading. The other parameters control what the thermo-mechanical load will be. These influences captured in the main effects plots shown in Figure 5.42 to Figure 5.45 and the effects summarized in Table 5.8.

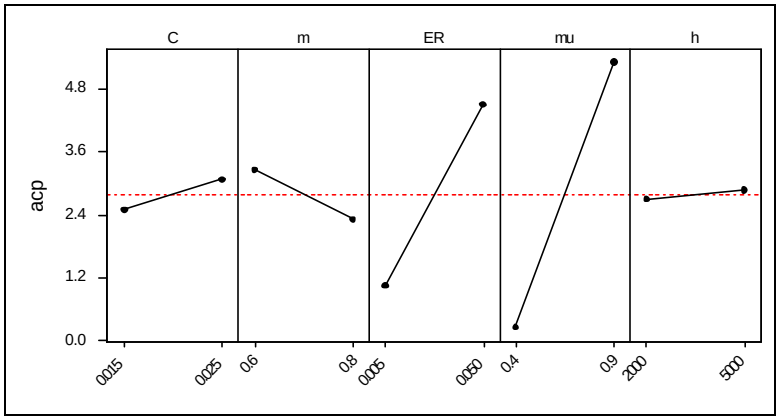

Figure 5.42 Main effects plot of area of tensile residual stress in cut direction (*ACP*)

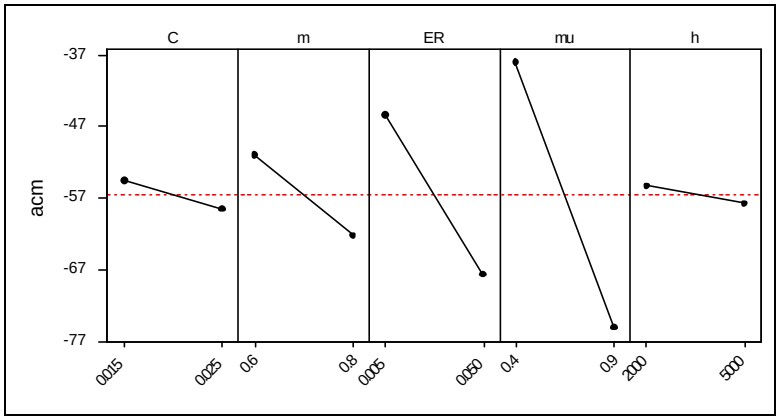

Figure 5.43 Main effects plot of area of compressive residual stress in cut direction (*ACM*)

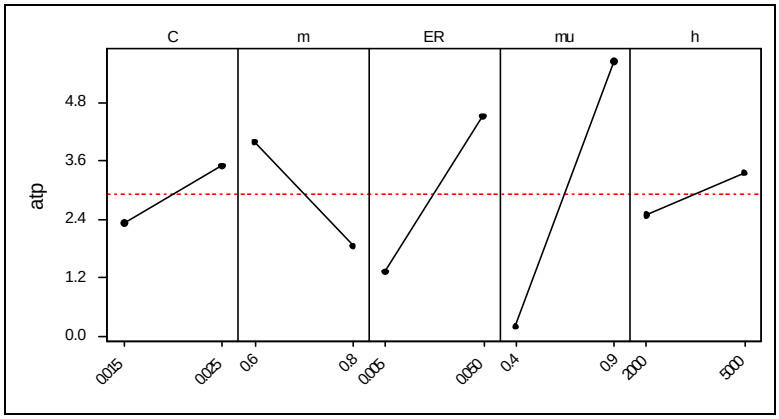

Figure 5.44 Main effects plot of area of tensile residual stress in transverse direction (*ATP*)

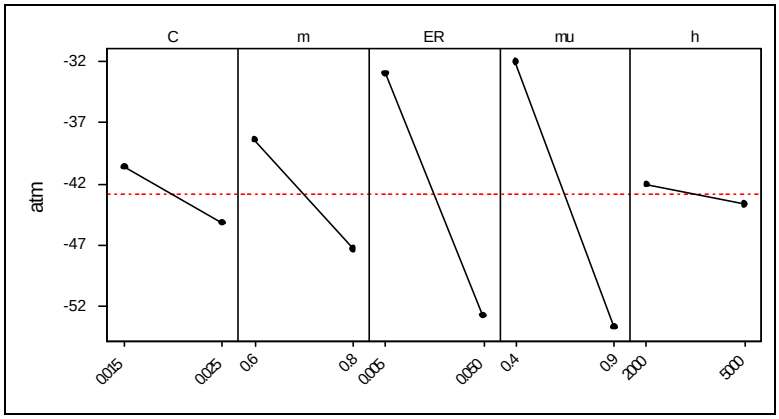

Figure 5.45 Main effects plot of area of compressive residual stress in transverse direction (*ACM*)

Table 5.8 Effect of increasing input variables on *atp, atm, acp, and acm*

Input Variable	*acp*	*acm*	*atp*	*atm*
C	increase	increase	increase	increase
m	decrease	increase	decrease	increase
ER	increase	increase	increase	increase
mu	increase	increase	increase	increase
h	minimal increase	minimal increase	increase	minimal increase
Comment	▪ The residual stress areas are influenced by most variables with heat transfer being the least influential ▪ Results show a similar trend to the results from the broaching analysis. ▪ Increase in *C* indicates residual stress area is sensitive to strain rate. ▪ Increase in *m* indicates residual stress area is sensitive to thermal behavior of material ▪ Increase in edge radius increases stresses due to higher plowing forces. Results in higher overall stresses ▪ Increase in friction increases stresses due to higher cutting forces. Higher overall stresses in workpiece			

5.8 Summary

In this chapter, a model for predicting residual stress for milling operations is presented. The model is derived from the model for orthogonal cutting developed in Chapter 3. Geometric transformations as well as location effects are considered. Additionally, the effect of cutting fluid is incorporated into the model. Milling experiments are performed on Ti 6Al-4V to measure cutting forces as well as residual stresses produced from milling. Both slot milling and face milling are considered in the modeling predictions.

The milling force predictions show good agreement with the experimental data. The predicted force profiles match the experimental data in terms of force magnitudes and profiles. It is found that the corner radius and the modeling of the corner radius play an important role force predicted for the axial direction. For depths of cut smaller than the corner radius, there is a pronounced effect on the force predictions.

Residual stresses are measured for four experimental cases. Two measurements are taken on the rib of the machined samples, and two are take on the web of the machined samples. The residual stress results for Cases 5 and 6 showed low levels of compressive residual stress generated from the cutting operation. Cases 7 and 8 produced larger magnitudes of compressive residual stress due in part to slower cutting speeds. The model predictions capture the residual stress trends well. The depth of penetration of residual stress and the compressive nature of the residual stress are captured. However, predictions for the residual stress magnitudes tend to be larger than those measured.

A sensitivity analysis is performed to determine the impact of user inputs on the model. The results show that for the range of values explored, the friction coefficient has a strong influence on all of the model outputs. In addition to the friction coefficient, the edge radius of the cutter also has an impact on the model predictions. Nearly all of the input parameters are found to affect the residual stress predictions. This is due to the dependency of the residual stress model on a variety of inputs that affect the loading stresses as well as the behavior of the material under thermo-mechanical loading.

CHAPTER 6

MODELING RESIDUAL STRESSES IN HARD TURNING

6.1 Introduction

In the previous chapters, modeling techniques for predicting residual stresses for orthogonal cutting and milling were discussed. In this chapter, a model for predicting residual stresses produced from hard turning is presented. The modeling techniques are similar to those used in the previous chapter. Cutting forces consisting of both chip formation forces and plowing forces are modeled. Additionally, the temperature rise in the workpiece is modeled. And finally, the thermo-mechanical residual stress model is employed. The model predictions are compared with experimental results.

6.2 Cutting Force Modeling in Turning

Similar to the treatment of the corner radius in milling, an equivalent cutting edge is used to capture the influence of turning with a round-nosed tool. The equivalent straight cutting edge enables the use of the oblique cutting model described in Chapter 5. An equivalent depth of cut and width of cut are derived based on the cutting geometry and the equivalent side cutting angle.

For oblique cutting, the orthogonal model is applied assuming that the inclination angle is zero, regardless of its actual value [41]. Referring to Figure 6.1, if the side cutting angle C_S^* is known from the equivalent cutting edge transformation along with

the feed *f* and the depth of cut *d*, then the effective depth of cut *t** and width of cut *w** are given by Equation (6.1) and Equation (6.2), respectively.

$$t^* = f \cos C_S^* \tag{6.1}$$

$$w^* = \frac{d}{\cos C_S^*} \tag{6.2}$$

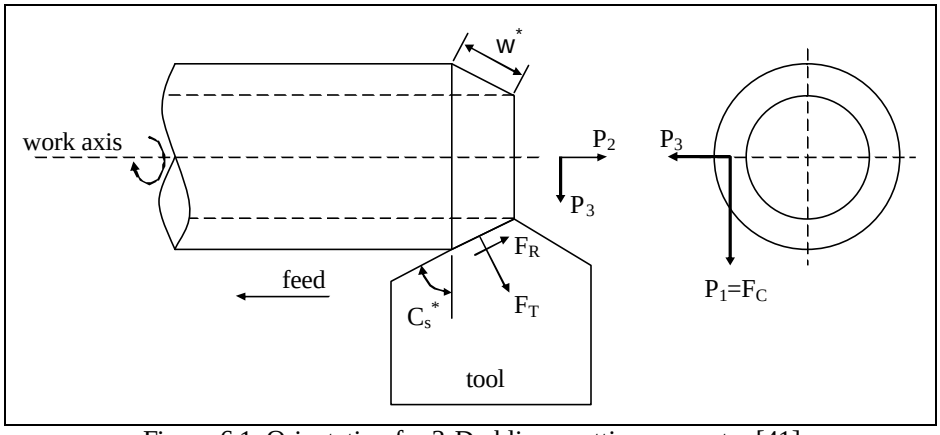

Figure 6.1 Orientation for 3-D oblique cutting geometry [41]

In addition to the chip formation forces, the plowing forces due to the roundness of the cutting edge also need to be considered in order to determine stresses induced by the roundness of the cutting tool. Waldorf extended the orthogonal plowing force model presented in [43] to predicting plowing forces in turning [54]. The extension of the model to turning incorporates similar geometric transformations in order to account for the tool nose radius and the subsequent effect on cutting forces.

The equivalent cutting edge is used in the current application of the model in order to account for the effect of the nose radius in turning. Both milling with a corner radius and turning with a nose radius are treated similarly in that an effective cutting width, depth of cut, and cutting geometry are established in order to predict plowing forces. The resulting plowing forces for the inclined case are given by

$$P_{cut} = k \cdot w^* \begin{bmatrix} \cos(2h)\cos(f-g+h)+ \\ (1+2q+2g+\sin(2h))\sin(f-g+h) \end{bmatrix} \cdot CA$$
$$P_{thrust} = k \cdot w^* \begin{bmatrix} (1+2q+2g+\sin(2h))\cos(f-g+h)- \\ \cos(2h)\sin(f-g+h) \end{bmatrix} \cdot CA \quad , \tag{6.3}$$

where w^* is given by Equation (6.2). The cutting forces F_C, F_T, and F_R shown in Figure 6.1 are given by the following equation.

$$\begin{aligned} F_C &= F_{cut} + P_{cut} \\ F_T &= F_{thrust} + P_{thrust} \\ F_R &= \frac{F_C(\sin i - \cos i \sin a_n \tan h_c) - F_T \cos a_n \tan h_c}{\sin i \sin a_n \tan h_c + \cos i} \end{aligned} \tag{6.4}$$

By utilizing the transformed cutting edge, the cutting forces F_{cut} and F_{thrust}, can be predicted with the Oxley model for sharp tools by replacing the orthogonal depth of cut and width of cut with t^* and width of cut w^*. In order to represent the forces in the orientation measured by the force dynamometer, a coordinate transformation similar to that shown in Equation (5.12) is used. Forces P_1, P_2, and P_3 which act in the cutting, feed, and axial directions, respectively are given by Equation (6.5). The expressions in Equation (6.5) vary slightly from those used in Equation (5.12) due to the orientation of the measured forces.

$$\begin{aligned} P_1 &= F_C \\ P_2 &= F_T \cos C_S^* + F_R \sin C_S^* \\ P_3 &= F_T \sin C_S^* - F_R \cos C_S^* \end{aligned} \tag{6.5}$$

6.3 Flow Stress Behavior of AISI 52100

In order to employ the models previously described for predicting cutting forces and residual stress, the flow stress behavior of the material needs to be known.

Machining tests have also been used by previous researchers to estimate Johnson-Cook parameters for AISI 52100. The technique developed by Shatla [85] was utilized by Ramesh [86] for determining the Johnson-Cook parameters for AISI 52100. Huang [87] calibrated the material coefficients in a similar manner. The calibrated coefficients from both sets of research are shown in Table 6.1. The coefficients for each set of data are fairly consistent between the two sources.

Table 6.1 Johnson-Cook coefficients for AISI 52100 calibrated from machining tests

Source	A	B	C	m	n
Ramesh [86]	688.17	150.82	0.0428	2.7786	0.336
Huang [87]	774.78	134.46	0.0173	3.171	0.371

Other previous research has also been conducted to determine the flow stress behavior of AISI 52100 as a function of temperature [88] and the behavior as a function of strain rate and temperature [89]. The high strain rate tests performed by Caccialupi were performed using the Split Hopkinson Pressure Bar (SHPB) technique. The Johnson-Cook parameters determined from those tests differed substantially from those obtained from the machining tests. The parameters computed from the compression tests are shown in Table 6.2.

Table 6.2 Johnson-Cook parameters for AISI 52100 determined from compression tests

Source	A	B	C	m	n
Toledo Garcia [88]	2430	1757	0.014	2.49	0.293
Caccialupi [89]	2555	1898	0.021	0.51	0.239

An additional source of stress-strain data for AISI 52100 used for comparison was published by Guo [90]. The yield strength at 22 °C was found to be approximately 1400

MPa. Brittle fracture was blamed for the relatively low yield strength at that temperature. For the other test temperatures, there was a trend of decreasing yield strength with increasing temperature. A plot of the yield strength vs. temperature data from [90] is shown in Figure 6.2.

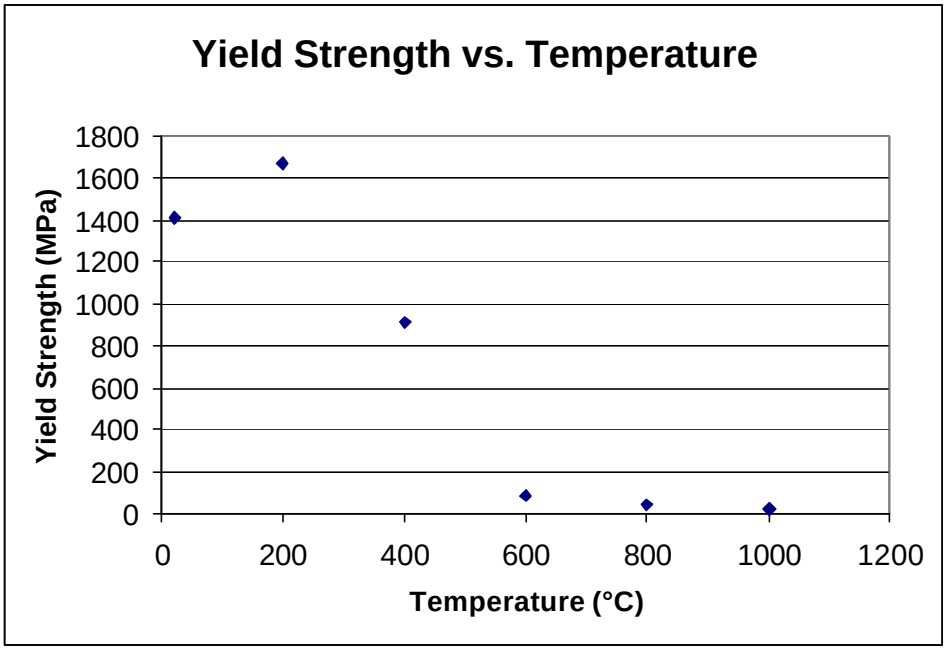

Figure 6.2 Adapted from [90]. Yield strength vs. temperature for AISI 52100

In the Johnson-Cook flow stress model, the coefficient *A* represents the uniaxial yield stress of the material. For the case of AISI 52100 in the range of hardness values used in the tests (~HRC 60) that yield stress is approximately 2000 MPa [91]. The results in Table 6.1 underestimate the yield stress while the coefficients in Table 6.2 overestimate the yield stress.

Table 6.3 Mechanical properties of AISI 52100 [90]

Temperature (°C)	22	200	400	600	800	1000
Yield Strength (MPa)	1410	1672	916	81	41	19
Yield Strain	0.0070	0.0109	0.0109	0.0030	0.0030	0.0020

The data in Table 6.3 are used as an additional source for comparison to fit coefficients in the Johnson-Cook flow stress model. The rate term of the equation is ignored since the data from Guo [90] was collected at a constant strain rate. As a result, Equation (6.6) is used to estimate the Johnson-Cook parameters excluding the strain rate term *C*. The equation is fitted to the data in Table 6.3 using a least squares fitting routine. The Matlab non-linear curve-fitting routine *lsqcurvefit*, is used to determine the set of coefficients shown in Table 6.4.

$$s_Y = \left(A + Be^n\right)\left(1 - T^{*m}\right) \tag{6.6}$$

Table 6.4 Johnson-Cook coefficients fitted to experimental data from [90]

A	B	m	n
1712	408	1.21	0.391

The coefficients in Table 6.4 do not include the strain rate constant *C*. Inspection of the strain rate constants for the other tests indicates a fairly consistent value of *C* for AISI 52100. Therefore, a nominal value of *C=0.021* is used in conjunction with the coefficients in Table 6.4 for the calculations.

6.4 Experimental Conditions and Setup

Experimental data from Thiele and Melkote [13, 14, 92] are used as a basis for comparison of the predictive capabilities of the residual stress model. The goal of their experiments was to determine the effect of hardness and edge preparation on the surface generation of hard turned AISI 52100. The experimental data consisted of both cutting

forces and sub-surface residual stress measurements which are the target of the present modeling technique. A brief overview of their experimental setup is provided below.

Machining experiments were carried out on a Hardinge Conquest TSP42 CNC lathe. Polycrystalline cubic boron nitride (PCBN) inserts with various types of edge preparation were used in the experiments. The preparation consisted of multiple levels of edge hone (22.9 μm, 94.0 μm, and 121.9 μm) and a 17° chamfer with an edge hone of approximately 25.4 μm. Edge radii were measured using a stylus-type CMM specifically designed for characterization of cutting edge geometry. The inserts were low content CBN finishing inserts of grade Kennametal KD050. The ANSI classification of each insert was TNGA-432. Inserts were mounted in a Kennametal DTGNL-164D tool holder with a -5° side rake angle, -5° back rake angle, and a 0° lead angle.

AISI 52100 steel bars nominally 28.6 mm in diameter were heat treated to 57 HRc. Thiele performed two clean-up cuts with depth of cut of 0.191 mm and feed rate of 0.10 mm/rev were made prior to the final machining. The length of cut for each test was 20.3 mm in the axial direction. The depth of cut and feed were held constant at 0.254 mm and 2.0 m/s, respectively. All tests were performed under dry cutting conditions. The test conditions are listed in Table 6.5.

Table 6.5 Test conditions for hard turning of AISI 52100 HRc 57 [92]

Case	Edge Sharpness (μm)	Nose Radius (mm)	Feed Rate (mm/rev)	Cutting Speed (m/s)	Depth of Cut (mm)
1	22.9	0.8	0.05	2.0	0.254
2	22.9	0.8	0.10	2.0	0.254
3	22.9	0.8	0.15	2.0	0.254
4	94.0	0.8	0.05	2.0	0.254
5	94.0	0.8	0.10	2.0	0.254
6	94.0	0.8	0.15	2.0	0.254
7	121.9	0.8	0.05	2.0	0.254
8	121.9	0.8	0.10	2.0	0.254
9	121.9	0.8	0.15	2.0	0.254
10	25.4 + 17° Chamfer	0.8	0.05	2.0	0.254
11	25.4 + 17° Chamfer	0.8	0.10	2.0	0.254
12	25.4 + 17° Chamfer	0.8	0.15	2.0	0.254

Force measurements in the axial, radial, and tangential direction were made for all cases. Three replications were made for each of the force measurements. Sub-surface residual stress measurements were made for Cases 9 and 12. Material properties necessary for implementing the model, in addition to the Johnson-Cook parameters Table 6.4, are listed in Table 6.6. The hardening modulus H is determined by computing the slope of the stress-strain curve of AISI 52100 found in [91] in the region 0.9-1.2% strain.

Table 6.6 Additional material properties used in the model

Material	E (GPa)	ν	H (GPa)	ρ (kg/m^3)	k (W/m°C)	C_P (J/kg°C)	α ($°C^{-1}$)	T_m (°C)
AISI 52100 HRc 60	200	0.28	60	7833	46.6	475	11.0e-6	1480

6.5 Force Predictions in Hard Turning

The comparisons between predicted cutting forces and measured cutting forces are shown below. Force predictions are compared with experimental data for the tangential, radial, and axial directions. The force predictions presented in Figure 6.3 to Figure 6.5 consist of both chip formation forces and plowing forces. The cutting cases represent varying edge hones and three levels of feed rate for each cutting edge.

The tangential cutting force results are shown in Figure 6.3. In general, the experimental data show an increase in the cutting force with an increase in the feed rate. Additionally, increasing the size of the cutting edge hone also increases the tangential cutting force. Both of these trends are captured very well by predicted tangential forces. However, the predicted tangential forces are consistently larger than the measured cutting forces. This discrepancy between the predicted values and the force values is due in part to the method of accounting for the effect on the hone radius on the effective rake angle of the tool.

In the present cutting force model, an effective rake angle is computed for the cutting tool based on the size of the hone radius, depth of cut, and the nominal rake angle. When accounting for the edge radius, the net result is a more negative rake angle. For larger negative rake angle cuts, the predicted shear angle decreases. A lower shear angle causes the shear zone to increase in size. Consequently, the force in the cut direction is

larger. For the cases evaluated, the effective rake angle predicted may differ from the actual rake angle. Although the use of the effective rake angle in these cases tends to result in higher forces in the tangential direction, the method is used in order to maintain consistency throughout the model.

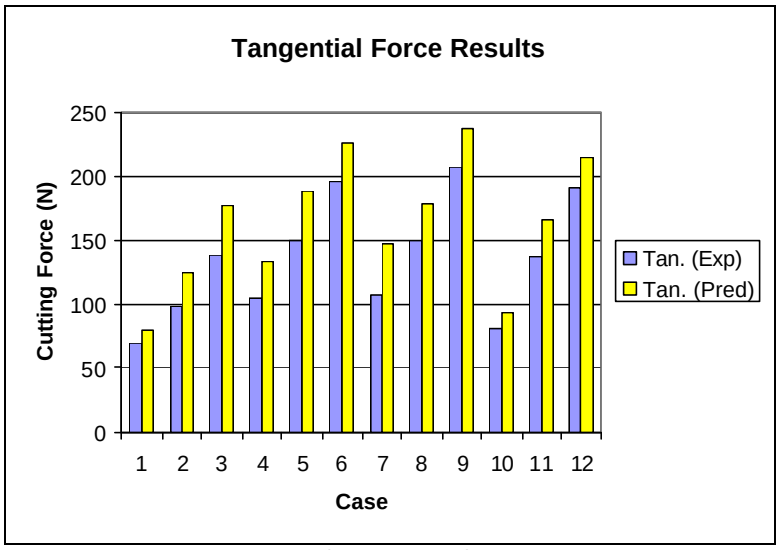

Figure 6.3 Tangential force results for turning Cases 1-12

The radial forces follow a similar trend to the tangential forces. The results for the radial force predictions are displayed in Figure 6.4. Forces in the radial direction are largely affected by the nose radius and the size of the edge hone. The general trend of the forces shows an increase in cutting force corresponding to an increase in feed along with an increase in the edge radius. The predictions capture the pattern of increasing radial force very well.

Although most of the cutting conditions follow the pattern of increasing cutting force corresponding to increasing edge radius, Cases 6 appears to deviate from the trend. The measured tangential cutting force for Case 6 is approximately 348 N. That cutting force is larger than that measured for Case 9 which uses a larger hone radius tool. This result may indicate that there is some additional tool workpiece interaction for that

particular size of edge hone that is not being captured by the cutting force model or more simply, an aberration in the force measurement. In spite of the variations in those specific cases, force predictions in the tangential direction are very reasonable.

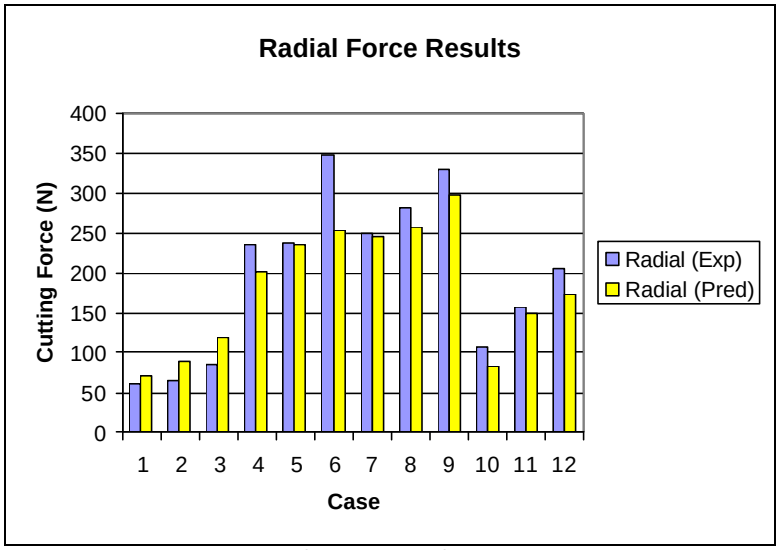

Figure 6.4 Radial force results for turning Cases 1-12

The results for axial forces are shown in Figure 6.5. The magnitudes of the axial forces for each of the cases are smaller than the forces in the other directions. The largest error of 54% is in the prediction of forces Case 2. This larger error is due in part to the axial cutting force remaining constant from Case 1 to Case 2. For a change in cutting conditions, the force model will produce different outputs. For cases where cutting conditions change with no resulting change in cutting force (e.g. Case 1 to Case 2) the model prediction is less accurate than for case where a definite trend is observed.

Additionally, the measured axial force for Case 6 appears to deviate from the trend of increasing cutting forces corresponding to increased edge radii. This situation is the same as that for the radial forces for Case 6. The cutting force model does not capture the effects leading to the increase in cutting force for that particular case. However, the general trend of cutting forces is well captured.

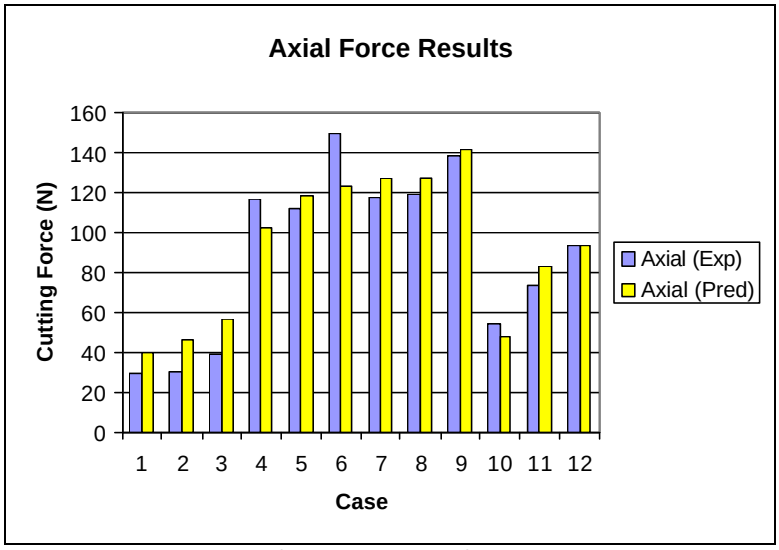

Figure 6.5 Axial force predictions for turning Case 1-12

The contribution of forces in terms of chip formation and plowing forces are shown in Figure 6.6 to Figure 6.8. The plowing force due to the tool edge increases with increasing edge radius as would be expected. There is however, a slight variation in the plowing effect from one feed rate to another for the same cutting edge. This is due to the dependence of the plowing effect on the edge radius and the cutting conditions. For a larger feed rate, the difference between the effective rake angle and the nominal rake angle is less pronounced due to the smaller contribution of the hone edge to the overall cutting geometry.

The contribution to the overall cutting force varies depending on the direction of the force prediction. In the radial and axial directions, the plowing component of the cutting force makes up the majority of the overall cutting force. For instance, in Case 4, the plowing force is approximately 58% of the total axial force and nearly 80% of the overall radial force. The high percentage of plowing force is due to tendency of the rounded tool edge to push the tool away from the workpiece resulting in higher forces in the axial and radial directions.

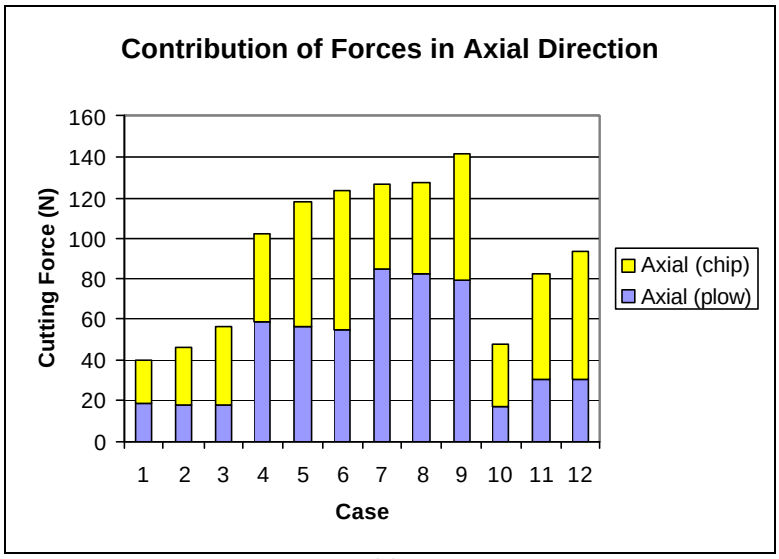

Figure 6.6 Breakdown of forces in the axial direction

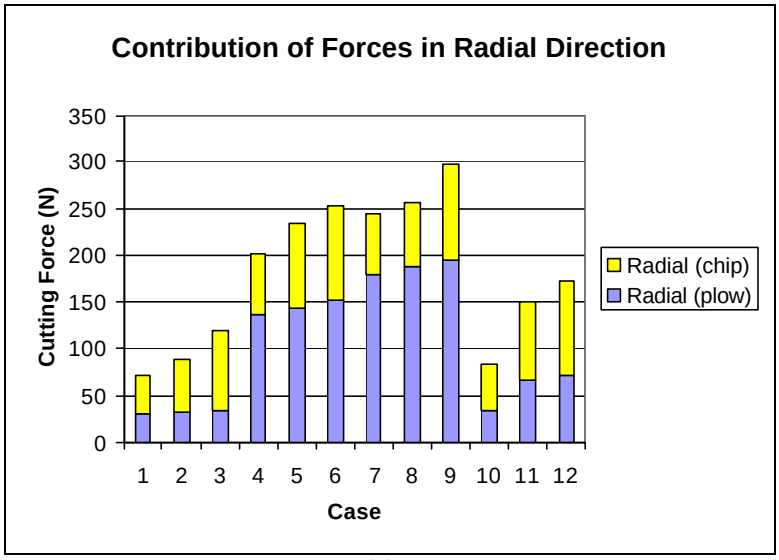

Figure 6.7 Breakdown of forces in the radial direction

For the tangential direction, the plowing contribution is less pronounced. For Case 4, the plowing contribution is only 8% of the total forces in the tangential direction. The plowing effect has less impact on forces in the tangential direction due to the nature of the plowing effect. The main influence of the plowing effect is to push the tool away from the workpiece. That effect is less noticeable in the tangential direction due to the geometry of the cut.

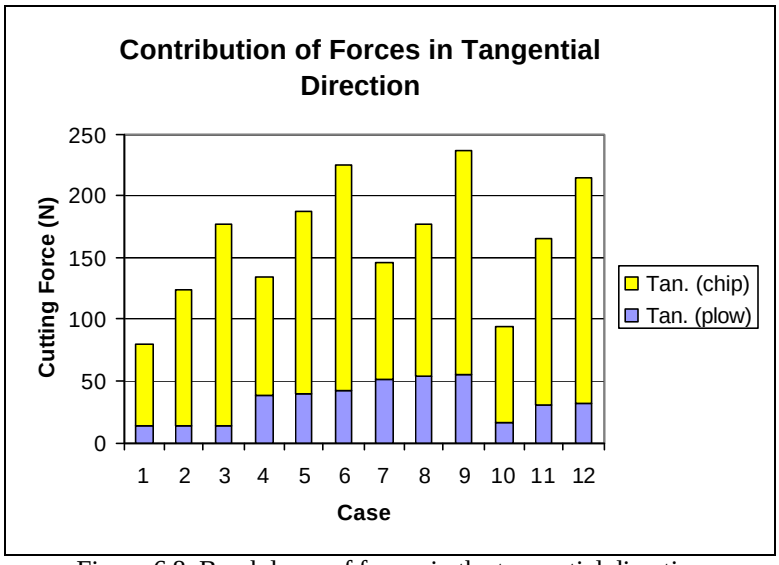

Figure 6.8 Breakdown of forces in the tangential direction

For each of the cases using the same cutting edge geometry, the plowing force remains relatively constant. The most notable exception occurs during the use of the chamfered tool (Cases 10-12). The effect is due to the size of the chamfer and the feed rate used in the experiments.

For the tools used in the Cases 10-12, the chamfer land of the cutting edge was nominally 0.115 mm $\times$ 17° [92]. In order to incorporate the chamfer into the plowing model, an equivalent edge radius like that described by Waldorf [54] is used. If the chamfer length is given by T and the chamfer angle given by l, then the equivalent edge radius is defined by Equation (6.7)

$$r_{equiv} = \frac{1}{2}\left[T\cos(l) + T\sin(l)\right] \tag{6.7}$$

An additional consideration for the chamfered edge is the feed rate which defines the effective depth of cut. For Case 10, the feed is 0.05 mm. That feed rate is smaller than the chamfer length. Therefore, an additional constraint on the T is given by Equation (6.8).

$$T = \min\left(feedrate, T \right) \tag{6.8}$$

The cutting force predictions show good agreement with the experimental data. Implementation of the force model is relatively easy with the required inputs being the model are the flow stress behavior of the material, Oxley's chip formation force model, Waldorf's plowing force model, and the tool nose radius transformation. Since the predictive capabilities are derived from physical foundations, the force model is well positioned for determining the mechanical inputs necessary for the residual stress model.

6.6 Workpiece Temperature Modeling in Hard Turning

Like milling, the cutting edge in turning is not necessarily straight. To accommodate this, the concept of the equivalent side cutting edge is utilized in order to implement the temperature modeling described in Chapter 3. The oblique moving heat source technique is used to model the temperature rise in the workpiece due to chip formation. The parallel sided moving heat source method is used estimate the temperature rise in the workpiece due to rubbing between the tool and the workpiece. Comparisons with published data for hard turning are made with predictions.

The first comparison is with published modeling data from Chou and Song [93]. They used a similar approach to predict the temperature rise in the workpiece for hard turning in an effort to model white layer formation in finish hard turning. They extended the oblique moving heat source method to a contoured cutting edge rather than using an equivalent straight cutting edge. The model produced temperature profiles like those shown in Figure 6.9.

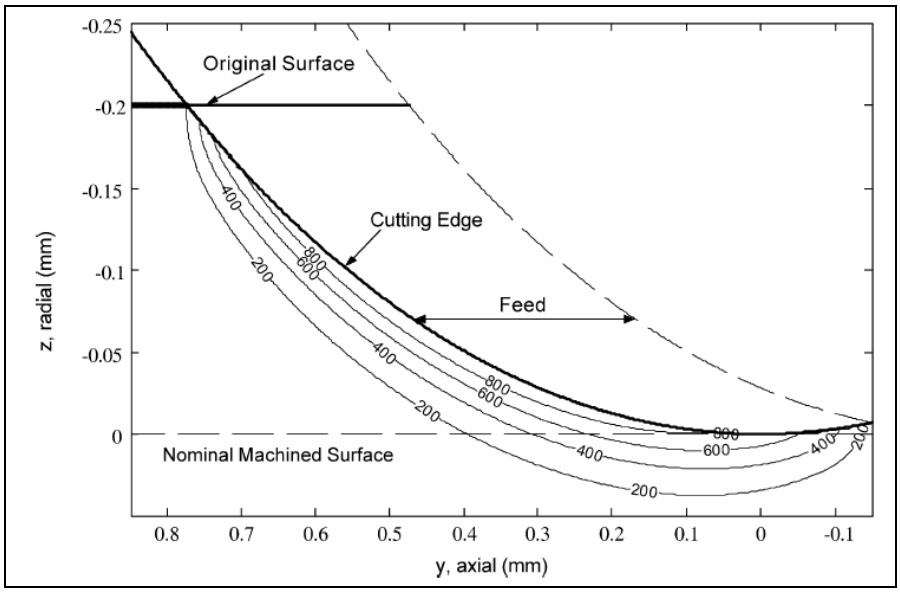

Figure 6.9 Temperature contours (in °C) around cutting edge [93]

The cutting conditions used for evaluation are shown in Table 6.7. A comparison of the temperature profile beneath the newly generated surface of the workpiece at the point y = 0 is shown in Figure 6.10. The peak surface temperature of around 850 °C matches well with published results. The temperature gradient for the model used in the current research closely matches the data from Chou [93]. The prediction from the model used in this research shows the temperature reaches the original room temperature at a depth of around 0.12 mm. Judging by the data in Figure 6.10, it appears the workpiece temperature would reach room temperature around 0.05 mm. The general trend of the temperature drop into the workpiece is consistent between the two results.

Table 6.7 Cutting conditions used in [93]

Speed (m/s)	Depth of Cut (mm)	Feed (mm/rev)	Nose Radius (mm)	Edge Geometry
2.0	0.200	0.30	1.6	$20° \times 0.1$ mm chamfer

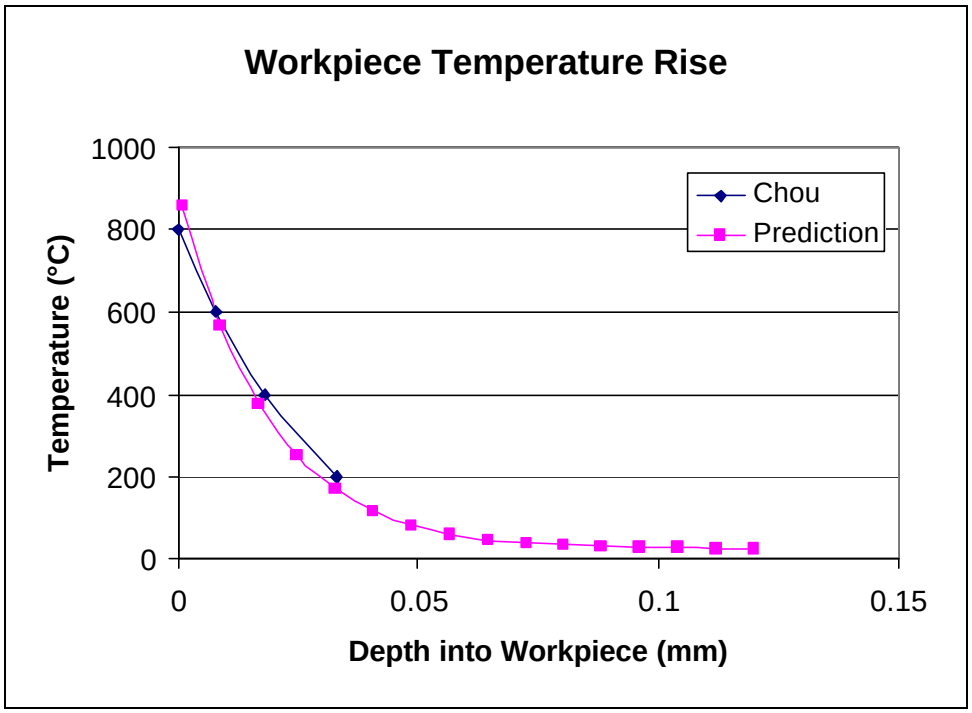

Figure 6.10 Comparison of workpiece temperature rise predictions

Published FEM results are also used as a basis for comparison for the temperature predictions used in the present model. Hua [33] used DEFORM_2D to model the effect of feed rate, workpiece hardness, and edge preparation on the process conditions such as temperature and forces and residual stresses. Predictions of the temperature rise beneath the cutting tool were made for several hard turning conditions. The material used in conjunction with the conditions listed in Table 6.8 was AISI 52100 HRc 56. A PCBN insert was used in the model.

Table 6.8 Cutting conditions from Hua used for workpiece temperature comparison

Speed (m/s)	Depth of Cut (mm)	Feed (mm/rev)	Nose Radius (mm)	Edge Geometry
2.0	0.35	0.28	0.8	20° chamfer
2.0	0.35	0.56	0.8	20° chamfer

The results of increasing feed rate on the temperature are shown in Figure 6.11 and Figure 6.12. The maximum surface temperatures predicted by FEM were approximately 675 °C and 770 °C for feeds of 0.28 mm/rev and 0.56 mm/rev, respectively. The maximum surface temperatures predicted using the oblique moving heat source model were 795 °C and 770 °C for the feeds of 0.28 mm/rev and 0.56 mm/rev, respectively. Assuming the FEM prediction is the true value of the workpiece surface temperature, the error in the prediction is approximately 18%. In considering the variability of the material properties and other conditions used in predicting the temperature, the result is very reasonable.

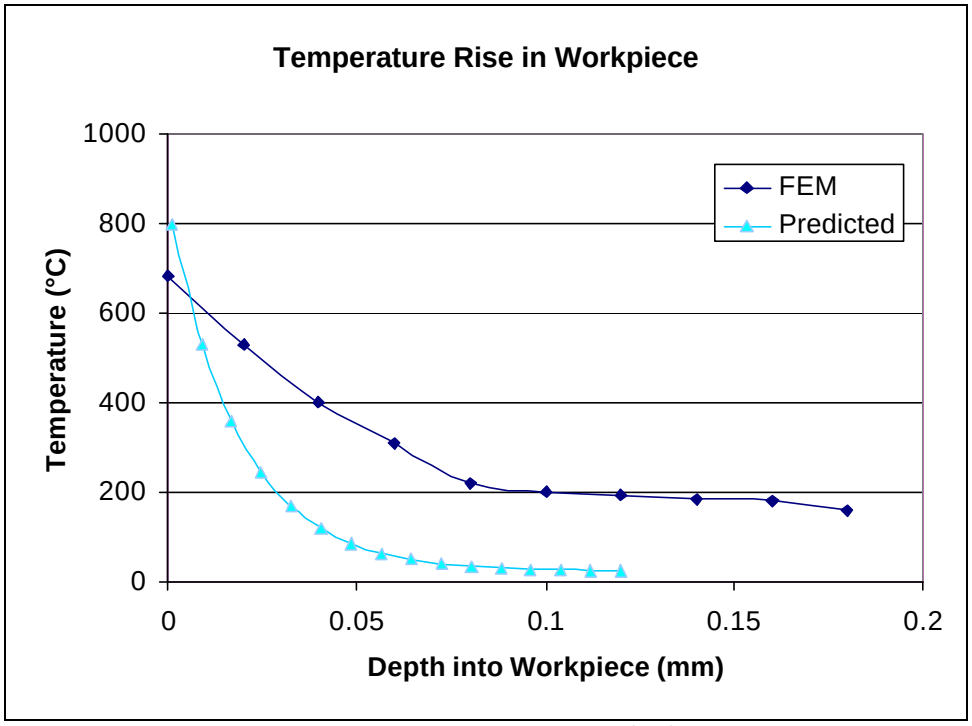

Figure 6.11 Workpiece temperature comparison for feed = 0.28 mm/rev

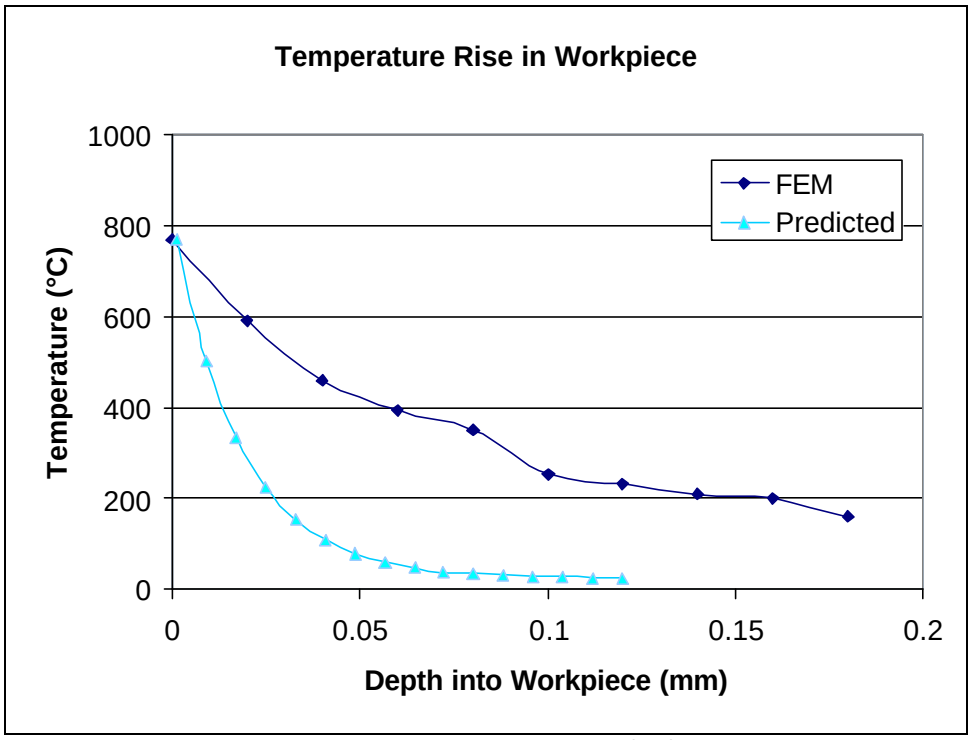

Figure 6.12 Workpiece temperature comparison for feed = 0.56 mm/rev

A notable result of the analytic prediction is that the maximum surface temperature for feed rate of 0.28 mm/rev is actually higher than the maximum surface temperature for the feed rate of 0.56 mm/rev. This is due to the change in effective cutting geometry of the cutting edge for the larger feed. The predicted shear angle varies between the two cutting cases as does the predicted flow stress. The slight variation in predicted values for those two process parameters results in changes in the heat intensity because the heat intensity is dependent on the forces and the shear area. The net effect is a slightly higher maximum surface temperature prediction for the lower feed rate case.

Another aspect of the FEM prediction is the lower temperature gradient beneath the surface. The high temperature gradient predicted from the oblique heat source method is due to the thermal behavior of the material. The thermal diffusivity and the cutting speed influence the depth to which the temperature rises in the workpiece. Another explanation for the lower temperature gradient in the FEM prediction is the

effect of plastic work. In the moving heat source model, the only source of heat is near the region of chip formation. However, in the FEM model, plastic deformation in the workpiece is also treated a source of heat. This effectively places heat sources within the workpiece, thus raising the temperature within the body. These effects are neglected with the moving heat source type models.

6.7 Residual Stress Predictions for Hard Turning

Having established reasonable cutting force and temperature predictions for the hard turning process, the residual stress model is implemented for hard turning conditions. The cutting force and temperature predictions are used as inputs to predict the thermo-mechanical loading experienced by the workpiece during machining. Sub-surface residual stress predictions for hard turned AISI 52100 are compared with published experimental data. The residual stress predictions are performed for the hoop direction and axial directions shown in Figure 6.13.

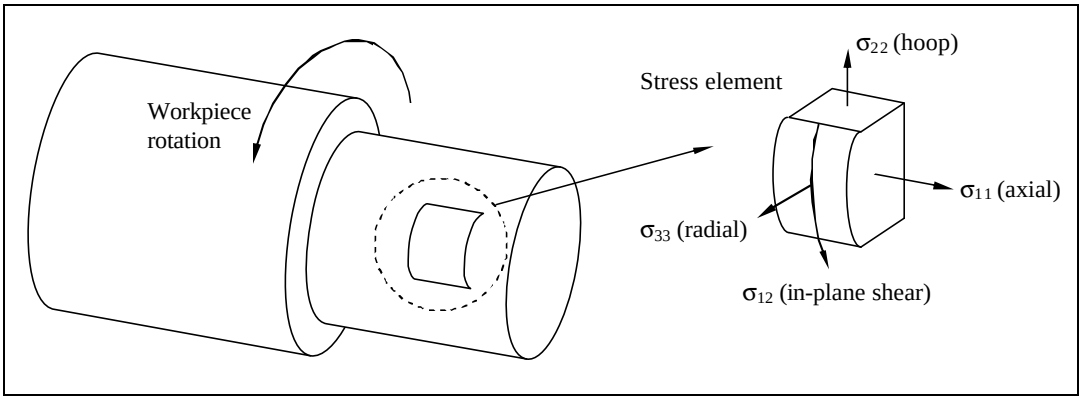

Figure 6.13 Adapted from Thiele [92]. Stress component notation

Residual stress measurements were conducted on a TEC Model 1600 goniometer. Chromium K_α radiation was used to scan the {211} peak. A rotating anode generator operating at 35 kV and 1.5 mA was used as the x-ray source. Count times of 100 s were

used. Samples were scanned at tilt angles of 0°, 18.4°, 33.2°, 39.2°, and 45°. Biaxial residual stress analysis was used to compute the residual stresses from diffraction data. Through-thickness measurements were made by removing material in increments of 12.7 μm using electrolytic polishing. The electrolytic polishing solution was composed of 72% ethanol, 10% butylcellosolve, 10% distilled water, and 8% perchloric acid [92].

Through-thickness residual stresses were measured for Cases 9 and 12 listed in Table 6.5. The comparisons between the model predictions and experimental data are shown Figure 6.14 through Figure 6.17. The experimental data show compressive residual stresses near the surface for both cases. Additionally, there is a noticeable trend with regards to the depth of the maximum compressive residual stress. For the samples machined using the conditions for Case 9, the depth of penetration of the residual stress increases.

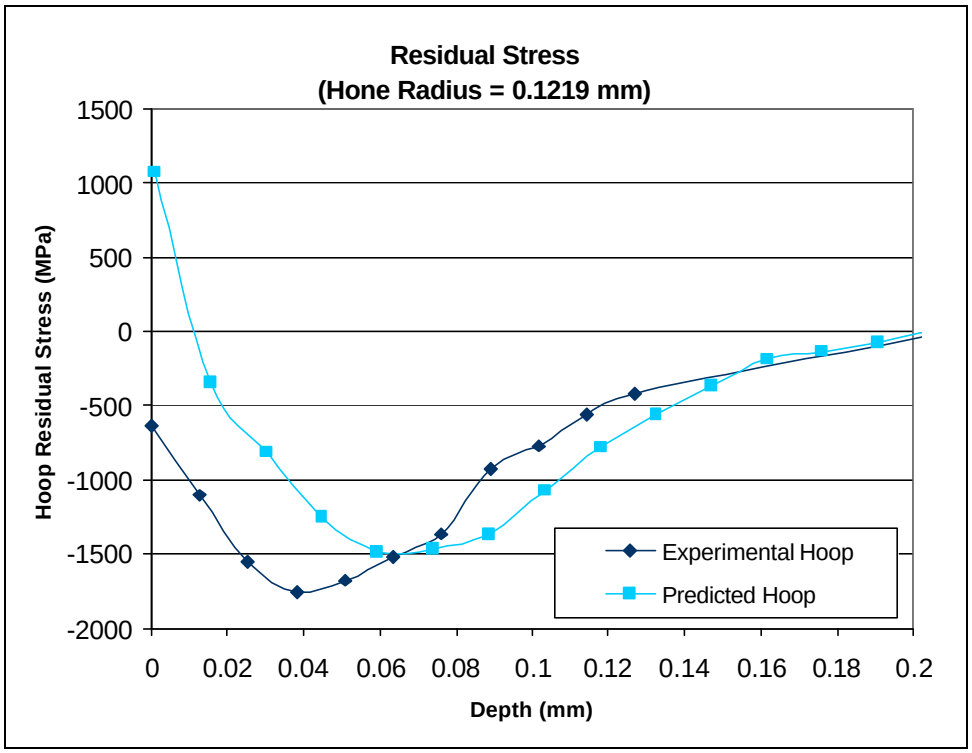

Figure 6.14 Residual stress results in the hoop direction for Case 9

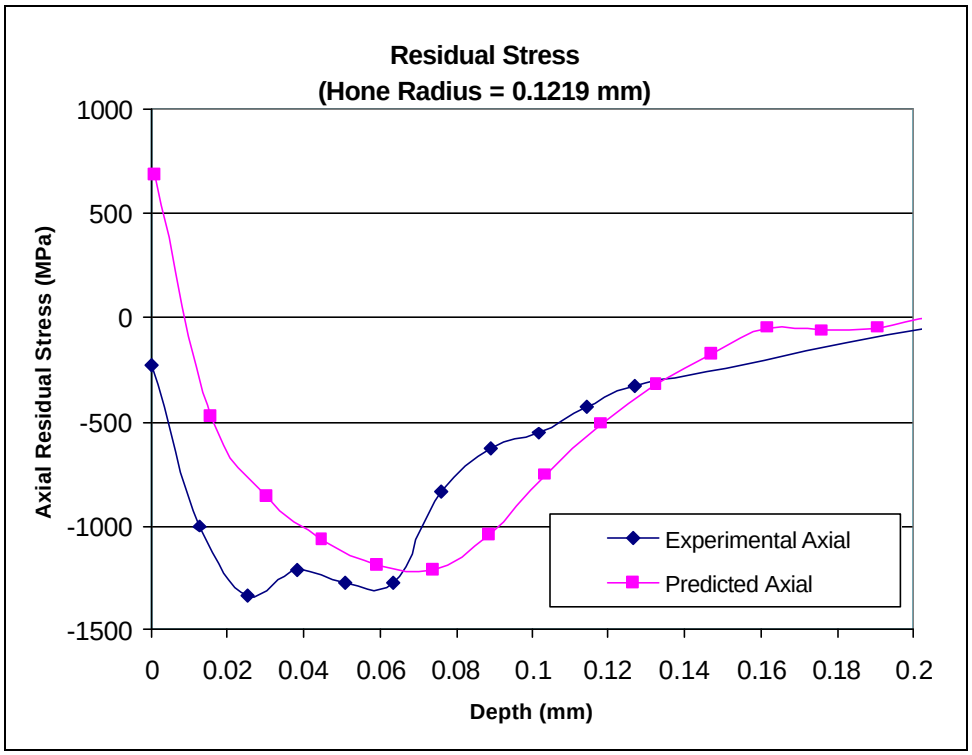

Figure 6.15 Residual stress results in axial direction for Case 9

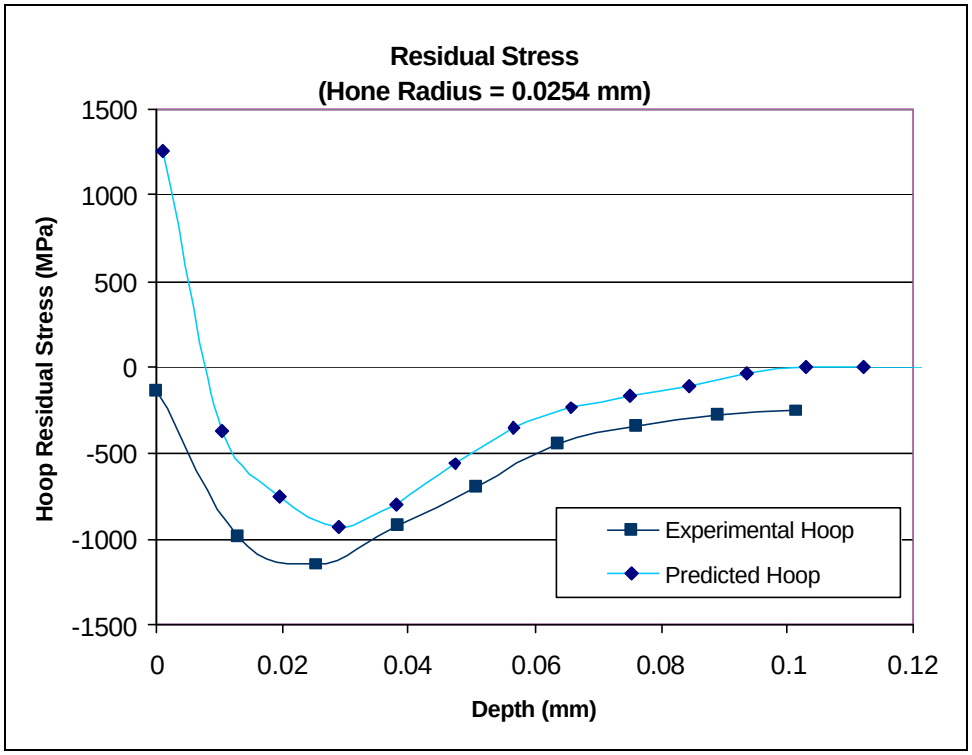

Figure 6.16 Residual stress results in the hoop direction for Case 12

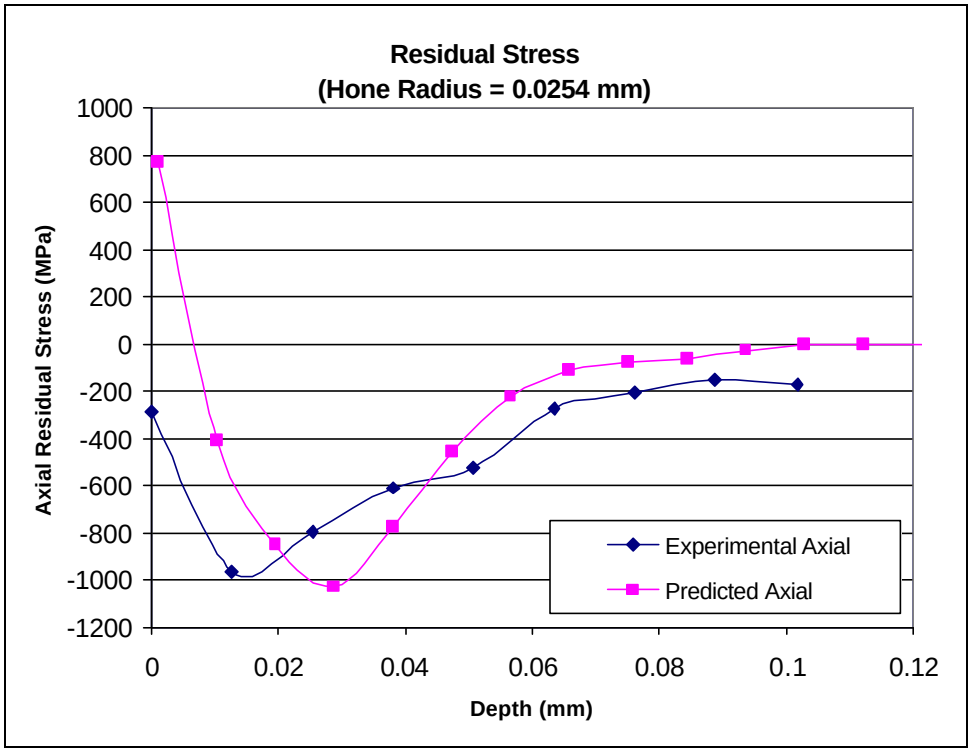

Figure 6.17 Residual stress results in the axial direction for Case 12

For the hard turned samples produced with the large hone edged tool (Case 9), the maximum compressive residual stress in the hoop direction is approximately -1764 MPa and is located at a depth of approximately 38.1 µm beneath the workpiece surface. In the axial direction, the magnitude is approximately -1336 MPa. Although there is slight oscillation, the depth of maximum compressive residual stress is considered to be 25.4 µm beneath the surface. The model prediction for the depth and magnitude of the maximum compressive residual stress for hoop direction are 59.4 µm and -1488 MPa, respectively. Similarly, the model predictions for the depth and magnitude of the maximum compressive residual stress in the axial direction are 74.0 µm and -1207 MPa, respectively. For both experimental data and model predictions, the residual stresses appeared to diminish around 20.0 µm.

For Case 12, the maximum compressive residual stress in the hoop direction is -1148 MPa. The location of the maximum compressive stress is approximately 25.4 µm beneath the workpiece surface. The model prediction for the depth and magnitude of the compressive residual stress is 28.8 µm and -930 MPa. For the axial direction, the location of the maximum compressive residual stress is 25.4 µm below the surface and it has a magnitude of -962 MPa. The predicted values for those two categories are 28.8 µm and -1098 MPa, respectively. The residual stresses diminished beyond 10.0 µm. A summary of those results is provided in Table 6.9.

Table 6.9 Depth and magnitude of maximum compressive residual stress for Cases 9 and 12

Case	Orientation	Depth (μm)	Magnitude (MPa)
9	Axial (Exp)	25.4	-1413
	Axial (Pred)	74.0	-1207
	Hoop (Exp)	38.1	-1764
	Hoop (Pred)	59.4	-1488
12	Axial (Exp)	25.4	-962
	Axial (Pred)	28.8	-1092
	Hoop (Exp)	25.4	-1148
	Hoop (Pred)	28.8	-930

Figure 6.18 and Figure 6.19 below show the predicted second invariant of stress J_2 stress contours in the workpiece beneath the tool edge for Cases 9 and 12, respectively. The contact region in Figure 6.18 is larger, and the J_2 values are higher than those shown in Figure 6.19. The maximum ratio of J_2 to the yield strength of the material is approximately 3 for Case 9. In Case 12, that value is only 2.5. The greater stresses produced by the larger edge hone result in more plastic deformation and consequently higher levels of compressive residual stress. Additionally, the penetration of the stresses to where yielding is expected to occur ($J_2 > 1$) is further beneath the surface for the large hone radius. These findings help to explain the magnitudes of the residual stress profiles shown in Figure 6.14 to Figure 6.17.

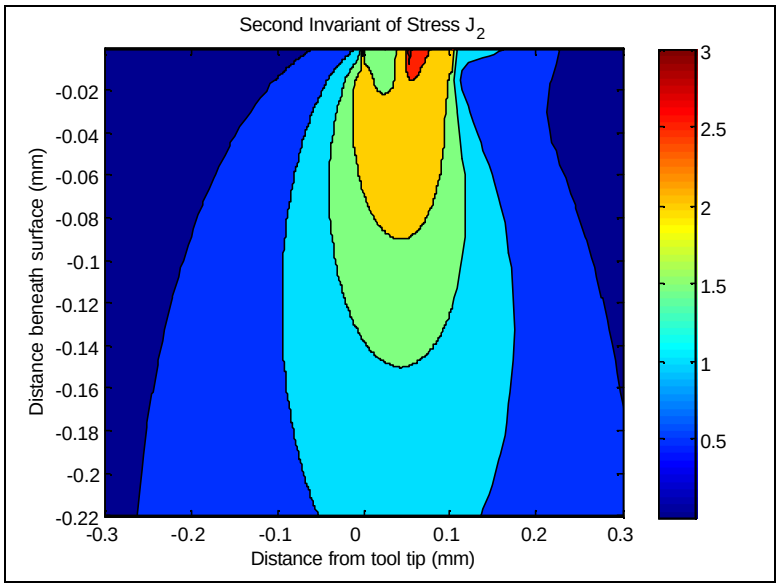

Figure 6.18 Second invariant of stress contours for Case 9

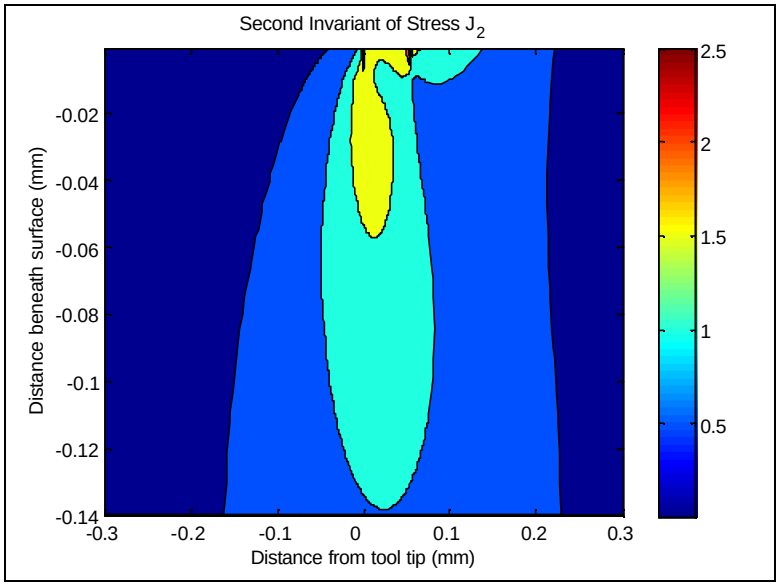

Figure 6.19 Second invariant of stress contours for Case 12

The model predictions capture the general trends of the profiles and magnitudes of the residual stresses produced by the hard turning operation. However, there are a few differences between the predicted values and the measured values. Firstly, predicted tensile residual stresses on the surface are at odds with the measured compressive surface residual stresses. Additionally, the predicted depths of maximum compressive residual stress are deeper than the measured values.

There are a few explanations possible for the discrepancies. The first is the potential that the variation in cutting forces is causing an over-estimate of the contact size, resulting in deeper penetration of the effective stress in the workpiece. However, the modeling results in the previous chapters showed that the depth of maximum compressive residual stress is generally well predicted with the model.

Another possibility is the presence of a change in chemical composition of the material at the workpiece surface. The experimental data collected in [92] included analysis of workpiece microstructures. Samples were analyzed for micro structural changes produced by the turning process. The analysis showed that samples machined with feed rates larger than 0.05 mm/rev showed signs of phase changes, indicating the thermal effects dominate surface residual stresses for the large feeds.

Thiele found that three basic micro structural patterns were found to exist on the machined surfaces for feed rates larger than 0.05 mm/rev. Those patterns included continuous white layers, intermittent white layers, and dark layers. The patterns were produced as a result of heating and subsequent cooling of the workpiece during the cutting process. White layers arise from heating the workpiece material above δ-γ transformation temperature and subsequent rapid cooling. They are composed mostly of fine-grained, untempered martensite that resists etching and appears white when viewed with an optical microscope [94]. The dark layers, composed of over-tempered martensite, are created by heating the workpiece below the δ-γ transformation temperature.

The residual stresses in the hoop and axial directions were found to correlate with the microstructural patterns. The samples that showed continuous white layers on the

surface also corresponded to compressive residual stresses in the axial and hoop directions. Figure 6.20 shows the continuous white layer formed from hard turning Case 9. Case 12 was also found to have produced continuous white layers as shown in Figure 6.21 .

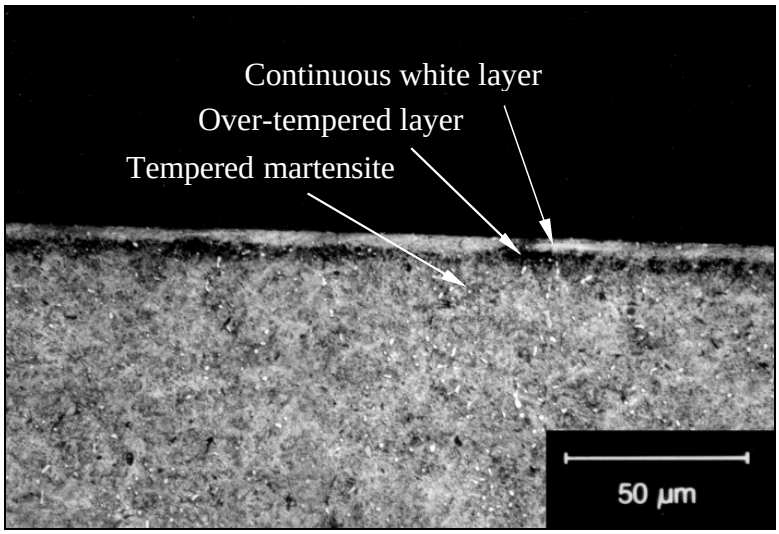

Figure 6.20 Continuous white layer on hard turned AISI 52100 Case 9 [92]

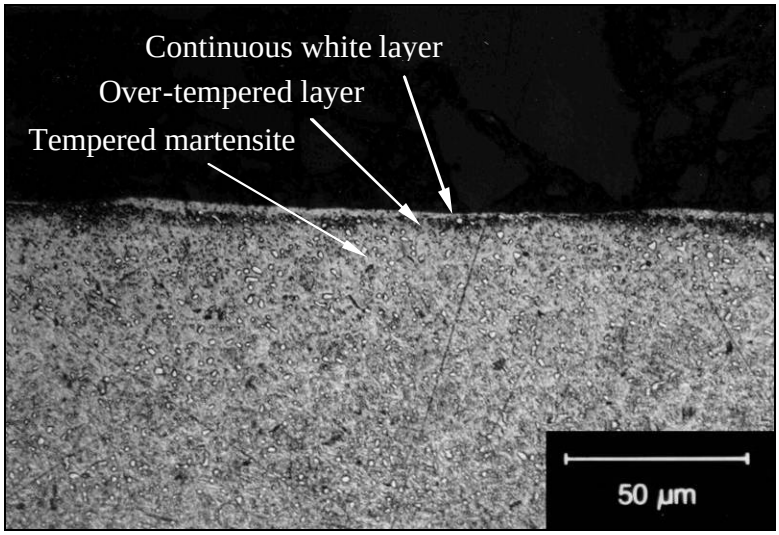

Figure 6.21 Continuous white layer on hard turned AISI 52100 Case 12 [92]

The residual stress predictions in the previous section indicated tensile residual stresses near the surface. However, experimental data for the conditions showed compressive residual stresses near the surface. The dichotomy between the predictions

and the experimental data can be attributed to the white layer formation at the surface of the machined part. Rapid cooling of the workpiece material results in the formation of untempered martensite which has a tendency to expand [95]. The untempered martensite must maintain compatibility with the interior layer of the material and reach static equilibrium once the loading due to the tool is removed. The interior workpiece material prevents expansion of the untempered martensite, thus producing compressive residual stresses at the surface.

Additional experimental data from Smith also showed lower levels of compressive residual stress with white layers [96]. In modeling the effect of white layer on residual stress formation, Ramesh [86] found similar results. Modeling residual stresses without considering the effect of white layer formation resulted in more tensile residual stresses compared to the same modeling conditions in which white layer formation was considered. Furthermore, the location of peak compressive residual stresses shifted toward the workpiece surface when white layer was accounted for in the machining simulations. The work also concluded that increasing cutting conditions such as cutting speed increase the heat flux into the workpiece which in turn cause higher temperatures at the workpiece surface. The greater thermal expansion initially places the surface layers in compression. When the surface layers cool, they shrink, causing them to be placed in tension.

Previous research in white layers and residual stress has produced somewhat contradictory results. Matsumoto, et al [19] found that tensile residual stresses corresponded to white layers on the surface of AISI 4340 steel. Similarly, Toenshoff [97] reported tensile residual stresses associated with continuous white layers formed during

hard turning of ASTM 5115 steel. However, Abrao [98] showed that compressive residual stresses are associated with white layers generated by hard-turning AISI 52100 steel. Thiele proposed that the volume expansion of the higher carbon content AISI 52100 steel was greater than the volume expansion for the other steels resulting in the compressive residual stresses measured in AISI 52100.

The residual stress profiles predicted in the previous section are made assuming no chemical changes occur in the workpiece. However, in considering the discussion regarding the effect of white layer on the residual stress profile, it is apparent that the residual stresses near the surface are influenced by white layer. The predictions of tensile residual stress on the surface using the present modeling technique are consistent with the results of Ramesh when not considering white layer. The sub-surface residual stress predictions, however, match well with the experimental data. This indicates that the thermo-mechanical model for residual stress performs better in conditions where effects such as white layer are not present.

6.8 Summary

In this chapter, an extension of the residual stress model introduced in Chapter 3 is applied to hard turning. Several aspects of the residual stress model including flow stress parameters, cutting forces, and cutting temperatures are evaluated. Johnson-Cook parameters are computed for AISI 52100 based on various sources in order to establish flow stress information for the workpiece. The computed flow stress parameters fall between machining-test computed values and compression test values.

The turning force predictions show good agreement with the experimental data. Forces predicted in the cut direction are generally larger than measured forces while forces in the axial and radial directions are in line with experimental data. Forces are decomposed into chip formation and plowing forces. The plowing forces are found to be relatively constant for each cutting edge. The chip formation forces vary depending on the cutting parameters. This would be expected as the plowing is largely a function of the edge condition.

The cutting temperatures of the workpiece surface are compared with published experimental data. The comparisons are made with FEM predictions as well as other moving heat source models. Comparisons with moving heat source models match the data very well in terms of maximum temperatures and the temperature rise in the workpiece. When compared to the FEM predictions, the maximum surface temperatures are similar, but the sub-surface temperature rise is lower than the FEM results. However, the general temperature trends are well captured.

The residual stress modeling results are compared with two complete sub-surface predictions for hard turned AISI 52100. The comparisons show that sub-surface residual stress predictions are very good in terms of magnitude and depth of penetration. However, near surface residual stresses deviate from measured values. The difference between model predictions and experimental data are attributed to the presence of white layer near the surface. White layer introduces compressive residual stresses near the surface. The chemical changes introduced by the cutting process near the surface are not captured in the predictive model.

CHAPTER 7

CONCLUSIONS

7.1 Summary

This dissertation presents a method of predicting residual stresses generated as a result of machining processes. The residual stress modeling techniques were derived from previously developed modeling techniques for orthogonal machining processes. In Chapter 3, the general model based on orthogonal cutting was presented. The modeling approaches covered included predicting cutting forces, cutting temperatures, and the residual stresses generated by the process. An analysis of the model behavior for varying parameters on predicted outputs was conducted.

Chapter 4 compared the model predictions to published experimental data for orthogonal cutting cases. Cutting forces were compared with the published experimental data. Workpiece temperature predictions were also presented. The residual stress model was compared to experimental data for a range of materials. The results showed good agreement with cutting forces and residual stress trends. Depths of maximum compressive residual stress as well as overall depth of penetration were captured by the model.

Chapter 5 extended the predictive model to milling operations. Cutting forces and temperature estimates were made for milling of Ti 6Al-4V and compared with experimental data. The effects of coolant were introduced into the model. Geometric transformations were made in order to apply the orthogonal model to the more complex

milling scenarios. Residual stress measurements were made for several milling conditions. The measured sub-surface residual stress profiles were found to be compressive for the cases explored. The model predictions captured the trends of residual stresses produced from the experiments. A sensitivity analysis was performed to assess the impact of varying values of input parameters on the modeling results. Similar to the orthogonal machining cases, the friction coefficient was found to have the most influence on the behavior of the model for the range of parameters tested.

In Chapter 6, the modeling technique was applied to turning. Residual stress predictions deviated from the experimental data near the surface. The discrepancy between predicted and measured residual stresses was attributed to the white layers present near the surface. The sub-surface predictions, however, matched the measured data well.

7.2 Conclusions

The research presented in this dissertation was driven by the need for an analytical model for predictive modeling of machining-induced residual stress. The research has shown that it is possible to model machining induced residual stresses in an analytical fashion. The impact of cutting forces and thermal effects coupled with knowledge of the material behavior under the influence of those parameters can be coupled with an incremental plasticity model to predict residual stresses. The modeling techniques presented are well suited for quick and trend-accurate analysis of machining process output parameters such as cutting forces, workpiece temperatures, and resulting residual stresses. With a few exceptions, the cutting forces were well predicted for the

various machining operations. Although the residual stress model was less effective in the presence of chemical changes to the workpiece material, it performed well in cases where such conditions were absent. The residual stress predictions captured the experimental data trends, and were in many cases very close to the measured values. Cutting temperatures, although not directly measured, were reasonable for the conditions used in the analysis.

7.3 Contributions

The modeling techniques presented in this dissertation provided improvements to the current state of the art in analytical residual stress prediction in machining. The intellectual contributions of the research presented are as follows:

- Developed an analytical predictive residual stress model for machining based on cutting forces, thermal effects, and flow behavior of the material
- Extended the rolling contact model to include thermal effects
- Validated the model for orthogonal cutting conditions based on published experimental data
- Performed a sensitivity analysis of the model to characterize how model inputs affect the model results
- Validated the model for milling operations including slot milling and face milling
- Incorporated the effects of coolant in terms of lubrication and cooling
- Performed a sensitivity analysis of the model with respect to milling operations to estimate the impact of various model inputs

- Extended the residual stress model for use in turning operations
- Validated the model with published experimental data of AISI 52100

7.4 Future Work

The current model provides a solid foundation for predicting both cutting forces and residual stresses produced from the machining process. It offers a quick and effective method of modeling those process output parameters. However, there are opportunities for improving the predictive capability of the model. The following areas for future research will help to address limitations in the current modeling capabilities and improve the state of residual stress modeling.

For the modeling used in this research, steady state conditions are assumed. The dynamic effects of the machining process such as vibration and tool wear are not considered in this work. The variations in cutting output parameters due to these effects may impact the residual stress generation.

Although the model presented performs well in terms of capturing trends and magnitudes of residual stresses produced from a variety of cutting conditions, there are still areas for improvement. The effect of phase transformation is apparent in the hard turned experimental data. The current modeling approach does not account for that effect on the residual stress formation. A method to incorporate phase transformation and its influence on the residual stress production needs to be developed.

Using coolant in the machining operations also presents additional challenges to the residual stress predictive model. In the present application, the friction coefficient due to coolant is treated as a constant value. However, since the sensitivity analysis

showed a strong correlation between friction and other output parameters for the range of friction coefficients tested, perhaps a more analytical approach will be necessary to quantify the effects of friction on machining output parameters. A physics-based model for determining the friction coefficient can be used to determine a range of friction values consistent with the machining process being studied. A boundary lubrication model can be used to determine the friction coefficient based upon the lubricating conditions along with the roughness of the tool-chip interface. The true value of friction will depend on the lubrication conditions as well as the interface between the tool and workpiece.

In a similar vein, the heat transfer coefficient due to coolant application can be estimated by a physics-based approach through the use of convective cooling theory. Previous researchers have treated the cooling effect as a forced convection problem with the geometry of the cutting process dictating the method of predicting the heat transfer coefficient.

In addition to refining the coolant dependent modeling parameters, the geometric modeling of the machining processes can also be improved. For instance, the milling predictions showed a slight, although consistent over-prediction of axial forces in the milling force predictions. The axial forces are strongly influenced by tool geometry parameters including the helix angle, edge sharpness, and the corner radius. A more refined model representing the interaction at the tool edge radius may help to improve the force and resulting residual stress predictions in those areas.

One consideration regarding the sensitivity of the model is to establish how variations in model inputs affect the force and residual stress predictions. The earlier sensitivity analysis indicated that cutting forces and residual stresses were dependent

upon the friction coefficient. However, a relationship between cutting forces and residual stress due to variations in friction and other input parameters was not established. Progression of the modeling effort should target to fill this void.

Measuring residual stresses is still a laborious task. Developing alternative techniques to measure sub-surface residual stresses such as the Barkhausen noise or ultrasonic sensing will ease the tremendous experimental efforts necessary to acquire residual stress data. Advancements in measuring capabilities may help to improve general modeling capabilities as well as guide process planning in production environments.

With the above enhancements to the current modeling approach and general residual stress research, the techniques presented can progress towards becoming a more highly reliable, robust analytical model for predicting residual stresses in machined components. The results will be realized as a useful tool in improving process optimization of machining operations.

REFERENCES

[1] Noyan, I.C. and J.B. Cohen, *Residual Stress : Measurement by Diffraction and Interpretation*. 1987, New York: Springer-Verlag. x, 276 p.

[2] Henriksen, E.K., *Residual Stresses in Machined Surfaces.* American Society of Mechanical Engineers -- Transactions, 1951. **73**(1): p. 69-76.

[3] Liu, C.R. and M.M. Barash, *Variables Governing Patterns of Mechanical Residual Stress in a Machined Surface.* Journal of Engineering for Industry, Transactions ASME, 1982. **104**(3): p. 257-264.

[4] Xie, Q., et al. *A Study on Residual Stresses and Tool Wear Induced by the Machining Process*. in *NAMRC XVII*. 1989: SME.

[5] Sadat, A.B. and J.A. Bailey, *Residual Stresses in Turned AISI 4340 Steel.* Experimental Mechanics, 1987. **27**(1): p. 80-85.

[6] Sadat, A.B., *Surface Region Damage of Machined Inconel-718 Nickel-Based Superalloy Using Natural and Controlled Contact Length Tools.* Wear, 1987. **119**(2): p. 225-35.

[7] Schlauer, C., R.L. Peng, and M. Oden, *Residual Stresses in a Nickel-Based Superalloy Introduced by Turning.* Materials Science Forum, 2002. **404-407**: p. 173-8.

[8] Jang, D.Y., et al., *Surface Residual Stresses in Machined Austenitic Stainless Steel*. Wear, 1996. **194**(1-2): p. 168-173.

[9] Matsumoto, Y., F. Hashimoto, and G. Lahoti, *Surface Integrity Generated by Precision Hard Turning.* CIRP Annals - Manufacturing Technology, 1999. **48**(1): p. 59-62.

[10] Mamalis, A.G., J. Kundrak, and K. Gyani, *On the Dry Machining of Steel Surfaces Using Superhard Tools.* International Journal of Advanced Manufacturing Technology, 2002. **19**(3): p. 157-162.

[11] Jacobson, M., *Surface Integrity of Hard-Turned M50 Steel.* Proceedings of the Institution of Mechanical Engineers, Part B: Journal of Engineering Manufacture, 2002. **216**(1): p. 47-54.

[12] Liu, M., J.-I. Takagi, and A. Tsukuda, *Effect of Tool Nose Radius and Tool Wear on Residual Stress Distribution in Hard Turning of Bearing Steel.* Journal of Materials Processing Technology, 2004. **150**(3): p. 234-241.

[13] Thiele, J.D. and S.N. Melkote, *Effect of Tool Edge Geometry on Workpiece Sub-Surface Deformation and through-Thickness Residual Stresses for Hard-Turning of AISI 52100 Steel.* Technical Paper - Society of Manufacturing Engineers. MR, 1999(MR99-167): p. 1-6.

[14] Thiele, J.D. and S.N. Melkote, *Effect of Cutting Edge Geometry and Workpiece Hardness on Surface Generation in the Finish Hard Turning of AISI 52100 Steel.* Journal of Materials Processing Technology, 1999. **94**(2): p. 216-226.

[15] Thiele, J.D., et al., *Effect of Cutting-Edge Geometry and Workpiece Hardness on Surface Residual Stresses in Finish Hard Turning of AISI 52100 Steel.* American Society of Mechanical Engineers, Manufacturing Engineering Division, MED, 2000. **122**: p. 642-649.

[16] Tsuchida, K., Y. Kawada, and S. Kodama, *Study on the Residual Stress Distributions by Turning.* 1975. **18**(116): p. 123-130.

[17] Liu, C.R. and M.M. Barash, *Mechanical State of the Sublayer of a Surface Generated by Chip-Removal Process Part 1: Cutting with a Sharp Tool.* Journal of Engineering for Industry, Transactions ASME, 1976. **98 Ser B**(4): p. 1192-1201.

[18] Liu, C.R. and M.M. Barash, *Mechanical State of the Sublayer of a Surface Generated by Chip-Removal Process Part 2: Cutting with a Tool with Flank Wear.* Journal of Engineering for Industry, Transactions ASME, 1976. **98 Ser B**(4): p. 1202-1208.

[19] Matsumoto, Y., M.M. Barash, and C.R. Liu, *Effect of Hardness on the Surface Integrity of AISI 4340 Steel.* Journal of Engineering for Industry, Transactions ASME, 1986. **108**(3): p. 169-175.

[20] Wu, D.W. and Y. Matsumoto, *Effect of Hardness on Residual Stresses in Orthogonal Machining of AISI 4340 Steel.* Journal of Engineering for Industry, Transactions of the ASME, 1990. **112**(3): p. 245-252.

[21] Fuh, K.-H. and C.-F. Wu, *Residual-Stress Model for the Milling of Aluminum Alloy (2014-T6).* Journal of Materials Processing Technology, 1995. **51**(1-4): p. 87-105.

[22] Jacobus, J.K., R.E. DeVor, and S.G. Kapoor, *Machining-Induced Residual Stress: Experimentation and Modeling.* Journal of Manufacturing Science and Engineering, 2000. **122**: p. 20-31.

[23] Merwin, J.E., Johnson, K.L., *An Analysis of Plastic Deformation in Rolling Contact.* Proeedings, Institution of Mechanical Engineers, London, 1963. **177**(25): p. 676-685.

[24] Mittal, S. and C.R. Liu, *Method of Modeling Residual Stresses in Superfinish Hard Turning.* Wear, 1998. **218**(1): p. 21-33.

[25] El-Axir, M.H., *A Method of Modeling Residual Stress Distribution in Turning for Different Materials.* International Journal of Machine Tools & Manufacture, 2002. **42**(9): p. 1055-63.

[26] Sridhar, B.R., et al., *Effect of Machining Parameters and Heat Treatment on the Residual Stress Distribution in Titanium Alloy Imi-834.* Journal of Materials Processing Technology, 2003. **139**(1-3 SPEC): p. 628-634.

[27] Okushima, K. and Y. Kakino, *Residual Stress Produced by Metal Cutting.* CIRP Annals, 1971. **20**(1): p. 13-14.

[28] Mishra, A. and T. Prasad, *Residual Stresses Due to a Moving Heat Source.* International Journal of Mechanical Sciences, 1985. **27**(9): p. 571-581.

[29] Lin, Z.-C., Y.-Y. Lin, and C.R. Liu, *Effect of Thermal Load and Mechanical Load on the Residual Stress of a Machined Workpiece.* International Journal of Mechanical Sciences, 1991. **33**(4): p. 263-278.

[30] Lin, Z.-C. and B.-Y. Lee, *An Investigation of the Residual Stress of Machined Workpiece Considering Tool Flank Wear.* Journal of Materials Processing Technology, 1995. **51**: p. 1-24.

[31] Wiesner, C., *Residual Stresses after Orthogonal Machining of AISI 304: Numerical Calculation of the Thermal Component and Comparison with Experimental Results.* Metallurgical Transactions A (Physical Metallurgy and Materials Science), 1992. **23A**(3): p. 989-96.

[32] Shih, A.J., *Finite Element Analysis of the Rake Angle Effects in Orthogonal Metal Cutting.* International Journal of Mechanical Sciences, 1996. **38**(1): p. 1-17.

[33] Hua, J., et al., *Effect of Feed Rate, Workpiece Hardness and Cutting Edge on Subsurface Residual Stress in the Hard Turning of Bearing Steel Using Chamfer + Hone Cutting Edge Geometry.* Materials Science and Engineering A, 2005. **394**(1-2): p. 238-248.

[34] Hua, J., D. Umbrello, and R. Shivpuri, *Investigation of Cutting Conditions and Cutting Edge Preparations for Enhanced Compressive Subsurface Residual Stress in the Hard Turning of Bearing Steel.* Journal of Materials Processing Technology, 2006. **171**(2): p. 180-187.

[35] Liu, C.R. and Y.B. Guo, *Finite Element Analysis of the Effect of Sequential Cuts and Tool-Chip Friction on Residual Stresses in a Machined Layer.* International Journal of Mechanical Sciences, 2000. **42**(6): p. 1069-1086.

[36] Guo, Y.B. and C.R. Liu, *Fem Analysis of Mechanical State on Sequentially Machined Surfaces.* Machining Science and Technology, 2002. **6**(1): p. 21-41.

[37] Jacobus, J.K., et al., *Predictive Model for the Full Biaxial Surface and Subsurface Residual Stress Profiles from Turning.* Journal of Manufacturing Science and Engineering, 2001. **123**: p. 537-546.

[38] Marusich, T.D., et al. *Three-Dimensional Finite Element Modeling of Hard Turning Processes*. 2003. Washington, DC., United States: American Society of Mechanical Engineers, New York, NY 10016-5990, United States.

[39] Marusich, T.D., S. Usui, and R.J. McDaniel. *Three-Dimensional Finite Element Prediction of Machining-Induced Stresses*. 2003. Washington, DC., United States: American Society of Mechanical Engineers, New York, NY 10016-5990, United States.

[40] Merchant, M.E., *Mechanics of the Metal Cutting Process. Ii. Plasticity Conditions in Orthogonal Cutting.* Journal of Applied Physics, 1945. **16**: p. 318-324.

[41] Oxley, P.L.B., *The Mechanics of Machining : An Analytical Approach to Assessing Machinability*. 1989, New York: E. Horwood; Halsted Press. 242 p.

[42] Fang, N., I.S. Jawahir, and P.L.B. Oxley, *Universal Slip-Line Model with Non-Unique Solutions for Machining with Curled Chip Formation and a Restricted Contact Tool.* International Journal of Mechanical Sciences, 2001. **43**(2): p. 557-580.

[43] Waldorf, D.J., R.E. DeVor, and S.G. Kapoor, *Slip-Line Field for Ploughing During Orthogonal Cutting.* Journal of Manufacturing Science and Engineering, Transactions of the ASME, 1998. **120**(4): p. 693-698.

[44] Johnson, G.R. and W.H. Cook, *Fracture Characteristics of Three Metals Subjected to Various Strains, Strain Rates, Temperatures and Pressures.* Engineering Fracture Mechanics, 1985. **21**(1): p. 31-48.

[45] Wang, Z.G., et al., *A Hybrid Cutting Force Model for High-Speed Milling of Titanium Alloys.* CIRP Annals - Manufacturing Technology, 2005. **54**(1): p. 71-74.

[46] Adibi-Sedeh, A.H., V. Madhavan, and B. Bahr, *Extension of Oxley's Analysis of Machining to Use Different Material Models.* Journal of Manufacturing Science and Engineering, 2003. **125**(4): p. 656-666.

[47] Li, K.-M. and S.Y. Liang. *Predictive Models for Flank Wear in near Dry Machining*. 2005. Orlando, FL, United States: American Society of Mechanical Engineers, New York, NY 10016-5990, United States.

[48] Albrecht, P., *New Developments in Theory of Metal-Cutting Process -- 1. Ploughing Process in Metal Cutting.* American Society of Mechanical Engineers -- Transactions -- Journal of Engineering for Industry Series B, 1960. **82**(4): p. 348-358.

[49] Basuray, P.K., B.K. Misra, G.K. Lal, *Transition from Ploughing to Cutting During Machining with Blunt Tools.* Wear, 1977. **43**: p. 341-349.

[50] Arsecularatne, J.A., *On Tool-Chip Interface Stress Distributions, Ploughing Force and Size Effect in Machining.* International Journal of Machine Tools & Manufacture, 1997. **37**(7): p. 885-899.

[51] Manjunathaiah, J. and W.J. Endres, *A New Model and Analysis of Orthogonal Machining with an Edge-Radiused Tool.* Journal of Manufacturing Science and Engineering, 2000. **122**(3): p. 384-390.

[52] Ren, H. and Y. Altintas, *Mechanics of Machining with Chamfered Tools.* Journal of Manufacturing Science and Engineering, 2000. **122**: p. 650-659.

[53] Schimmel, R.J., W.J. Endres, and R. Stevenson, *Application of an Internally Consistent Material Model to Determine the Effect of Tool Edge Geometry in Orthogonal Machining.* Journal of Manufacturing Science and Engineering, 2002. **124**(3): p. 536-543.

[54] Waldorf, D.J. *A Simplified Model for Ploughing Forces in Turning*. 2004. Charlotte, NC, United States: Society of Manufacturing Engineers, Dearborn, 48121-0930, United States.

[55] Manjunathaiah, J., *Analysis and a New Model for the Orthogonal Machining Process in the Presence of Edge-Radiused (Non-Sharp) Tools*. Ph.D., University of Michigan, United States -- Michigan, 1998.

[56] Kragel'skii, I.V. and S.L. Rybalov, *Temperature Dependence of Specific Wear for Sliding of Rubber (Resin) on Metals.* Doklady Akademii Nauk SSSR, 1965. **164**(5): p. 1035-1036.

[57] Venkatesh, V.C. and R. Ramaswami, *Secondary Shear Zone and the Negative Wedge on H.S.S. Tools.* 1970. **18**(3): p. 513-19.

[58] Jaeger, J.C., *Moving Sources of Heat and Temperature at Sliding Contacts.* Royal Society of New South Wales -- Journal and Proceedings, 1942. **76**(Part 3): p. 203-224.

[59] Komanduri, R. and Z.B. Hou, *Thermal Modeling of the Metal Cutting Process Part I - Temperature Rise Distribution Due to Shear Plane Heat Source.* International Journal of Mechanical Sciences, 2000. **42**(9): p. 1715-1752.

[60] Komanduri, R. and Z.B. Hou, *Analysis of Heat Partition and Temperature Distribution in Sliding Systems.* Wear, 2001. **250-251**(PART 2): p. 925-938.

[61] Trigger, K.J. and B.T. Chao, *Analytical Evaluation of Metal-Cutting Temperatures.* American Society of Mechanical Engineers -- Transactions, 1951. **73**(1): p. 57-60.

[62] Huang, Y., *Predictive Modeling of Tool Wear Rate with Application to CBN Hard Turning*. Ph.D., Georgia Institute of Technology, Atlanta, GA, 2002.

[63] Sekhon, G.S. and J.L. Chenot, *Numerical Simulation of Continuous Chip Formation During Non-Steady Orthogonal Cutting.* Engineering Computations (Swansea, Wales), 1993. **10**(1): p. 31-48.

[64] Komanduri, R. and Z.B. Hou, *Thermal Modeling of the Metal Cutting Process - Part Ii: Temperature Rise Distribution Due to Frictional Heat Source at the Tool-Chip Interface.* International Journal of Mechanical Sciences, 2001. **43**(1): p. 57-88.

[65] Johnson, K.L., *Contact Mechanics*. 1985, Cambridge; New York: Cambridge University Press.

[66] Smith, J.O. and C.K. Liu. *Stresses Due to Tangential and Normal Loads on Elastic Solid with Application to Some Contact Stress Problems*. 1952: American Society of Mechanical Engineers (ASME), New York, NY, United States.

[67] McDowell, D.L., *Approximate Algorithm for Elastic-Plastic Two-Dimensional Rolling/Sliding Contact.* Wear, 1997. **211**(2): p. 237-246.

[68] McDowell, D.L., Moyar, G.J. *A More Realistic Model of Nonlinear Material Response: Appilcation to Elastic-Plastic Rolling Contact*. in *Proceedings of the 2nd International Symposium on Contact Mechancis and Wear of Rail/Wheel Systems*. 1986. Kingston, RI.

[69] Jiang, Y. and H. Sehitoglu, *Analytical Approach to Elastic-Plastic Stress Analysis of Rolling Contact.* Journal of Tribology, Transactions of the ASME, 1994. **116**(3): p. 577-587.

[70] Seo, S., O. Min, and H. Yang, *Constitutive Equation for Ti-6Al-4V at High Temperatures Measured Using the SHPB Technique.* International Journal of Impact Engineering, 2005. **31**(6): p. 735-754.

[71] Chandrasekaran, H., R. M'Saoubi, and H. Chazal, *Modelling of Material Flow Stress in Chip Formation Process from Orthogonal Milling and Split Hopkinson Bar Tests.* Machining Science and Technology, 2005. **9**(1): p. 131-145.

[72] Budak, E. and Y. Altintas. *Prediction of Milling Force Coefficients from Orthogonal Cutting Data*. 1993. New Orleans, LA, USA: Publ by ASME, New York, NY, USA.

[73] *Metals Affordability Initiative (MAI) Affordable Machining Program*.

[74] M'Saoubi, R., et al., *Residual Stress Analysis in Orthogonal Machining of Standard and Resulfurized AISI 316l Steels.* Journal of Materials Processing Technology, 1999. **96**(1-3): p. 225-233.

[75] Okushima, K. and Y. Kakino, *Residual Stress Produced by Metal Cutting.* 1971. **20**(1): p. 13-14.

[76] Li, H.Z., W.B. Zhang, and X.P. Li, *Modelling of Cutting Forces in Helical End Milling Using a Predictive Machining Theory.* International Journal of Mechanical Sciences, 2001. **43**(8): p. 1711-1730.

[77] Stabler, G.V., *Fundamental Geometry of Cutting Tools.* Institution of Mechanical Engineers -- Proceedings, 1951. **165**(63): p. 14-21.

[78] Young, H.T., P. Mathew, and P.L.B. Oxley, *Allowing for Nose Radius Effects in Predicting the Chip Flow Direction and Cutting Forces in Bar Turning.* Proceedings of the Institution of Mechanical Engineers, Part C: Mechanical Engineering Science, 1987. **201**(3): p. 213-226.

[79] Young, H.-T., et al., *Predicting the Chip Flow for Nose Radius Tools under Oblique Machining Conditions.* Journal of the Chinese Institute of Engineers, Transactions of the Chinese Institute of Engineers,Series A/Chung-kuo Kung Ch'eng Hsuch K'an, 1993. **16**(6): p. 825-834.

[80] Arsecularatne, J.A., P. Mathew, and P.L.B. Oxley, *Prediction of Chip Flow Direction and Cutting Forces in Oblique Machining with Nose Radius Tools.* Proceedings of the Institution of Mechanical Engineers, Part B: Journal of Engineering Manufacture, 1995. **209**(B4): p. 305-315.

[81] Kalpakjian, S. and S.R. Schmid, *Manufacturing Processes for Engineering Materials*. 4th ed. 2002, Upper Saddle River, N.J.: Prentice Hall. xvii, 954 p.

[82] Altintas, Y., *Manufacturing Automation : Metal Cutting Mechanics, Machine Tool Vibrations, and Cnc Design*. 2000, New York: Cambridge University Press. xii, 286 p.

[83] *Metals Affordability Initiative (MAI) Machining Distortion*. 2006.

[84] Li, X.P. and H.Z. Li, *Theoretical Modelling of Cutting Forces in Helical End Milling with Cutter Runout.* International Journal of Mechanical Sciences, 2004. **46**(9): p. 1399-1414.

[85] Shatla, M., C. Kerk, and T. Altan, *Process Modeling in Machining. Part I: Determination of Flow Stress Data.* International Journal of Machine Tools and Manufacture, 2001. **41**(10): p. 1511-1534.

[86] Ramesh, A., *Prediction of Process-Induced Microstructural Changes and Residual Stresses in Orthogonal Hard Machining*. Ph.D. Dissertation, Georgia Institute of Technology, Atlanta, 2002.

[87] Huang, Y. and S.Y. Liang, *Modeling of Cutting Forces under Hard Turning Conditions Considering Tool Wear Effect.* Journal of Manufacturing Science and Engineering, Transactions of the ASME, 2005. **127**(2): p. 262-270.

[88] Toledo Garcia, G.A., *High Temperature Compression Testing of Hardened Steels for Plasticity Behavior Modeling*. Master of Science, Georgia Institute of Technology, Atlanta, GA, 2002.

[89] Caccialupi, A., *Systems Development for High Temperature, High Strain Rate Material Testing of Hard Steels for Plasticity Behavior Modeling*. Master of Science, Georgia Institute of Technology, Atlanta, 2003.

[90] Guo, Y.B. and C.R. Liu, *Mechanical Properties of Hardened AISI 52100 Steel in Hard Machining Processes.* Journal of Manufacturing Science and Engineering, 2002. **124**(1): p. 1-9.

[91] ASM International, *Atlas of Stress-Strain Curves*. 2nd ed. 2002, Materials Park, OH: ASM International. iv, 816 p.

[92] Thiele, J.D., *An Investigation of Surface Generation Mechanisms for Finish Hard Turning of AISI 52100 Steel*. Master of Science, Georgia Institute of Technology, 1998.

[93] Chou, Y.K. and H. Song, *Thermal Modeling for White Layer Predictions in Finish Hard Turning.* International Journal of Machine Tools and Manufacture, 2005. **45**(4-5): p. 481-495.

[94] Griffiths, B.J., *Mechanisms of White Layer Generation with Reference to Machining and Deformation Processes.* Journal of Tribology, Transactions of the ASME, 1987. **109**(3): p. 525-530.

[95] Fletcher, S.G., *Dimensional Changes in Heat Treatment of Steel.* Metal Treating, 1968. **19**(2): p. 3-4.

[96] Smith, S.R., *An Investigation into the Effects of Hard Turning Surface Integrity on Component Service Life.* Ph.D., Georgia Institute of Technology, Atlanta, 2002.

[97] Toenshoff, H.K., C. Arendt, and R.B. Amor, *Cutting of Hardened Steel.* CIRP Annals - Manufacturing Technology, 2000. **49**(2): p. 547-566.

[98] Abrao, A.M. and D.K. Aspinwall, *Surface Integrity of Turned and Ground Hardened Bearing Steel*. Wear, 1996. **196**(1-2): p. 279-284.